國 立 交 通 大 學
顯 示 科 技 研 究 所

碩士論文

氧化鋅微共振腔結構下之激子−極激子雷射之光學特性

Optical Characteristics of Exciton-Polariton Lasing in ZnO-Based Microcavity

研究生：吳永吉

指導教授：盧廷昌教授

郭浩中教授

中華民國九十九年七月

氧化鋅微共振腔結構下之激子−極激子雷射之光學特性

Optical Characteristics of Exciton-Polariton Lasing in

ZnO-Based Microcavity

研究生:吳永吉   Student: Yung-chi Wu

指導教授: 盧廷昌 教授   Advisor: Prof. Tien-chang Lu

郭浩中教授   Prof. Hao-chung Kuo

國 立 交 通 大 學 電機資訊學院
顯示科技研究所
碩 士 論 文

A Thesis
Submitted to Display. Institute
College of Electrical Engineering and Computer Science
National Chiao Tung University
in Partial Fulfillment of the Requirements
for the Degree of
Master
In
Display. Institute

July 2010
Hsinchu, Taiwan, Republic of China

中 華 民 國 九 十 九 年 七 月

氧化鋅微共振腔結構下激子-極激子雷射之光學特性

研究生:吳永吉　　　　　　　　　　　指導教授:　　盧廷昌　教授

郭浩中　教授

國立交通大學顯示科技研究所

摘要

在本篇論文中，我們利用氧化鋅的微共振腔結構作為研究對象。在特性分析中，主要是光學特性上的相關研究。在發光特性方面，利用光激發螢光光譜(PL)以及反射頻譜，量測不同角度的發光特性，藉由變角度的譜譜可以定義出極激子的能量對波向量的關係圖，藉此了解光與激子之間的耦合情形，並且確認兩者之間耦合現象確實存在。

接著我們利用調變共振腔長度來調整光存在微共振腔內的能量，使激子與光之間的耦合情形發生改變。觀察此時的極激子發光情形。 在波向量等於零，當光子能量較激子能量來的低時，能量對波向量的曲線可以觀察到明顯的轉折處， 使得當極激子由較大的能量向低能處掉落時，會容易阻塞再轉折處， 這種瓶頸對於我們的目標-激子極激子雷射-是一項需要克服的問題，要克服這種瓶頸現象，便進行了不同的實驗來探討此一現象，我們藉由改變共振腔長度的方法，了解在光與激子對瓶頸現象的關係，接著我們利用變溫的變角度光激發螢光光譜(ARPL)， 確認了極激子與聲子的散射可以幫助克服瓶頸現象， 最後我們利用變功率的變角度光激發螢光光譜(ARPL)，使瓶頸現象可以藉由極激子對極激子本身的散射現象來克服。

為了在室溫的條件下觀測到玻色-愛因斯坦凝聚的現象，我們使用摻釹釩酸釔晶體脈衝雷射來進行激發並且順利在室溫下觀測到同調性的發光現象，與現有類似規格的面射型雷射相比所需的功率只有十分之一， 因此我們認為這個是因為玻色-愛因斯坦凝聚的現象所形成的激子-極激子雷射。我們初步的證明，一樣是利用變角度的光激發螢光光譜(ARPL)， 可以觀察到極激子克服平井現象後， 集中於底部形成玻色-愛因斯坦凝聚的情形。這是在氧化鋅材料下觀測到玻色-愛因斯坦凝聚的例子。

Optical Characteristics of Exciton-Polariton Lasing in ZnO-Based Microcavity

Student: Yung-chi Wu   Advisors: Prof. Tien-chang Lu

Prof. Hao-chung Kuo

Display. Institute, National Chiao Tung University

Abstract

In this paper, we use zinc oxide micro-cavity structure to study the characteristics of exciton-polaritons. By performing angle-resolved photoluminescence and angle-resolved reflection measurements, we can probe the energy-wavevector dispersion curves of cavity polaritons. This dispersion relationship can be used to understand the coupling strength between photons and excitons, and confirm the existence of cavity polaritons. Furthermore, we observed the coupling between different exciton-photon detunings by varying the length of microcavity. When the detuning is negative, photon energy lower than the exciton energy, the anticrossing can be observed in the dispersion curves, which causes a significant change in density of states. Under the condition, the bottleneck behavior should be observed during the process of polariton relaxation. This consequence may originate from the polariton states with very high photon fractions in the low angle region.

The bottleneck effect is an important obstacle to the realization of Bose-Einstein condensation in microcavity. Several systematical experiments are performed to understand the possible physical mechanisms inducing the polariton bottleneck effect. First, we change the cavity length in order to get different exciton-photon detunings, which gives rise to different photon and exciton fractions, and the corresponding density of states. Second, it is found that the polariton relaxation bottleneck can be

significantly suppressed by the mechanism of polariton-phonon scattering at high temperature. Consequently, we use the temperature-dependent and angle-resolved photoluminescence to confirm the effect of polariton-phonon scattering. Finally, the polariton-polariton interaction is an important factor under high pumping power condition, and the power-dependent angle-resolved photoluminescence can help us to understand the factor.

In order to observe Bose-Einstein condensates at room temperature, we use Nd:YVO$_4$ pulsed laser as excitation source and observe a coherence light at room temperature with a low-threshold pumping power, 1 order of magnitude smaller than in previously reported nitride-based vertical-cavity surface-emitting lasers. This is an important evidence of an exciton-polariton laser induced by Bose-Einstein condensate. In addition, based on the experimental results of angle-resolved photoluminescence, we can observe the phenomenon that the polaritons could overcome the relazation bottleneck, and then approach to the bottom of low polariton branch. This result demonstrates the experimental observation of Bose-Einstein condensation in ZnO-based microcavity at room temperature.

Acknowledgement

List of Tables

List of Figures

Chapter1. Introduction and Motivation

1.1 Polaritons for Bose-Einstein condensation(BEC) Study

Bose-Einstein condensation (BEC) has been a source of imagination and innovation of physicists ever since its first proposal by Einstein in 1925. Bose–Einstein condensation (BEC), also simply "Bose condensation", is a phase transition for bosons leading to the formation of a coherent multiparticle quantum state characterized by a wavefunction, and the BEC occupies the lowest energy level of the system that coincides with the chemical potential. In particle physics, bosons are subatomic particles that obey Bose–Einstein statistics. Several bosons can occupy the same quantum state, include photon, meson, some of atom with integer spin, exciton, etc. In 1995, the first unambiguous realization of BEC was achieved in dilute atomic gasses. The effort devoted to atomic systems has harvested a modern branch of physics, (ultra-)cold atom physics, which continues to be a test-ground of theories and a cradle of novel applications. In recent decades, the well developed fabrication techniques in semiconductor make it possible to observe the BEC phenomenon at laboratory through the microcavity-polariton BEC system. Below we briefly review the history of BEC research.

1.1.1   Atomic system BEC

The BEC phenomenon is predicted in 1924 by Satyendra Nath Bose and Albert Einstein, and is observed first from dilute atomic gases in 1995 [1, 2, 3], and later in spin-polarized hydrogen and

metastable helium gases. In atomic system BEC, because the condensation at low densities is achievable only at very low temperatures (~nK), the laser-cooling technique is necessary. The primary force used in laser cooling and trapping is the recoil when momentum is transferred from photons scattering off an atom, and the cooling is achieved by making the photon scattering rate velocity-dependent using the Doppler effect. Moreover, a magnetic quadruple field generated by two coils carrying equal currents flowing in opposite directions traps those atoms, as shown in fig 1.1(c). because of the laser cooling technique, the Bose-Einstein condensation can be observed at 200nK, as shown in fig 1.1(d), and Cornell, Wieman and Ketterle won the 2001 Nobel Prize in Physics for the achievements [18]. However, the application of atomic system BEC in room temperature is extremely different.
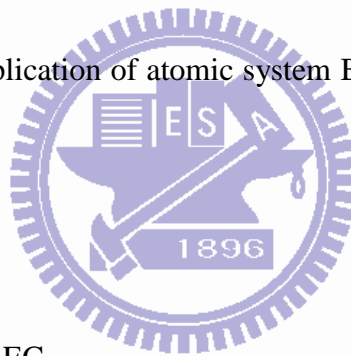
1.1.2   Exciton-polariton system BEC

Exciton BEC was first proposed in 1962 by Moskalenko et al. [4] and Blatt et al. (18). A most well-known experimental system is the ortho-excitons in bulk Cu2O. This system was considered to have shown, in the first conference on BEC held in 1995, the most convincing evidence of BEC [5]. Yet it was found out later that the auger-recombination of excitons prevented the system from reaching the critical density of BEC. In 2002, a few macroscopic phenomena observed in quantum-well exciton systems were again proposed to be related to BEC. Yet more careful analysis later concluded otherwise. Indirect evidence of quantum degeneracy was obtained with quantum-well excitons, yet no evidence

of a phase transition was inferred from these experiments, e.g. the coherenceproperties and momentum

distribution functions of the excitons. The search continuesfor exciton BEC and the question remains

open if BEC is ever possible in a solid state system.

In 1968, BEC was proposed to be also possible with bulk polaritons [7]. However, these

polaritons are outside of the optical cone and do not directly couple to light, as shown in Fig 1.2(a). It

is very difficult to study the bulk polaritons experimentally. Moreover, the minimum energy of the

bulk polariton bands are the crystal ground state with zero excitation energy. BEC is possible only

with states at an energy-relaxation bottleneck. These states have a large degeneracy in momentum,

adding much complication to the physics. There has been no successful experimental effort toward

bulk polariton condensation.

In decades, a more experimentally accessible solid-state system becomes available when the

strong-coupling regime is reached in an epitaxially grown quantum-well microcavity [8]. Due to

confinement of both the cavity photon field and the quantum excitons along the growth direction,

translational symmetry is broken in the longitudinal direction, only the transverse wavenumber $k_\parallel$ is

a good quantum number for microcavity polaritons. Hence for the relevant polariton states, there exists

a one-to-one coupling between each internal polariton mode with certain $k_\parallel$ at energy $E_{LP}(k_\parallel)$ and

each external photon mode with the same $k_\parallel$ and $E_{LP}(k_\parallel)$ emitted into certain angle θ relative to the

growth direction, as shown in Fig 1.2(b). The coupling rate is determined by the fixed cavity photon

out-coupling rate. As a result, information about the internal polaritons can be directly obtained from

the external photon emission by well developed optical techniques. Within a decade after the first observation of microcavity polaritons, stimulated scattering threshold of polaritons were reported by various groups [9, 10, 11, 12].

Table 1.1 compares the basic parameters of atomic gases to excitons and polaritons in semiconductors. The parameter scales of these systems differ by many orders of magnitude. Even in a common quantum phase transition, each system is expected to have its own characteristics, to reveal particular pieces of unexplored fundamental physics, and to have unique applications. Most notable for the polariton system is its very light effective mass and very short time scale. The former leads to a critical temperature of phase transitions ranging from 1 K up to room temperature. The latter dictates the dynamic nature of polariton phase transitions.

1.2 Properties of Microcavity

A microcavity is an optical resonator close to, or below the dimension of the wavelength of light. Micrometre- and submicrometre-sized resonators use two different schemes to confine light. In the first, reflection off a single interface is used, for instance from a metallic surface, or from total internal reflection at the boundary between two dielectrics. The second scheme is to use microstructures periodically patterned on the scale of the resonant optical wavelength, for instance a planar multilayer Bragg reflector with high reflectivity, or a photonic crystal. Since confinement by reflection is sometimes required in all three spatial directions, combinations of these approaches can be used within

the same microcavity. The resonant optical modes within a microcavity have characteristic lineshapes, wavelength spacings and other properties that control their use. A longitudinal resonant mode has an integral number of halfwavelengths that fit into the microcavity, while transverse modes have different spatial shape.   The common designs of microcavity are listed in Fig 1.3

The most common microcavity is the planar microcavity in which two flat mirrors are brought into close proximity so that only a few wavelengths of light can fit in between them. To confine light laterally within these layers, a curved mirror or lens can be incorporated to focus the light, or they can be patterned into mesas.

Due to well developed fabrication techniques, Distributed Bragg reflector (DBR) can achieve the request of high reflectance mirror. A DBR is made of layers of alternating high and low refraction indices, each layer with an optical thickness of $\lambda/4$. Light reflected from each interface destructively interfere, creating a stop-band for transmission. As shown in Fig 1.4, the DBR stop-band width is considered the number of pairs and the refraction index difference between two materials.

When two such high-reflectance DBRs are attached to a layer with an optical thickness integer times of $\lambda/2$, a cavity resonance is formed at λ, leading to a sharp increase of the transmission T at λ, as shown in Fig1.5.

1.2.1   Q-factor and finesse

The quality-factor (or Q-factor) has the same role in an optical cavity as in an LCR electrical circuit, in that it parametrizes the frequency width of the resonant enhancement. We can define a

characteristic parameter, the cavity quality factor Q of the cavity quality.

$$Q = \frac{\omega_c}{\delta\omega_c} \approx \frac{\lambda}{\Delta\lambda}$$

Eq(1.1)

The finesse of the cavity is defined as the ratio of free spectral range (the frequency separation between successive longitudinal cavity modes) to the linewidth (FWHM) of a cavity mode :

$$F = \frac{\Delta\omega_c}{\delta\omega_c} = \frac{\pi\sqrt{R}}{1-R}$$

Eq(1.2)

Q is the average number of round trips a photon travels inside the cavity before it escapes. That is, the higher Q value means the higher ability to confirm a photon. Equivalently, the exponentially decaying photon number has a lifetime given by $\tau = \frac{Q}{\omega_c}$. Because the mode frequency separation $\Delta\omega_c = \frac{2\pi c}{L}$ is similar to the cavity mode frequency in a wavelength-scale microcavity, the finesse and the Q-factor are not very different. This is not the situation for a large cavity, in which case the Q-factor becomes much greater than the finesse because of the long round-trip propagation time. Instead, the finesse parameterizes the resolving power or spectral resolution of the cavity.

$$Q = \frac{2n_{neff}L_{cav}}{\lambda}F$$

Eq(1.3)

In order to achieve the higher quality factor (Q) and higher finesse, we have to use the higher reflectivity mirrors as much as possible.

1.3 Introduction to coupling between photon and exciton

1.3.1   The time-dependent Schrödinger equation

The quantum treatment of the interaction between light and atoms is usually developed in terms

of the two-level atom approximation. This approximation is applicable when the frequency of the light

coincides with one of the optical transitions of the atom. The condition is depicted schematically in Fig

1.6.

The time-dependent Schrödinger equation for a two-level system in the presence of the light is a

great method to understand the coupling between photon and exciton. In other words, we must solve:

$$\hat{H}\Psi = i\hbar \frac{\partial \Psi}{\partial t} \qquad\qquad\qquad Eq(1.4)$$

for an atom with two energy levels E_1 and E_2 in the presence of a light wave of angular frequency

ω. We shall assume that the light is very close to resonance with the transition, so that

$$\omega = \omega_0 + \delta\omega \qquad\qquad\qquad Eq(1.5)$$

Where

$$\omega_0 = \frac{(E_2 - E_1)}{\hbar} , \text{ and } \delta\omega << \omega_0 \qquad\qquad\qquad Eq(1.6)$$

Exact resonance thus corresponds to $\delta\omega = 0$, We start by splitting the Hamiltonian into a

time-independent part $\hat{H}_0$ which describes the atom in the dark, and a perturbation term $\hat{V}(t)$ which

accounts for the light–atom interaction:

$$\hat{\tilde{\tilde{H}}} = H_0(r) + V(t) \qquad\qquad\qquad Eq(1.7)$$

Since we are dealing with a two-level atom, there will be two solutions for the unperturbed

system:

$$\hat{H}_0 \Psi_i = i\hbar \frac{\partial \Psi_i}{\partial t} \qquad\qquad \text{Eq(1.8)}$$

with $\Psi_i(r,t) = \psi_i(r)\exp(-iE_i t/\hbar) \quad \{i=1,2\}$ Eq(1.9)

and $\hat{H}_0(r)\psi_i(r) = E_i\psi_i(r) \quad \{i=1,2\}$ Eq(1.10)

The general solution to the time-dependent Schrödinger equation is:

$$\Psi(r,t) = \sum_i c_i(t)\psi_i(r)\exp(-i\,E_i t/\hbar) \qquad\qquad \text{Eq(1.11)}$$

where the subscript i runs over all the eigenstates of the system. In the

case of a two-level atom, this reduces to:

$$\Psi(r,t) = c_1(t)\psi_1(r)\exp(-i\,E_1 t/\hbar) + c_2(t)\psi_2(r)\exp(-i\,E_2 t/\hbar) \qquad \text{Eq(1.12)}$$

On substituting this wave function into equation 1.4 with $\hat{H}$ given by equation 1.7,

we obtain:

$$\begin{aligned} & \left(\hat{H}_0 + V\right)\left(c_1\psi_1\,e^{(-iE_1 t/\hbar)} + c_2\psi_2\,e^{(-iE_2 t/\hbar)}\right) \\ & = i\hbar\left(\left(\dot{c}_1 - i\,E_1 c_1/\hbar\right)\psi_1\,e^{(-iE_1 t/\hbar)} + \left(\dot{c}_2 - i\,E_2 c_2/\hbar\right)\psi_2\,e^{(-iE_2 t/\hbar)}\right) \end{aligned} \qquad \text{Eq(1.13)}$$

Now equation 1.10 implies that

$$\begin{aligned} & \hat{H}_0\left(c_1\psi_1\,e^{(-iE_1 t/\hbar)} + c_2\psi_2\,e^{(-iE_2 t/\hbar)}\right) \\ & = c_1 E_1\psi_1\,e^{(-iE_1 t/\hbar)} + c_2 E_2\psi_2\,e^{(-iE_2 t/\hbar)} \end{aligned} \qquad \text{Eq(1.14)}$$

so that we can cancel several of the terms in equation 1.13 to obtain:

$$c_1\hat{V}\psi_1\,e^{(-iE_1 t/\hbar)} + c_2 V\psi_2\,e^{(-iE_2 t/\hbar)} = i\hbar\dot{c}_1\psi_1\,e^{(-iE_1 t/\hbar)} + i\hbar\dot{c}_2\psi_2\,e^{(-iE_2 t/\hbar)} \qquad \text{Eq(1.15)}$$

On multiplying by ψ_1^*, integrating over space, and making use of the orthonormality of the

eigenfunctions, which requires that:

$$\int \psi_i^* \psi_j d^3 r = \delta_{ij} \qquad \text{Eq(1.16)}$$

where δ_{ij} is the Kronecker delta function, we find that:

$$\dot{c}_1(t) = -\frac{i}{\hbar}\left(c_1(t)V_{11} + c_2(t)V_{12}e^{-i\omega_0 t}\right) \qquad \text{Eq(1.17)}$$

Where

$$V_{ij}(t) \equiv \langle i|\hat{V}(t)|j\rangle = \int \psi_i^* V(t)\psi_j d^3 r \qquad \text{Eq(1.18)}$$

Similarly, on multiplying by ψ_2^* and integrating, we find that:

$$\dot{c}_2(t) = -\frac{i}{\hbar}\left(c_1(t)V_{21}e^{i\omega_0 t} + c_2(t)V_{22}\right) \qquad \text{Eq(1.19)}$$

To proceed further we must consider the explicit form of the perturbation $\hat{V}$. In the semi-classical approach, the light–atom interaction is given by the energy shift of the atomic dipole in the electric field of the light:

$$\hat{V}(t) = er \cdot E(t) \qquad \text{Eq(1.20)}$$

We arbitrarily choose the x-axis as the direction of the polarization so that we can write:

$$E(t) = (E_0, 0, 0)\cos(\omega t) \qquad \text{Eq(1.21)}$$

where E_0 is the amplitude of the light wave. The perturbation then simplifies to:

$$\begin{aligned}\hat{V}(t) &= exE_0\cos(\omega t) \\ &= \frac{exE_0}{2}\left(e^{i\omega t} + e^{-i\omega t}\right)\end{aligned} \qquad \text{Eq(1.22)}$$

and the perturbation matrix elements are given by:

$$V_{ij}(t) = \frac{eE_0}{2}\left(e^{i\omega t} + e^{-i\omega t}\right)\int \psi_i^* x\psi_j d^3 r \qquad \text{Eq(1.23)}$$

Now the dipole matrix element μ_{ij} is given by:

$$\mu_{ij} = -e\int \psi_i^* x\psi_j d^3 r \equiv -e\langle i|x|j\rangle \qquad \text{Eq(1.24)}$$

so that we can write:

$$V_{ij}(t) = \frac{-E_0}{2}\left(e^{i\omega t} + e^{-i\omega t}\right)\mu_{ij} \hspace{4cm} \text{Eq(1.25)}$$

Since x is an odd parity operator and atomic states have either even or odd parities, it must be the

case that $\mu_{11} = \mu_{22} = 0$ Moreover, the dipole matrix element represents a measurable quantity and

must be real, which implies that $\mu_{21} = \mu_{12}$, because $\mu_{21} = \mu_{12}^*$

With these simplifications, equation 1.17, 1.19 reduce to:

$$\dot{c}_1(t) = i\frac{E_0\mu_{12}}{2\hbar}\left(e^{i(\omega-\omega_0)t} + e^{-i(\omega+\omega_0)t}\right)c_2(t)$$
$$\dot{c}_2(t) = i\frac{E_0\mu_{12}}{2\hbar}\left(e^{-i(\omega-\omega_0)t} + e^{i(\omega+\omega_0)t}\right)c_1(t) \hspace{2cm} \text{Eq(1.26)}$$

We now introduce the Rabi frequency defined by:

$$\Omega_R = \left|\mu_{12}E_0/\hbar\right| \hspace{4cm} \text{Eq(1.27)}$$

We then finally obtain:

$$\dot{c}_1(t) = \frac{i}{2}\Omega_R\left(e^{i(\omega-\omega_0)t} + e^{-i(\omega+\omega_0)t}\right)c_2(t)$$
$$\dot{c}_2(t) = \frac{i}{2}\Omega_R\left(e^{-i(\omega-\omega_0)t} + e^{i(\omega+\omega_0)t}\right)c_1(t) \hspace{2cm} \text{Eq(1.28)}$$

These are the equations that we must solve to understand the behavior of the atom in the light

field. It turns out that there are two distinct types of solution that can be found, which correspond to

the weakfield limit and the strong-field limit respectively.

1.3.1.1 Strong coupling between photon and exciton

In order to find a solution to equation 1.28 in the strong-field limit we make two simplifications. First, we apply the rotating wave approximation to neglect the terms that oscillate at $\pm(\omega + \omega_0)$, as in the previous section. Second, we only consider the case of exact resonance with $\delta\omega = 0$. With these simplifications, equation 1.28 reduces to:

$$\dot{c}_1(t) = \frac{i}{2}\Omega_R c_2(t)$$
$$\dot{c}_2(t) = \frac{i}{2}\Omega_R c_1(t)$$

Eq(1.29)

We differentiate the first line and substitute from the second to find:

$$\ddot{c}_1 = \frac{i}{2}\Omega_R \dot{c}_2 = \left(\frac{i}{2}\Omega_R\right)^2 c_1$$

Eq(1.30)

We thus obtain

$$\ddot{c}_1 + \left(\frac{\Omega_R}{2}\right)^2 c_1 = 0$$

Eq(1.31)

which describes oscillatory motion at angular frequency $\dfrac{\Omega_R}{2}$. If the particle is in the lower level at t = 0 so that $c_1(0) = 1$ and $c_2(0) = 0$, the solution is:

$$c_1(t) = \cos(\Omega_R t/2)$$
$$c_2(t) = i\sin(\Omega_R t/2)$$

Eq(1.32)

The probabilities for finding the electron in the upper or lower levels are then given by:

$$|c_1(t)|^2 = \cos^2(\Omega_R t/2)$$
$$|c_2(t)|^2 = \sin^2(\Omega_R t/2)$$

Eq(1.33)

The time dependence of these probabilities is shown in fig 1.7. At $t = \pi/\Omega_R$ the electron is in

the upper level, whereas at $t = 2\pi/\Omega_R$ it is back in the lower level. The process then repeats itself

with a period equal to $2\pi/\Omega_R$. The electron thus oscillates back and forth between the lower and

upper levels at a frequency equal to $\Omega_R/2\pi$. This oscillatory behaviour in response to the strong-field

is called Rabi oscillation or Rabi flopping. When the light is not exactly resonant with the transition, it

can be shown that the second line of equation 1.33 is modified to:

$$|c_2(t)|^2 = \frac{\Omega_R^2}{\Omega^2} \sin^2(\Omega t/2) \qquad \text{Eq(1.34)}$$

where

$$\Omega^2 = \Omega_R^2 + \delta\omega^2 \qquad \text{Eq(1.35)}$$

$\delta\omega$ being the detuning. This shows that the frequency of the Rabi oscillations increases but their

amplitude decreases as the light is tuned away from resonance. For transitions in the visible-frequency

range, the experimental observation of Rabi flopping requires powerful laser beams. In many cases,

these lasers will be pulsed, so that the electric field amplitude E_0 varies with time. Equation 1.27

then tells us that the Rabi frequency $\Omega_R/2\pi$

also varies with time, and so it is useful to define the pulse area Θ according to:

$$\Theta = \left| \frac{\mu_{12}}{\hbar} \int_{-\infty}^{+\infty} E_0(t)\,dt \right| \qquad \text{Eq(1.36)}$$

The pulse area is a dimensionless parameter which is determined by the pulse energy and serves

the same purpose as $\Omega_R t$ in the analysis above. A pulse which has an area equal to π is called a

π-pulse. An atom in the ground state with $c_1(0) = 1$ will thus be promoted to the excited state with

$c_2(0) = 0$, by a π-pulse, but will end up back in the ground state if it interacts with a 2π-pulse.

1.3.2   Weak coupling between photon and exciton

Weak coupling between two systems refers to the regime opposed to strong coupling where dissipation dominates over the system interaction so that the coupling between the modes can be dealt with pertubatively and both modes retain essentially their uncoupled properties.

With a low-intensity source, the electric field amplitude will be small and the perturbation weak. The number of transitions expected is therefore small, and it will always be the case that $c_1(t) \gg c_2(t)$. In these condition, we can get the solution of equation 1.28:

$$
\begin{aligned}
\left| c_1(t) \right|^2 &= 1 \\
\left| c_2(t) \right|^2 &= \left(\frac{\Omega_R}{2} \right)^2 t^2
\end{aligned}
\qquad \text{Eq(1.37)}
$$

The weak coupling between exciton and light manifests itself in the appearance of the splitting between the imaginary parts of the eigenfrequencies of exciton-polariton modes at the resonance between bare exciton and photon modes. In this regime the real parts of two polariton eigenfrequencies coincide at the resonance, and two polariton resonances in the reflection or transmission spectra usually coincide, [17].

1.4 Difference Of Material In Semiconductor Microcavity

Semiconductor microcavities have recently attracted much attention because of the control that they provide on the light-matter interaction in solid-state systems. In the strong coupling regime, excitons and photons form new coupled modes—the cavity polaritons—exhibiting large nonlinearities

which open the way to a broad area of fundamental and applied investigations.

The first observations of exciton–polaritons in microresonators were reported for GaAs and CdTe-based resonators at low temperatures (T < 30 K) [19, 20, 21]. In these materials, the exciton binding energy is smaller than the thermal energy at RT and excitons are not stable at RT. Therefore, many efforts have been made to obtain microresonators with gain media that reveal an exciton binding energy larger than the thermal energy at RT, such as organic semiconductors [22, 23], or GaN [24, 25, 26] and ZnO [27, 28, 29]. The advantage of organic semiconductors is their huge exciton oscillator strength resulting in a large coupling strength between the excitons and the cavity photons. However, often the low crystal quality of such materials leads to emission spectra that are superposed from the emission from localized and delocalized states. In contrast, inorganic semiconductors reveal high crystal qualities with an emission from well-defined exciton states. Here, GaN and ZnO are the most prominent candidates that are considered for high temperature applications. ZnO offers some advantages, since it reveals the largest exciton oscillator strength of the technologically relevant semiconductors, about three times larger than that of GaN [30 ,31], and its exciton binding energy is about twice the thermal energy at RT.

The critical temperature is determined by the Rydberg energy of exciton, oscillator strength, etc. Most of those factors are depended on the material properties. Table 1.2 shows several common semiconductor materials, including GaAs, GaN, and ZnO. GaN and ZnO are the well-known wide-bandgap material used in microcavity, which have the higher Rydberg energy than, 30meV and

60meV, respectively. That is to say, at room temperature, more excitons exist in the room temperature in GaN and ZnO microcavity.

1.4.1   GaAs-Based Microcavity

The choice of a direct band-gap semiconductor depends first on the fabrication technology. The best fabrication quality of both quantum well and microcavity has been achieved via molecular-beam epitaxy growth of $Al_xGa_{1-x}As$-based samples $(0 \leq x \leq 1)$, thanks to the close match of the lattice constants a_{lat} of AlAs and GaAs and a relatively large difference between their band-gap energies E_g. At 4K, GaAs has a_{lat}=5.64 Å and E_g=1.519 eV and AlAs has a_{lat}=5.65 Å and E_g=3.099 eV. Nearly strain and defect-free GaAs QWs are now conventionally grown between $Al_xGa_{1-x}As$. Inhomogeneous broadening of exciton energy is limited mainly by monolayer QW thickness fluctuation. Nearly defect-free microcavity structures can be grown with more than 30 pairs of AlAs/GaAs layers in the DBRs and with a cavity quality factor Q exceeding 10^5 [32]. Many signatures of polariton condensation were first obtained in GaAs-based systems , [33, 34, 35], as shown in Fig 1.8 .

1.4.2   CdTe-based Microcavity

Another popular choice is the CdTe-based II-IV system, with CdTe QWs and $Mg_xCd_{1-x}Te$ and $Mn_xCd_{1-x}Te$ barrier and DBR layers. The larger lattice mismatch is compensated by larger binding

energy and larger oscillator strength, as well as larger refractive index contrast (hence less layers needed in the DBRs). The smaller Bohr radius of CdTe excitons, on the one hand, allows a larger saturation density and, on the other hand, reduces the polariton and acoustic phonon scattering. Hence the energy relaxation bottleneck is more persistent in this system, which prevented condensation in the LP ground state in early experiments, [37, 38]. By adjusting the detuning to facilitate thermalization, partially localized polariton condensation into the ground state was finally observed in 2006, [39] , as shown in fig 1.9.

1.4.3   GaN-Based Microcavity

GaN-based MCs are beginning to receive interest in the research community. A realistic model for room temperature polariton laser has been proposed for a GaN MC by Malpuech [40]. In the preceding report, the model structure was a $3\lambda/2$ MC which consisted of a cavity layer with 4 monolayers thick 9 QWs between $Al_{0.2}Ga_{0.8}N/Al_{0.9}Ga_{0.1}N$ DBRs, 11 pairs on the top and 14 pairs at the bottom. The critical temperature of BEC of cavity polaritons was predicted to be 460 K with a room temperature polariton lasing threshold as small as 100mW. Several groups have already reported polariton luminescence at room temperature from bulk [41, 42, 43, 44] and QW MCs. The first experimental results of the strong coupling regime in GaN-based MCs were reported by Antoine-Vincent et al, [45]. The MCs fabricated by a wafer-bonding technique was composed of $In_{0.15}Ga_{0.85}N/In_{0.02}Ga_{0.98}N$ QWs embedded in a GaN-based cavity layer sandwiched between two

SiO$_2$/ZrO$_2$ DBRs. The anticrossing behavior was observed by angle-resolved reflectivity measurements showing a vacuum Rabi splitting of 6 meV. By increasing the number of QWs from 3 to 10, the vacuum Rabi splitting was increased to 17 meV. An impediment for strong coupling regime in this particular InGaN QW-MC was a low finesse cavity and/or large inhomogeneous broadening of the QW emission, [46]. Bulk GaN-based MCs were further studied for polariton emission in the strong coupling regime [41, 42, 43, 44]. In a bulk GaN MC with lattice matched AlInN/(Al)GaN DBRs, a strong bottleneck effect was observed at room temperature by photoluminescence (PL) measurements [43]. In an attempt to use ubiquitous Si substrates, bulk GaN MCs with a 10 pair AlN/Al0.2Ga0.8N DBR have been grown directly on Si (111),[41, 42]. A vacuum Rabi splitting of approximately 50 meV was observed up to room temperature by angle-resolved reflectivity and PL measurements. A vacuum Rabi splitting of 43 meV in GaN hybrid MCs in the strong coupling regime was reported by Alyamani et al, [44]. despite a cavity Q factor of about 160 or less. A GaN/Al$_{0.2}$Ga$_{0.8}$N QW-MC with a sharper linewidth enabled observation of cavity polaritons at room temperature using angle-resolved PL [47]. A vacuum Rabi splitting of 30 meV was observed and the exciton oscillator strength was estimated to be $\sim 3 \times 10^{13}$ cm^{-2} per QW.

Room temperature polariton lasing in a bulk GaN MC under nonresonant pulsed optical pumping has been demonstrated by Christopoulos et al, [48]. The 3λ/2 bulk GaN cavity was sandwiched between a bottom 34 pair Al$_{0.85}$In$_{0.15}$N/Al$_{0.2}$Ga$_{0.8}$N DBR and a top 10 pair SiO$_2$/Si$_3$N$_4$ DBR. The Q factor obtained was $\sim$ 2800. The optimum pumping occurred in resonance with the first Bragg mode

above the upper DBR stop band, and the system in the strong coupling regime was confirmed by the observed anti-crossing behavior from angleresolved PL. A clear nonlinear behavior is seen for the emission at $\lambda \approx 365$ nm above the critical threshold of $I_{th} = 1.0$ mW. This corresponds to a carrier density of $N_{3D} \sim 2.2 \times 10^{18}$ cm^{-3}, which is an order of magnitude below the Mott density $\approx 1 - 2 \times 10^{19}$ cm^{-3} in GaN at 300 K. Additionally, the emission line was observed to blueshift with increasing pump power and lock at threshold due to polariton-polariton interactions.

Further challenging, room temperature strong coupling regime and nonlinear effects in GaN-based QWs MCs were studied. Christmann et al [49, 50, 51]. employed GaN-based hybrid MCs which consist of a 3λ cavity layer with 67 period of GaN/Al$_{0.2}$Ga$_{0.8}$N MQWs sandwiched between a 35 pair of lattice-matched Al$_{0.85}$In$_{0.15}$N/Al$_{0.2}$Ga$_{0.8}$N DBR and a 10 pair SiO$_2$/Si$_3$N$_4$ DBR. Due to high quantum efficiency, InGaN-based emitting devices are commonly used. However, large inhomogeneous broadening of QWs at room temperature is a serious problem in efforts to attain the strong coupling regime, [52]. By comparison, GaN/AlGaN QWs have a narrower emission linewidth with a broadening of ~ 38 meV which is capable of paving the way for achieving the strong coupling regime. In the lattice-matched GaN/AlGaN QWs MC system, the strong coupling regime at room temperature was demonstrated using angle-resolved reflectivity measurements observed at small angles followed by an asymptotic trend towards the uncoupled exciton energy (X). Anticrossing between the lower polariton branch (LPB) and the upper polariton branch (UPB) was observed at 17°, confirming that the system is in the strong coupling regime. The vacuum Rabi splitting of 56 meV is

observed at room temperature. In order to observe the nonlinear optical properties, MCs were nonresonantly excited by a pulsed laser (λpump = 266 nm). Fig. 1.10 (a) shows a series of emission spectra at average pump power densities ranging from 0.16 to 28.8 W/cm^2 at k// = 0. The nonlinear behavior is clearly observed at a relatively low threshold pump power density ~18 W/cm^2, corresponding to a calculated density of 8×10^9 cm^{-2} per QW. This threshold pump power density is ~ 1/3 smaller than that in GaN-based VCSELs [53]. It should note that a further increase of the pump power results in broadening of the emission peak due to increasing polariton-polariton interactions occurring in the condensates. Above threshold, the linewidth reduced from ~15 meV to ~ 0.46 meV.

In a perfect polariton laser, polarization should randomly change for each realization of condensate. Baumberg et al. observed the spontaneous polarization build up in room temperature GaN-based polariton lasers excited by short optical pulses [54]. The Stokes vector of the emitted light changes its orientation randomly from one excitation pulse to the other. Although it was unpolarized below threshold, the polartization of polariton emission above threshold are linearly polarized, but with no preferential orientation. This behavior is completely different from any conventional laser including VCSELs. A spontaneous build up of polarization could be interpreted as spontaneous symmetry breaking in a Bose-Einstein condensate of exciton-polaritons.

Interest is now brought to wide band-gap materials because the strong coupling regime is stable up to room temperature and the exciton binding energy is much larger, leading to stronger nonlinearities. The realization of a GaN-based polariton laser operating at room temperature has been

achieved.

1.4.4   ZnO-Based Microcavity

Another wide bandgap semiconductor, ZnO is an attractive candidate for ultraviolet (UV)

optoelectronics devices. ZnO has an exciton binding energy (60 meV) that is more than twice that of

GaN (~26 meV). Zamfirescu et al [55]. predicted a large Vacuum Rabi splitting ~120 meV for cavity

polaritons in a model ZnO MC sandwiched between $Mg_{0.3}Zn_{0.7}O/ZnO$ DBRs, which projects to an

extremely low threshold polariton laser (~2 mW) at room temperature. A record of ~191 meV has been

predicted but not yet experimentally observed [56]. On the reflector side, Chichibu et al. reported high

reflectivity SiO_2/ZrO_2 DBRs for ZnO based MCs owing to the large refractive index contrast between

SiO_2 and ZrO_2, giving rise to a high reflectivity (> 99%) and a wide stop band even for an 8 pair

SiO_2/ZrO_2 DBR. Recently, ZnO-based MCs were grown by different growth techniques and tested

under optical pumping. Shimada et al, [58, 59, 60]. observed a vacuum Rabi splitting of 50 meV in

ZnO-based hybrid MCs grown by molecular beam epitaxy (MBE) sandwiched between a 29 pair of

AlGaN/GaN bottom DBR and an 8 pair dielectric (SiO_2/SiN_x) top DBR [58]. Fig. 1.11 (a) shows the

angle-resolved PL spectra at room temperature up to 40°. It is clear that the lower polariton mode gets

closer to the uncoupled exciton mode, and the upper polariton mode is dispersed from the exciton

mode to the cavity mode. The experimental cavity polariton dispersion curve shown in Fig. 1.11 (b)

exhibits a typical anti-crossing behavior between the cavity mode and exciton mode when the cavity

mode energy crosses the exciton mode. Schmidt-Grund et al. grew λ/2-thick ZnO-based planar MCs which consist of a ZnO cavity layer surrounded by a 10.5 pair ZrO_2/MgO DBR prepared by pulsed-laser deposition (PLD). A large vacuum Rabi splitting of ~ 78 meV was obtained from angle-resolved reflectivity and PL measurements [59]. Using a dielectric MC consisting of a λ-thick ZnO cavity layer and two HfO_2/SiO_2 DBRs by PLD and RF magnetron sputtering, respectively, cavity polariton formation was demonstrated by Nakayama et al [60]. The vacuum Rabi splitting energy was estimated ~ 80 meV. However, no polariton lasing was reported in any ZnO-based MCs as of yet. Nevertheless, the above mentioned results are promising towards the realization of room temperature ZnO-based polariton devices [61]. Moreover, ZnO-based electrical injection polariton lasers may also be realizable in the future when reproducible and reliable p-type conductivity is achieved in ZnO. [62, 63]
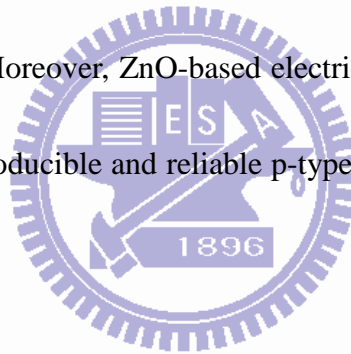
1.4.4.1   Material Characteristics Of Zinc-Oxide

In recent years, the desire for blue and UV diode lasers and light emitting diodes has prompted enormous research efforts into II–VI and III–V wideband gap semiconductors. Among the well-known semiconductor materials employed in various technical applications, two unique positions are held by gallium nitride (GaN) and zinc oxide (ZnO) in the wide direct band gap semiconductor. In the material property, both GaN and ZnO have many similar aspects, such as material structure, lattice constant, energy band gap,… etc.. In the difference of which, the remarkable property of ZnO better than GaN is

exciton binding energy of 60 meV, which is only 30 meV for GaN. Owing to the larger exciton binding energy, more excitons exist in the room temperature, resulting in higher luminescence than GaN. Furthermore, ZnO can be grown at lower temperature on the cheaper substrate and lead to low cost of growth. However, because of more intrinsic defects, the hard growth of p-type ZnO to achieve the p-i-n junctions, and the degradation of material quality, the current commercial blue and UV LEDs are primitively composed of GaN. However, GaN-based LEDs still face some problems of the luminescence, such as more defects in the material and low electron-hole recombination of c-direction growth. Therefore, it is worth making the further researches on the material of ZnO and GaN on purpose of possessing well-performed LEDs and LDs.

In materials science, ZnO is often called a II-VI semiconductor because zinc and oxygen belong to the 2nd and 6th groups of the periodic table, respectively. This semiconductor has several favorable properties: good transparency, high electron mobility, wide band-gap, strong room-temperature luminescence, etc.

Zinc oxide crystallizes is hexagonal wurtzite, as shown in Fig1.12(a). The hexagonal structure has a point group $6^\circ mm$ or C_{6v}, and the space group is $P6_3mc$ or C_{6v}^4. The lattice constants are a = 3.25 Å and c = 5.2 Å; their ratio c/a ~ 1.60 is close to the ideal value for hexagonal cell c/a = 1.633. As in most II-VI materials, the bonding in ZnO is largely ionic, which explains its strong piezoelectricity. Due to this ionicity, zinc and oxygen planes bear electric charge (positive and negative, respectively).

ZnO has a relatively large direct band gap of ~3.3 eV at room temperature; therefore, pure ZnO is

colorless and transparent. Advantages associated with a large band gap include higher breakdown voltages, ability to sustain large electric fields, lower electronic noise, and high-temperature and high-power operation. The bandgap of ZnO can further be tuned from ~3–4 eV by its alloying with magnesium oxide or cadmium oxide.

Most ZnO has n-type character, even in the absence of intentional doping. Native defects such as oxygen vacancies or zinc interstitials are often assumed to be the origin of this, but the subject remains controversial. An alternative explanation has been proposed, based on theoretical calculations, that unintentional substitutional hydrogen impurities are responsible. Controllable n-type doping is easily achieved by substituting Zn with group-III elements Al, Ga, In or by substituting oxygen with group-VII elements chlorine or iodine. Reliable p-type doping of ZnO remains difficult. This problem originates from low solubility of p-type dopants and their compensation by abundant n-type impurities, and it is pertinent not only to ZnO, but also to similar compounds GaN and ZnSe. Measurement of p-type in "intrinsically" n-type material is also not easy because in-homogeneity results in spurious signals.

Current absence of p-type ZnO does limit its electronic and optoelectronic applications which usually require junctions of n-type and p-type material. Known p-type dopants include group-I elements Li, Na, K; group-V elements N, P and As well as copper and silver. However, many of these form deep acceptors and do not produce significant p-type conduction at room temperature.

ZnO has wide direct band gap (3.37 eV or 375 nm at room temperature). Therefore, it's most

common potential applications are in laser diodes and light emitting diodes (LEDs). Some

optoelectronic applications of ZnO overlap with that of GaN, which has a similar bandgap (~3.4 eV at

room temperature). Compared to GaN, ZnO has a larger exciton binding energy (~60 meV, 2.4 times

of the room-temperature thermal energy), which results in bright room-temperature emission from

ZnO. Recent studies of ZnO epilayers have observed spontaneous emission from free-exciton (FE)

radiative recombination as well as stimulated emission from exciton-exciton scattering (EES) and

electron-hole-plasma (EHP) radiative recombination at temperature up to ~550K.[3] Other properties

of ZnO favorable for electronic applications include its stability to high-energy radiation and to wet

chemical etching. The pointed tips of ZnO nanorods result in a strong enhancement of an electric field.

Therefore, they can be used as field emitters. Transparent thin-film transistors (TTFT) can be produced

with ZnO. As field-effect transistors, they even may not need a p–n junction, thus avoiding the p-type

doping problem of ZnO. Some of the field-effect transistors even use ZnO nanorods as conducting

channels.
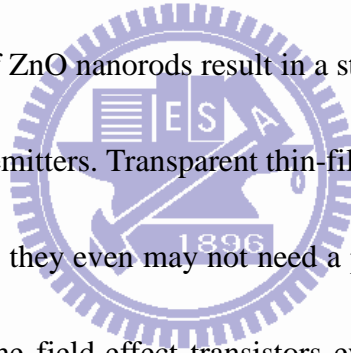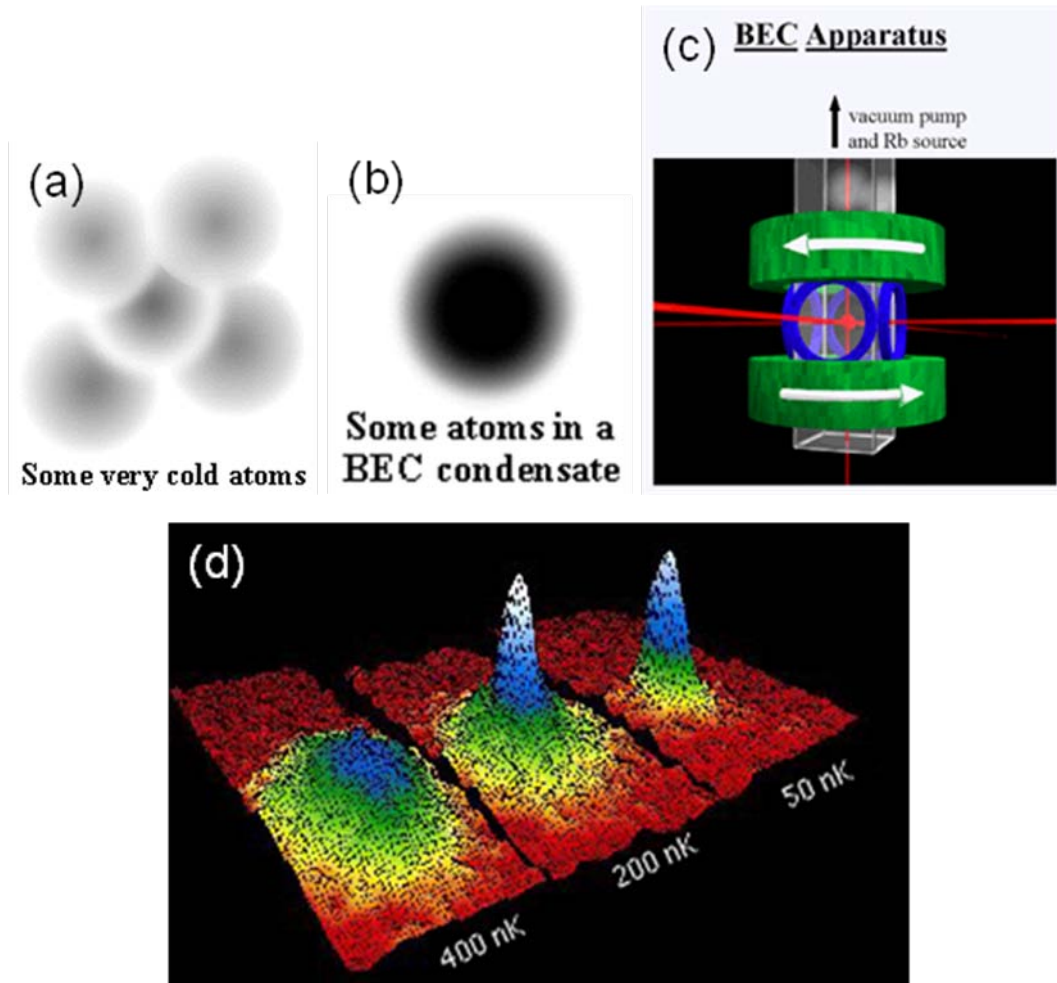
Fig 1.1 (a) Before condensation, the atoms look like fuzzy balls. (b) After condensation, the atoms lie exactly on top of each other . (c) Schematic of the apparatus. Six laser beams intersect in a glass cell, creating a magneto-optical trap (MOT). (d) Bose-Einstein Condensation at 400, 200, and 50 nK.
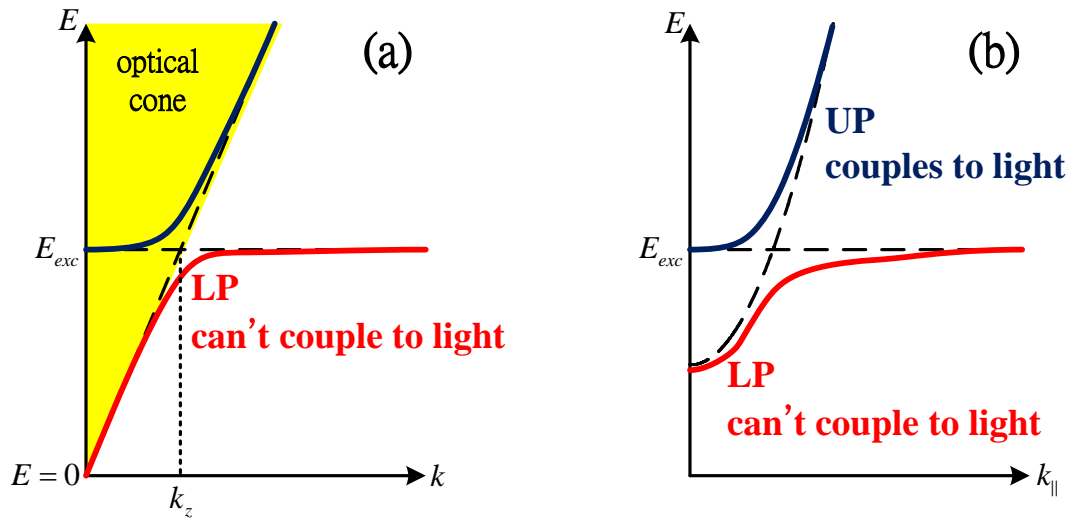
Fig 1.2 (a) the dispersion of bulk polariton (b) the dispersion of microcavity polariton
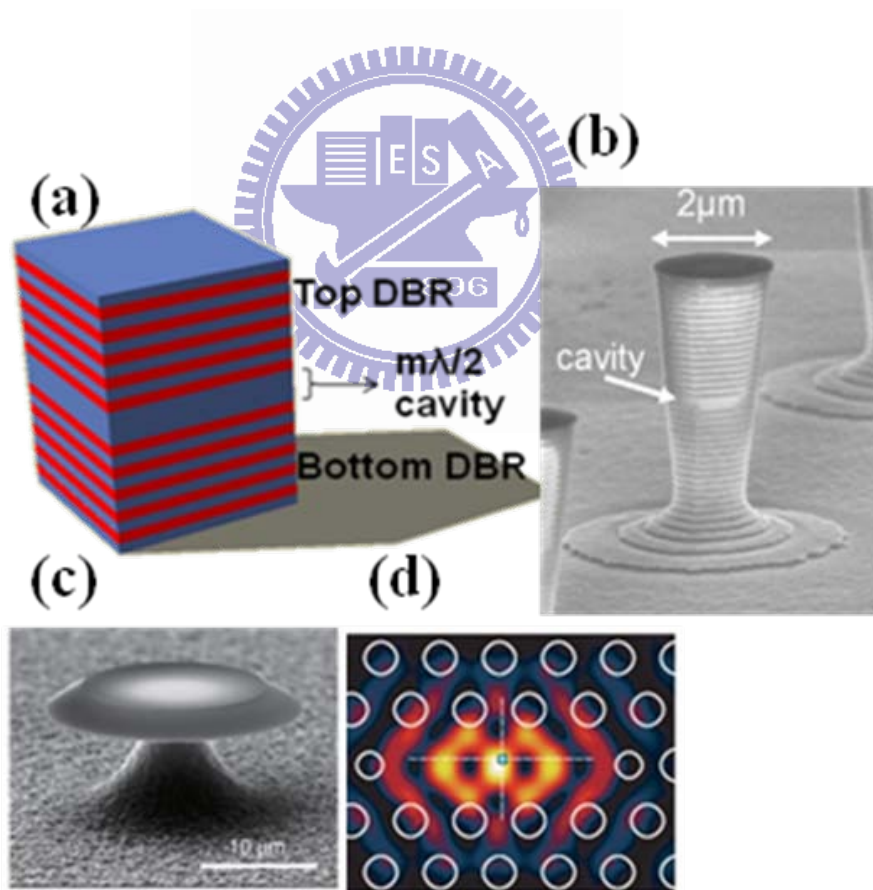
Fig 1.3   The different types of microcavity (a) planar microcavities (b) pillar microcavities [13]

((c) Whispering-gallery microdisk resonator [14] d) photonic-crystal cavity [15]
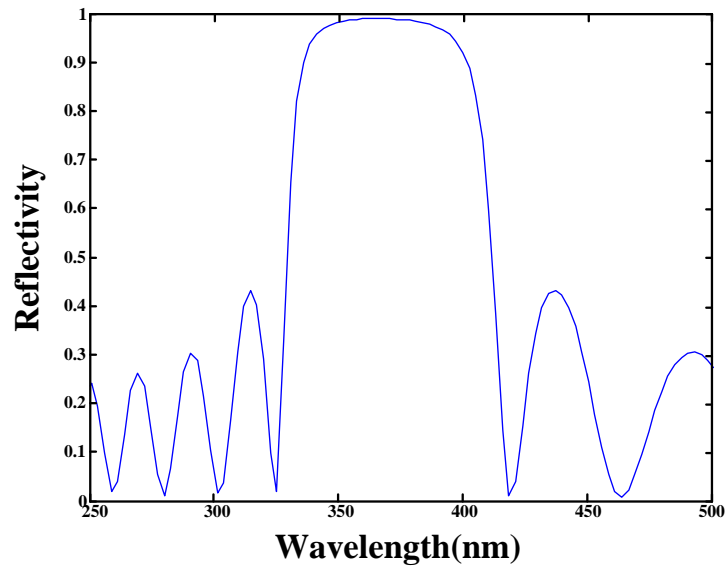
Fig 1.4 DBR reflectivity spectrum with different wavelength
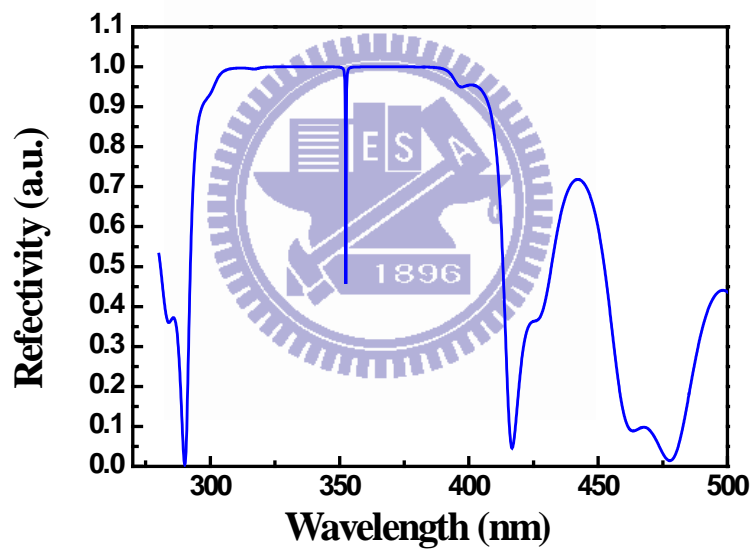
Fig 1.5 Microcavity reflectivity spectrum with different wavelength

$$E_2 - E_1 = \hbar\omega$$
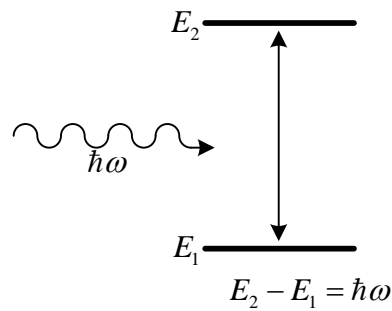
Fig 1.6 Schematic of two level system
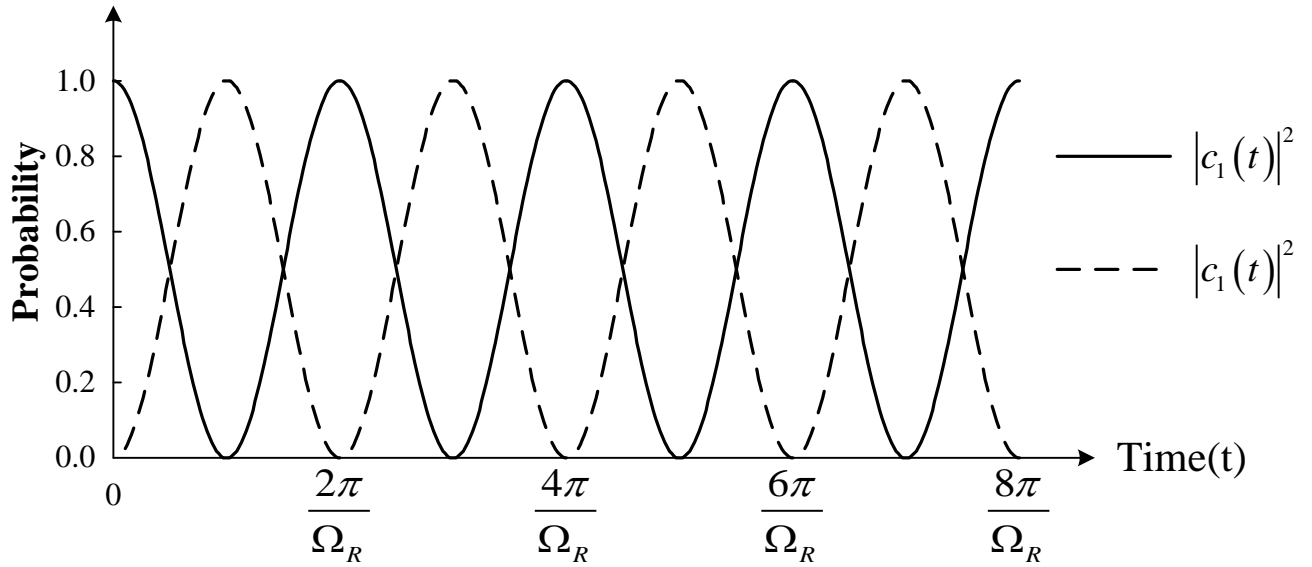
Fig 1.7. Probability for finding the atom in either the upper or lower level in the strong-field limit in the absence of damping. The electron oscillates back and forth between the two levels at the Rabi angular frequency, Ω_R. This phenomenon is either called Rabi flopping or Rabi oscillation, [16].
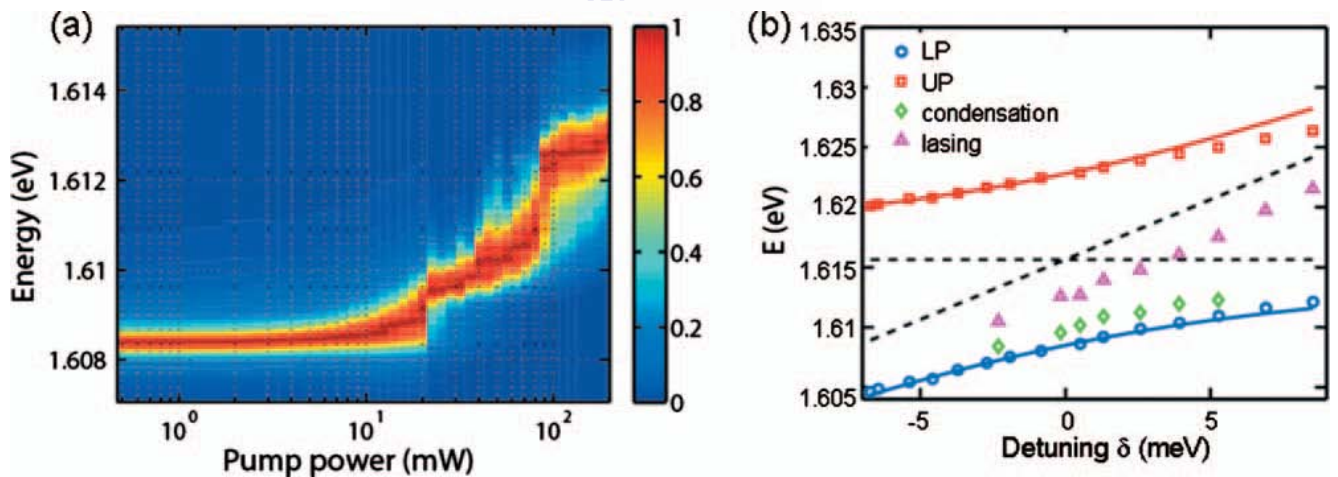
Fig1.8 □Polariton lasing and photon lasing. (a) The emission energy vs pump power for a N=12 multi-QW planar microcavity. (b) The dispersion characteristics of polariton BEC (green diamond) and photon lasing □(pink triangle) as well as the linear dispersion of UP (red square) and LP (blue circle) at low pump power, [36].
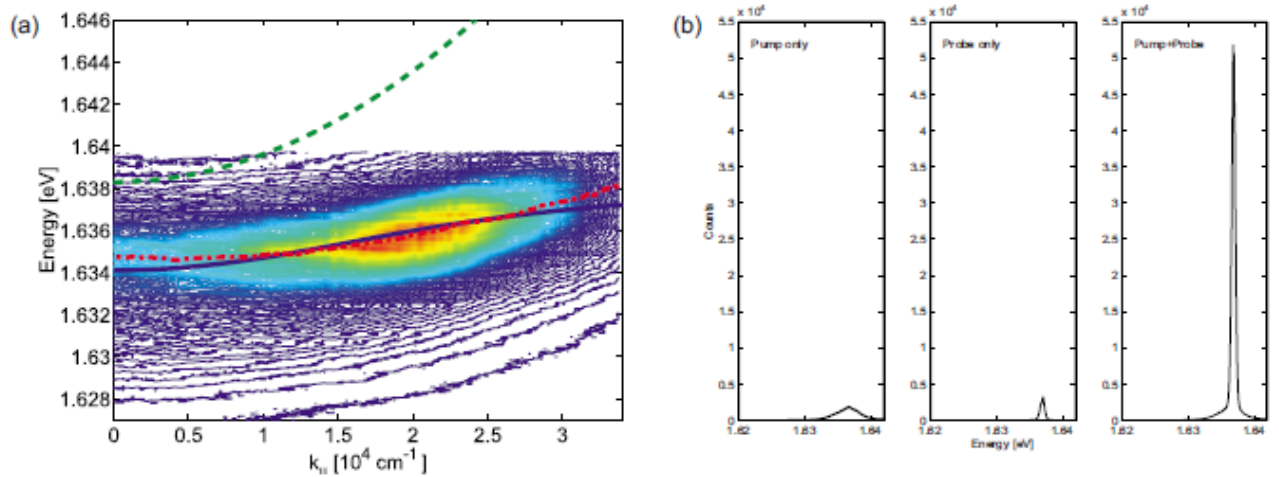
Fig 1.9 A negative conductance polariton amplifier. (a) The LP emission intensity taken as a function of energy and in-plane wave vector. The system is above the quantum degeneracy threshold at the bottleneck. The solid line and the dashed line indicate the theoretical dispersion (b) Observed probe emission for pump only, probe only, and simultaneous pump and probe excitation, [37].
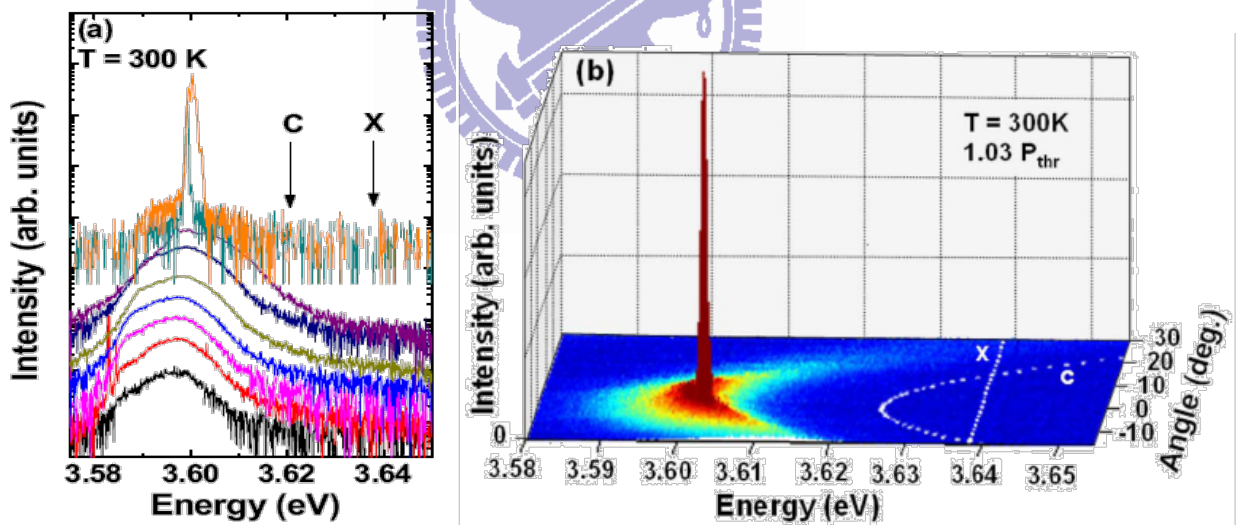
Fig 1.10(a) Semi-logarithmic plot displaying RT emission spectra at average pump power densities ranging from 0.16 to 28.8 W/cm^2, shifted for clarity. C and X are also reported (arrows). (b) Three-dimensional representation of the far-field emission with emission intensity displayed on the vertical axis □linear vertical scale above threshold. C and X are also reported□(white lines).
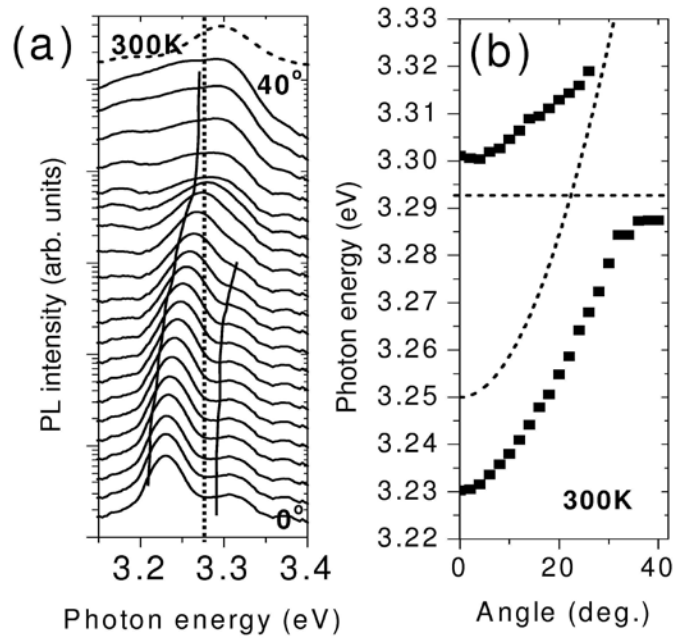
Fig. 1.11 (a) Angle-resolved PL spectra at RT in the range of 0 ° to 40 ° for a ZnO hybrid MC. The

dotted line is the exciton mode. The solid lines are guides to the eye. (b) Experimental cavity olariton

dispersion curve. The dashed lines represent the cavity and exciton modes. (Courtesy of R. Shimada).
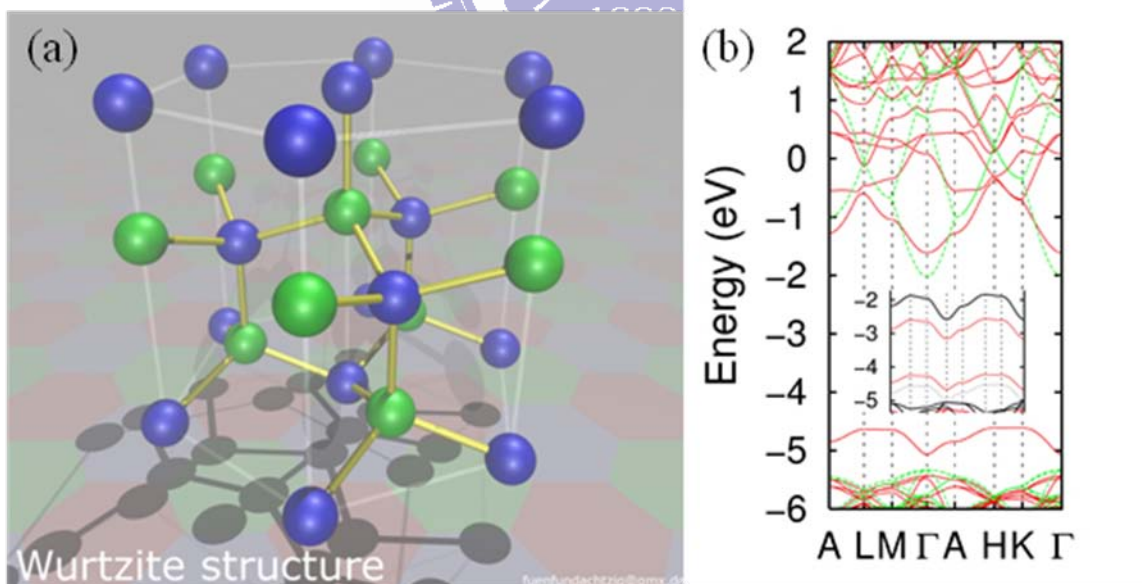
Fig 1.12 (a) Structure of wurtzite, which is a member of the hexagonal crystal system and consists

of tetrahedrally coordinated zinc and sulfur atoms that are stacked in an ABABAB pattern. (b) the

bangap structure of wurtzite structure

systems	atomic gases	excitons	polaritons
effective mass m^*/m_c	10^3	10^{-1}	10^{-5}
Bohr radius a_B	10^{-1} Å	10^2 Å	10^2 Å
particle spacing: $n^{-\frac{1}{d}}$	10^3 Å	10^2 Å	$1\mu m$
critical temperature T_c	1nK~1µK	1mK~1K	1K~>300K
$\dfrac{\text{thermalization time}}{\text{lifetime}}$	1ms/1s~10^{-3}	1ps/1ns~10^{-2}	(1~10ps)/(1~10ps) =0.1~10

Table 1.1: Parameter Comparison of BEC Systems

Material	Bandgap	Exciton binding energy	Rabi splitting	Advantages	Drawbacks
GaAs	1.519eV	~10meV	4meV	lattice-match DBR crystal quality	small exciton binding energy
GaN	3.507eV	~26meV(Bulk) ~40meV(QW)	26meV	large exciton binding energy	QCSE in QW lattice-mismatch DBR crystal quality
ZnO	3.289eV	~60meV	120meV	large exciton binding energy	lattice-mismatch DBR crystal quality

Table 1.2: Comparison of material use in exciton-polariton BEC Systems

Chapter2. THE COUPLING BETWEEN EXITON WITH PHOTON

2.1 Quasi-particle model

2.1.1   Properties of Wannier-Mott Exciton

A solid consists of 10^{23} atoms. Instead of describing the 10^{23} atoms and their constituents in full detail, the common approach is to treat the stable ground state of an isolated system as a quasi-vacuum (the state with filled valence band and empty conduction band for a semiconductor) and to introduce quasi-particles as a unit of elementary excitation, which only weakly interact with each other. An exciton is a typical example of such a quasi-particle, consisting of an electron and a hole bound by the Coulomb interaction. The quasi-vacuum of a semiconductor is the state with filled valence band and empty conduction band. When an electron with charge $-e$ is excited from the valence band into the conduction band, the vacancy it leaves in the valence band can be described as a quasi-particle call a 'hold '. A hole in the valence band has charge $+e$, and an effective mass defined by $-\left(\dfrac{\partial^2 E}{\partial p^2}\right)^{-1}$. A hole and an electron at $p \sim 0$ interacts with each other via Coulomb interaction and form a bound pair (an exciton) analogous to a hydrogen atom where an electron is bound to a proton. The envelope wavefunction of an exciton is also analogous to that of a hydrogen atom. However, due to the strong dielectric screening in solids and a small effective mass ratio of the hole to the electron, the binding energy of an exciton in GaAs, GaN, and ZnO is on the order of 10 meV, 26meV, and 60meV, respectively, three orders of magnitude smaller than that of hydrogen atoms, and the radius of an exciton is about extending over tens of atomic sites in the crystal (Wannier-Mott exciton).

An exciton can be classified into Wannier-Mott exciton and Frenkel exciton, depending on the properties of the material in question, as shown in Fig 2.1. In Wannier excitons, typically observed in covalent semiconductors and insulators, the electron and hole are separated by a distance much larger than the atomic spacing, so that the effect of the crystal lattice on the exciton can be taken into account primarily via an average permittivity.

An exciton is a typical example of such a quasi-particle, consisting of an electron and a hole bound by the Coulomb interaction. Therefore, an effective is that of a hydrogen-like atom formed by an electron and a hole interacting, though simplified picture of the exciton state. The energy of exciton $E_{n=}R_y^* \cdot \frac{1}{n^2}$ Ry is the Rydberg energy.Following Hanamura and Haug [64], the Hamiltonian of the electronic system of a direct two-band semiconductor is:

$$\hat{\hat{H}} = \int \hat{\psi}^{*3}(x)H_0(x)\psi(x)d\,x$$
$$+\frac{1}{2}\hat{\psi}^{**3}(x)\hat{\psi}\,(y)\hat{V}(x-y)\psi(x)\psi(y)d\,xd\,y \qquad \text{Eq(2.1)}$$

Where $\hat{H}_0(x)$ is the Hamiltonian of single electrons, $\hat{V}(x)=e^2/\varepsilon|x|$ is the screened Coulomb potential, and ψ is the field operator for electrons expanded in terms of the electron eigenfunctions $\psi_{kj}(x)$:

$$\hat{\psi}(x) = \sum_{j=c,v;k} \hat{a}_{kj}\psi_{kj}(x) \qquad \text{Eq(2.2)}$$

$$\psi_{kj}(x) = \mu_{kj}(x)\exp(ik\cdot x)/\sqrt{N} \qquad \text{Eq(2.3)}$$

Here $j=c,v$ denotes the conduction or valence band, $\mu_{kj}(x)$ is the Block wavefunction and N is the number of unit cells of the lattice. $\hat{a}_{kj}$ is the fermionic annihilation operator for an electron. It

obeys the commutation relations $\{\hat{a}_k, a_l^\dagger\} = \delta_{k,l}$ and $\{\hat{a}_{kj}, a_{lj}\} = 0$. For the valence band, we introduce

the hole creation operator $\hat{b}_{-k}$ to replace the electron annihilation operator:

$$\hat{a}_{kv}^\dagger = \hat{b}_{-k} \qquad \text{Eq(2.4)}$$

Annihilation of a valence band electron in a state with a wavevector k, spin σ, charge $-e$

and kinetic energy $-E(k)$ from the top of the valence band is equivalent to creation of hole in state

$-k$ with flipped spin $\bar{\sigma}$, positive charge $+e$ and kinetic energy $E(k)$. For the conduction band,

we can now simplify the denotation as:

$$\hat{a}_{kc} = a_k \qquad \text{Eq(2.5)}$$

Substitute eqn to eqn into eqn, neglecting number non-conserving term, we obtain:

$$\begin{aligned}
\hat{H} &= \sum E_e(k)\hat{a}_k^{*\dagger} a_k + \sum E_e(k)\hat{b}_k^{\hat{}} b_k \\
&+ \frac{1}{2}\sum V_{k_1 k_2 k_3 k_4}^{cc\,c\,c} \hat{a}_{k_1}^{*\dagger}\hat{a}_{k_2}^{*\dagger} a_{k_3} a_{k_4} - \frac{1}{2}\sum V_{-k_1 -k_2 -k_3 -k_4}^{v\,v\,v\,v} \hat{b}_{k_1}^{\hat{}}\hat{b}_{k_2}^{\hat{}} b_{k_3} b_{k_4} \\
&- \sum\left(V_{k_1 k_3 k_2 k_4}^{cv\,v\,c} - V_{k_1 k_3 k_4 k_2}^{cv\,c\,v}\right)\hat{a}_{k_1}^{*\dagger}\hat{b}_{k_2}^{\hat{}} b_{k_3} a_{k_4}
\end{aligned} \qquad \text{Eq(2.6)}$$

In the effective mass approximation, $E_e(k)$ ($E_h(k)$) are the kinetic energies of an electron (a

hole) with effective mass m_e, (m_h)

$$\begin{aligned}
E_e(k) &= E_g + \frac{\hbar^2 k^2}{2m_e}, \\
E_h(k) &= \frac{\hbar^2 k^2}{2m_h}
\end{aligned} \qquad \text{Eq(2.7)}$$

Where E_g is the bandgap energy. $V_{k_1 k_2 k_3 k_4}^{i\,j\,m\,n}$ are the direct and exchange interactions among

electrons and holes due to the Coulomb potential $\hat{V}$:

$$V_{k_1 k_2 k_3 k_4}^{i\,j\,m\,n} = \langle k_1 i, k_2 j|\hat{V}|k_3 m, k_4 n\rangle \quad (i,j,m,n=c,v) \qquad \text{Eq(2.8)}$$

For Wannier-Mott excitons, the plane wave factor in eqn and the Coulomb potential $\hat{V}$ are

slowly varying functions which charge vary little in one unit cell of the lattice, hence eqn can be calculated by first integrating the Block functions in a unit cell Ω_i, then summing over all unit cells weighted by the planar wave factors. We also nitice that:

$$\int_{v_i} d^3 x \mu^*_{k \approx 0,c}(x) \mu_{k \approx 0,c}(x) \approx 1$$
$$\int_{v_i} d^3 x \mu^*_{k \approx 0,c}(x) \mu_{k \approx 0,v}(x) \approx 0$$

Eq(2.9)

And we find that eqn can be simplified to a form, for example:

$$V^{cv\ v\ c}_{k\ -l'-k'l} = \frac{1}{V^2} \int d^3 x d^3 y \exp\left[i(l-k)\cdot x + i(l'-k')\cdot y\right] \frac{e^2}{\varepsilon|x-y|}$$

Eq(2.10)

Now we consider the general wavefunction of an electron-hole state:

$$|p\rangle = \sum C_{kk'} \hat{a}^\dagger_k \hat{b}_{k'} |vac\rangle$$

Eq(2.11)

Where $|vac\rangle$ is the quasi-vacuum with a full valence band and an empty conduction band. From the eigenvalue equation $H|p\rangle = E|p\rangle$, we obtain the equation for the amplitude $C_{kk'}$:

$$\left(E_e(k) + E_h(k') - E\right) C_{kk'} - \sum \left(V^{cv\ v\ c}_{k\ -l'-k'l} - V^{cv\ c\ v}_{k\ -l'-l-k'}\right) C_u = 0$$

Eq(2.12)

Takinf a Fourier transsfrom of eqn,use eqn, we obtain the Wannier equations [65] for an exciton:

$$\hat{H}_{exc} \phi(x_e, x_h) = E\phi(x_e, x_h),$$
$$\hat{H}_{exc} = -\frac{\hbar^2}{2m_e} \nabla_e - \frac{\hbar^2}{2m_h} \nabla_h + E_g - \frac{e^2}{\varepsilon|x_e - x_h|}$$

Eq(2.13)

The two particle wavefunction is related to the amplitudes $C_{kk'}$ by

$$\phi(x_e, x_h) = \sum C_{kk'} \exp\left(ik \cdot x_e + ik' \cdot x_h\right)$$

Eq(2.14)

We separate the center of mass motion and the relative motion by introducing the new coordinates:

$$r = x_e - x_h, R = \beta_e x_e - \beta_h x_h \qquad \text{Eq(2.15)}$$

Where $\beta_e = m_e/M$, $\beta_h = m_h/M$, $M = m_e + m_h$. Then eqn become:

$$\phi(x_e, x_h) = \phi_n(r)\exp(iK \cdot R)/\sqrt{V} \qquad \text{Eq(2.16)}$$

And the equation of relative motion is:

$$\left(-\frac{\hbar^2}{2m_r}\nabla_r - \frac{e^2}{\varepsilon_0 r} + \varepsilon_{exc,n}\right)\phi_n(r) = 0 \qquad \text{Eq(2.17)}$$

It has the same form as the equation of relative motion for a Hydrogen atom, but the reduced

mass $m_r = \dfrac{m_e m_h}{M}$ is normally four orders of magnitude less than the hydrogen atom mass, and the

Coulomb interaction is screened and reduced by a factor ε_0. These lead to a much larger Bohr radius

and much weaker binding energy of an exciton compared to an hydrogen atom. The total energy of the

pair is:

$$E(K,n) = E_g - \varepsilon_{exc,n} + \frac{\hbar^2 K^2}{2M} \qquad \text{Eq(2.18)}$$

The binding energy of the 1s state is

$$E_B^{3D} \doteq \varepsilon_{exc,1} = \frac{\hbar^2}{2m_r a_B^2 n^2} \qquad \text{Eq(2.19)}$$

And the Bohr radius of the 1s exciton is:

$$a_B^{3D} = \frac{\hbar^2 \varepsilon_0}{e^2 m_r} \qquad \text{Eq(2.20)}$$

Now the exciton operator $e_{K,n}^{\dagger}$ can be defined by inserting eqn into eqn and using

$|p\rangle = e_{K,n}^{\dagger}|vac\rangle$. We obtain:

$$e_{K,n}^{\dagger\dagger\dagger} = \sum_{k,k'}\delta_{K,k+k'}\phi_n\left(\beta_h k -_e k'\right)\hat{a}_k \hat{b}_{k'} \qquad \text{Eq(2.21)}$$

Where $\phi_n(k)$ is the Fourier transform of $\phi_n(x)$. The commutation relations of the exciton

operators are:

$$\left[\hat{\tilde{e}}_{K',n'}, e_{K,n}\right] = 0$$

$$\left[\hat{e}_{K',n'}^{*\dagger}, e_{K,n}\right] = 0 \qquad \text{Eq(2.22)}$$

$$\left[\hat{\tilde{e}}_{K',n'}, e_{K,n}^{\dagger 3}\right] = \delta_{KK'}\delta_{nn'} - O\left(n_{exc}a_B\right)$$

Hence excitons can be considered as boson in the low density regime when $n_{exc} \ll a_B^{-3}$, or, when

the exciton inter-particle spacing is much large than its Bohr radius.

The electron and hole in an exciton form a dipole which interacts with electromagnetic fields of

light. The interband optical transition matrix element is given by the Fermi's golden rule:

$$W_{cv} = \frac{2\pi}{\hbar} \sum_{f,i} \left|\left\langle f\left|\hat{H}_I\right|i\right\rangle\right|^2 \delta\left(E_f - E_i - \hbar\omega\right) \qquad \text{Eq(2.23)}$$

where i and f denotes the initial and final states with energies E_i and E_f respectively.

$\hbar\omega$ is the photon energy, and $\hat{H}_I$ is the dipole interaction Hamiltonian. We first

consider an uncorrelated electron-hole pair, the matrix element is given by:

$$W_{cv} = \frac{2\pi}{\hbar} \sum_{f,i} \left|\left\langle f\left|\hat{H}_I\right|i\right\rangle\right|^2 \delta\left(E_f - E_i - \hbar\omega\right) \qquad \text{Eq(2.24)}$$

where σ is the polarization of light, j_e and j_h are the angular momenta of the electron and

hole, χ_{ck_e} and χ_{vk_h} are the envelope functions, and μ_{ck_e} and μ_{vk_h} are the Bloch functions. Since

χ_{ck_e,vk_h} vary little within a unit cell, while μ_{ck_e} and μ_{vk_h} are the same from cell to cell, we can

rewrite the integral $\int V$ as a summation over all cells of the integrations in each unit cell Ω_i:

$$M \approx \delta_{\sigma, j_e - j_h} \sum_{R_i} \int_{\Omega_i} dr' \left[\chi_{ck_e}^*\left(r' + R_i\right) \mu_{ck_e}^*\left(r' + R_i\right) \cdot E \mu_{vk_h}\left(r' + R_i\right) \chi_{vk_h}\left(r' + R_i\right) \right]$$

$$\simeq \delta_{\sigma, j_e - j_h} \frac{1}{\Omega} \sum_{R_i} \Omega \chi_{ck_e}^*\left(r' + R_i\right) \chi_{vk_h}\left(r' + R_i\right) \qquad \text{Eq(2.25)}$$

$$\cdot \left[\int_\Omega dr' \mu_{ck_e}^*\left(r'\right) er' \cdot E \mu_{ck_h}\left(r'\right) + eR_i \cdot E \int_\Omega dr' \mu_{ck_e}^*\left(r'\right) \mu_{ck_h}\left(r'\right) \right]$$

Notice that for the lowest energy interband transition μ_{ck_e} has s-wave symmetry while μ_{vk_h} has p-wave symmetry, we obtain:

Oscillator Strength of Excitons

A convenient material parameter that characterizes the exciton-photon coupling is the exciton oscillator strength f defined analogous to the atomic oscillator strength as:

$$f = \frac{2m^*\omega}{\hbar}\left|\langle\mu_v|r\cdot e|\mu_c\rangle\right|^2 \frac{V}{\pi a_B^3}$$

Eq(2.26)

The optical transition matrix element M can be expressed in terms of f as:

$$M = \sqrt{\frac{\pi e^2 f}{\varepsilon m^* V}}\,\Gamma$$

Eq(2.27)

Γ are the first three terms in eqn which depends on the selection rules and geometric properties of the semiconductor.
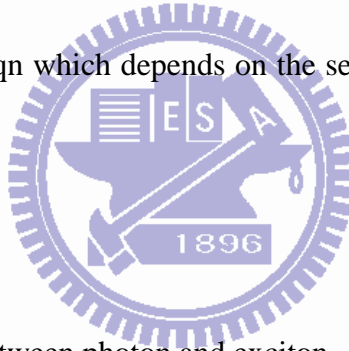
2.1.2 Introduction to coupling between photon and exciton

Typical microcavities have a thickness of a few integer multiples of half the photon wavelength at the exciton resonance frequency. Consequently, an exciton is coupled to a single cavity mode according to the in-plane wave-vector conservation.

Using the rotating wave approximation, the linear Hamiltonian of the system is written in the second quantization form as:

$$\begin{aligned}\hat{H}_{pol} &= H_{cav} + H_{exc} + H_I \\ &= \sum E_{cav}\left(k_\parallel, k_c\right)\hat{a}_{k_\parallel}^\dagger \hat{a}_{k_\parallel} + \sum E_{exc}\left(k_\parallel\right)e_{k_\parallel}e_{k_\parallel} + \sum \hbar\Omega\left(a_{k_\parallel,k_c}e_{k_\parallel} + a_{k_\parallel}e_{k_\parallel}\right)\end{aligned}$$

Eq(2.28)

Here $\hat{a}_{k_\parallel}^\dagger$ is the photon creation operator with in-plane wavenumber $k_\parallel$ and longitudinal

wavenumber $k_c = \mathbf{k} \cdot \hat{\mathbf{z}}$ determined by the cavity resonance. $\hat{e}_{k_\parallel}^\dagger$ is the exciton creation operators with in-plane wavenumber $k_\parallel$. $\hbar\Omega$ is the exciton-photon dipole interaction given by the exciton optical transition matrix element M, and we used the condition that M is non-zero only between modes with the same $k_\parallel$. The above Hamiltonian can be diagonalized by the transformation:

$$\hat{\hat{p}}_{k_\parallel} = X_{k_\parallel} e_{k_\parallel} + C_{k_\parallel} a_{k_\parallel}$$
$$\hat{\hat{q}}_{k_\parallel} = -C_{k_\parallel} e_{k_\parallel} + X_{k_\parallel} a_{k_\parallel}$$

Eq(2.29)

And $\hat{H}_{pol}$ becomes

$$\hat{H}_{pol} = \sum E_{LP}(k_\parallel) \hat{\hat{p}}_{k_\parallel}^\dagger \hat{\hat{p}}_{k_\parallel} + \sum E_{UP}(k_\parallel) q_{k_\parallel} q_{k_\parallel}$$

Eq(2.30)

The new operators $\left(\hat{\hat{p}}_{k_\parallel}, p_{k_\parallel}^\dagger \right)$ and $\left(\hat{\hat{q}}_{k_\parallel}, q_{k_\parallel}^\dagger \right)$ are the new quasi-particles, or, eigen modes, of the system. They are called the lower (LP) and upper polaritons (UP), corresponding to the lower and upper branches of the eigen energies. A polariton is a linear superposition of an exciton and a photon with the same inplane wavenumber $k_\parallel$. Since both excitons and photons are bosons, so are the polaritons. The exciton and photon fractions in each lower polariton (and vice versa for upper polaritons) are given by the amplitude squared of $X_{k_\parallel}$ and $C_{k_\parallel}$ which are referred to as the Hopfield coefficients [67], they satisfy:

$$\left| X_{k_\parallel} \right|^2 + \left| C_{k_\parallel} \right|^2 = 1$$

Eq(2.31)

Let $\Delta E(k_\parallel) = E_{exc}(k_\parallel) - E_{cav}(k_\parallel, k_c)$, $X_{k_\parallel}$ and $C_{k_\parallel}$ are given by:

$$\left|X_{k_{\parallel}}\right|^2 = \frac{1}{2}\left(1 + \frac{\Delta E\left(k_{\parallel}\right)}{\sqrt{\Delta\Delta E\left(k_{\parallel}\right)^2 + 4\hbar^2\Omega^2}}\right)$$

$$\left|C_{k_{\parallel}}\right|^2 = \frac{1}{2}\left(1 - \frac{\Delta E\left(k_{\parallel}\right)}{\sqrt{\Delta\Delta E\left(k_{\parallel}\right)^2 + 4\hbar^2\Omega^2}}\right)$$

Eq(2.32)

At $\Delta E = 0$, $\left|X_{k_{\parallel}}\right|^2 = \left|C_{k_{\parallel}}\right|^2 = \frac{1}{2}$, LP and UP are exactly half photon half exciton.

The energies of the polaritons, which are the eigenenergies of the Hamiltonian, are deduced from the diagonalization procedure as:

$$E_{LP,UP}\left(k_{\parallel}\right) = \frac{1}{2}\left[E_{exc} + E_{cav} \pm \sqrt{4\hbar^2\Omega^2 + \left(E_{exc} - E_{cav}\right)^2}\right]$$

Eq(2.33)

When the un-coupled exciton and photon are at resonance, $E_{exc} = E_{cav}$, lower and upper polariton energies have the minimum separation $E_{UP} - E_{LP} = 2\hbar\Omega$, which is often called the `Rabi splitting' in analogy to the atomic cavity Rabi splitting. Due to the coupling between the exciton and photon modes, the new polariton energies anti-cross when the cavity energy is tuned across the exciton energy. This is one of the signatures of 'strong coupling'. When $\left|E_{exc} - E_{cav}\right| \gg \hbar\Omega$, the polariton energies reduce to the same as photon and exciton energies due to the very large detuning between the two modes, and polariton is no longer a useful concept. So the detuning is assumed to be comparable to or less than the coupling strength in our discussions unless specified.

We use Δ as the exciton and photon energy detuning at $k_{\parallel} = 0$:

$$\Delta \doteq E_{cav}\left(k_{\parallel} = 0\right) - E_{exc}\left(k_{\parallel} = 0\right),$$

Eq(2.34)

And defind

$$k_{\|c} \doteq \sqrt{n_c k_c \frac{2\Omega}{c}}$$ Eq(2.35)

For which $E_{cav}(k_{\|c}) - E_{exc}(k_{\|c}) \sim \hbar\Omega$. Given Δ , eqngives the polariton energy-momentum dispersions. At $k_\| \ll k_{\|c}$, the dispersions are approximately parabolic:

$$E_{LP,UP}(k_\|) \simeq E_{LP,UP}(0) + \frac{\hbar^2 k_\|^2}{2m_{LP,UP}}$$ Eq(2.36)

The polariton effective mass is the weighted harmonic mean of the mass of its exciton

and photon components:

$$\frac{1}{m_{LP}} = \frac{|X|^2}{m_{exc}} + \frac{|C|^2}{m_{cav}}$$

$$\frac{1}{m_{UP}} = \frac{|C|^2}{m_{exc}} + \frac{|X|^2}{m_{cav}}$$
Eq(2.37)

where X and C are the exciton and photon fractions given by eqn. m_{exc} is effective exciton

mass of its center of mass motion, and m_{cav} is the effective cavity photon masses given by eqn. Since

m_{cav} is much smaller than m_{exc} ,

$$m_{LP}(k_\| \sim 0) \simeq m_{cav}/|C|^2 \sim 10^{-4} m_{exc}$$

$$m_{UP}(k_\| \sim 0) \simeq m_{cav}/|X|^2$$
Eq(2.38)

The very small effective mass of LPs at $k_\| \sim 0$ determines the very high critical temperature of

phase transitions for the system. At large $k_\| \gg k_{\|c}$, $E_{cav}(k_{k\|}) - E_{exc}(k_\|) \gg \hbar\Omega$, dispersions of the LP

and UP converge to the exciton and photon dispersions respectively, and LP has an effective mass

$m_{LP}(k_\| \gg k_{\|c}) \sim m_{exc}$. Hence the LP's effective mass changes by four order of magnitude from $k_\| \sim 0$

to large $k_\|$. This peculiar shape has important implications in the energy relaxation dynamics of

polaritons, as will be discussed in following chapter. A few examples of the polariton dispersion with

different Δ are given if fig 2.2. When taking into account the finite lifetime of the cavity photon and exciton, the eigen-energy equation is modified as:

$$E_{LP,UP}\left(k_{\parallel}\right)=\frac{1}{2}\left[E_{exc}+E_{cav}+i\left(\gamma_{cav}+\gamma_{exc}\right)\pm\sqrt{4\hbar^2\Omega^2+\left[E_{exc}-E_{cav}+i\left(\gamma_{cav}-\gamma_{exc}\right)\right]^2}\right]$$ Eq(2.39)

Here γ_{cav} is the out-coupling rate of a cavity photon due to imperfect mirrors, and γ_{exc} is the non-radiative decay rate of an exciton. Thus the coupling strength must be larger than half of the difference in decay rates to exhibit anti-crossing, i.e., to have polaritons as the new eigen modes. In another word, an excitation must be able to coherently transfer between a photon and an exciton at least once. When $\hbar\Omega\gg\left(\gamma_{cav}-\gamma_{exc}\right)/2$, we call the system in the strong coupling regime. In the opposite limit when excitons and photons instead are the eigenmodes, the system is called to be in the weak coupling regime, and the radiative decay rate of an exciton is given by the optical transition matrix element. We are mostly interested in microcavities with $\gamma_{exc}\ll\gamma_{cav}\ll\hbar\Omega$, then equation gives an accurate approximation of the polariton energies.

As a linear superposition of an exciton and a photon, the lifetime of the polaritons is directly determined by γ_{exc} and γ_{cav} as:

$$\begin{aligned}\gamma_{LP}&=\left|X\right|^2\gamma_{exc}+\left|C\right|^2\gamma_{cav}\\\gamma_{UP}&=\left|C\right|^2\gamma_{exc}+\left|X\right|^2\gamma_{cav}\end{aligned}$$ Eq(2.40)

In general, the polariton lifetime is mainly determined by the cavity photon lifetime: $\gamma_{LP}\simeq\left|C\right|^2\gamma_{cav}$. Polariton decays in the form of emitting a photon with the same $k_{\parallel}$ and total energy $\hbar\omega=E_{LP,UP}$, The one-to-one correspondence between the internal polariton mode and the external out-coupled photon mode lends great convenience to experimental access to the system. The

external emitted photon field carry direct information of the internal polaritons, such as the energy

dispersion, population per mode, and statistics of the polaritons. It is mainly through the emitted

photons that we study the internal polaritons.

2.1.3   Quasi-Particle Model simulation in MatLAB

The Hamiltonian for free exciton and cavity photon is:

$$H_0 = \sum_{\vec{k}} E_X\left(\vec{k}\right) b_{\vec{k}}^+ b_{\vec{k}} + \sum_{\vec{k}} E_C\left(\vec{k}\right) a_{\vec{k}}^+ a_{\vec{k}} \qquad \text{Eq(2.41)}$$

Operators $b_{\vec{k}}^+, b_{\vec{k}}, a_{\vec{k}}^+, a_{\vec{k}}$ are creation and annihilation operators for excitons and photons,

respectively.

The in-plane dispersion relation of exciton and cavity photon is

$$E_X\left(\vec{k}\right) = E_X\left(0\right) + \frac{\hbar^2 k^2}{2m_X} - \frac{i\hbar}{2}\Gamma_X\left(\vec{k}\right) \qquad \text{Eq(2.42)}$$

$$\begin{aligned} E_C\left(\vec{k}\right) &= \frac{\hbar c}{n_C}\sqrt{k_\perp^2 + k_\parallel^2} - \frac{i\hbar}{2}\Gamma_C\left(\vec{k}\right) \\ &\approx \frac{\hbar c}{n_C k_\perp}\left(1 + \frac{k_\parallel^2}{2k_\perp^2}\right), k_\parallel \ll k_\perp \qquad \text{Eq(2.43)} \\ &= E_C\left(0\right) + \frac{\hbar^2 k^2}{2m_C} - \frac{i\hbar}{2}\Gamma_C\left(\vec{k}\right) \end{aligned}$$

Where m_X, m_C is the effective mass of in-plane exciton or cavity photon, Γ_X is a

phenomenological decay rate the accounts for finite linewidth of the exciton resonance, and Γ_C is the

cavity photon escape rate taking into account the possibility of photon tunneling across the cavity

mirror.

The cavity photon acquires an effective mass of

$$m_C = \frac{2\pi\hbar}{\lambda_C c} = \frac{2\pi\hbar n_C}{\lambda_0 c}$$ Eq(2.44)

Where n_C is the cavity refractive index, and λ_0 is the resonant wavelength of the cavity.

The linear exciton-photon coupling formally reads:

$$H_0 = \sum_{\vec{k}} \hbar\Omega a_{\vec{k}}^+ b_{\vec{k}} + H.c.,$$ Eq(2.45)

where Ω is the coupling strength between an exciton and a photon, which is proportional to the

exciton oscillator strength and to the number of QWs embedded in the cavity.

If we only consider only one exciton and one photon interaction, the problem can be reduced to a

two-level system. As result, the eigenenergies of resulting states can be found by diagonalisation of the

matrix:

$$M(\vec{k}) = \begin{pmatrix} E_X(\vec{k}) & \hbar\Omega \\ \hbar\Omega & E_C(\vec{k}) \end{pmatrix}$$ Eq(2.46)

The eigencalues of this matrix are given by

$$(E_X - \lambda)(E_C - \lambda) = \hbar^2\Omega^2$$ Eq(2.47)

Solutions of the equation are

$$E_U(k) = \frac{E_C(k) + E_X(k)}{2} + \frac{1}{2}\sqrt{(E_C(k) - E_X(k))^2 + 4\hbar^2\Omega^2}$$ Eq(2.48)

$$E_L(k) = \frac{E_C(k) + E_X(k)}{2} - \frac{1}{2}\sqrt{(E_C(k) - E_X(k))^2 + 4\hbar^2\Omega^2}$$ Eq(2.49)

E_U and E_L are the energies of the upper and lower polariton branches, respectively.

From the solution of eigenvector, we can define the Hopfield coefficients $X_{U(L)}$ and $C_{U(L)}$ for

the upper (lower) polariton branch

$$M(k)\begin{pmatrix} X_U(k) \\ C_U(k) \end{pmatrix} = E_U(k)\begin{pmatrix} X_U(k) \\ C_U(k) \end{pmatrix}, M(k)\begin{pmatrix} X_L(k) \\ C_L(k) \end{pmatrix} = E_L(k)\begin{pmatrix} X_L(k) \\ C_L(k) \end{pmatrix} \qquad \text{Eq(2.50)}$$

$$C_U = \frac{2\hbar\Omega}{\sqrt{4\hbar^2\Omega^2 + (E_U - E_X)^2}} = X_L \qquad \text{Eq(2.51)}$$

$$X_U = \frac{E_U - E_X}{\sqrt{4\hbar^2\Omega^2 + (E_U - E_X)^2}} = -C_L \qquad \text{Eq(2.52)}$$

$|X|^2, |C|^2$ describe weights of excitonic and photonic parts in each branch. As result, the sum of $|X|^2$ and $|C|^2$ equal one.

However, we have to deal with more complicated system in practice. Generally, for III-V nitride and II-VI zincoxide semiconductors with a wurtize structure belonging to the space group C_{6v}^4, the conduction band minimum is located at the center of the Brillouin zone and its vicinity is almost composed by the s states of nitrogen and cation atoms. The valence band maximum is also located at the center of the Brillouin zone and its vicinity is almost composed by p states of nitrogen. Due to the reduces symmetry and to the spin-obit interaction, the valence band splits into the well-known A, B, and C bands with Γ_9, Γ_7, and Γ_7 symmetries, respectively. Therefore, the excitons have A, B, and C excitonic states in GaN and ZnO based material systems. Moreover, exciton is a Hydrogen-like atom, and the principal quantum number indicates the difference energy level. Fortunately, we don't have to find the solution including total energy level of exciton, because the oscillator strength is inversely proportional to n^3, with n being the principal quantum number. Besides, the C exciton has zero oscillator strength at normal incidence. In conclusion, we consider A and B excitons which only included the 1s and 2s states in the following simulation, [67, 68] .

According to Eq(2.46) form, the quasi-particle model's matrix

$$M\left(\vec{k}\right) = \begin{pmatrix} E_{X_{A1s}} & 0 & 0 & 0 & \hbar\Omega_{A1} \\ 0 & E_{X_{A2s}} & 0 & 0 & \hbar\Omega_{A2} \\ 0 & 0 & E_{X_{B1s}} & 0 & \hbar\Omega_{B1} \\ 0 & 0 & 0 & E_{X_{B2s}} & \hbar\Omega_{B2} \\ \hbar\Omega_{A1} & \hbar\Omega_{A2} & \hbar\Omega_{B1} & \hbar\Omega_{B2} & E_C \end{pmatrix} \qquad \text{Eq(2.53)}$$

2.2 Transfer Matrix Method

The transfer-matrix method is a method used in optics and acoustics to analyze the propagation of electromagnetic or acoustic waves through a stratified (layered) medium. This is for example relevant for the design of anti-reflective coatings and dielectric mirrors. Fig 2.3 show the simulation result of the reflectivity of microcavity in transfer matrix method.

The reflection of light from a single interface between two media is described by the Fresnel equations. However, when there are multiple interfaces, such as in the fig 2.4, the reflections themselves are also partially reflected. Depending on the exact path length, these reflections can interfere destructively or constructively. The overall reflection of a layer structure is the sum of an infinite number of reflections, which is cumbersome to calculate.

The transfer-matrix method is based on the fact that, according to Maxwell's equations, there are simple continuity conditions for the electric field across boundaries from one medium to the next. If the field is known at the beginning of a layer, the field at the end of the layer can be derived from a simple matrix operation. A stack of layers can then be represented as a system matrix, which is the

product of the individual layer matrices. The final step of the method involves converting the system matrix back into reflection and transmission coefficients.

Below is described how the transfer matrix is applied to electromagnetic waves of a given frequency propagating through a stack of layers at normal incidence. It can be generalized to deal with incidence at an angle, absorbing media, and media with magnetic properties. We assume that the stack layers are normal to the z-axis and that the field within one layer can be represented as the superposition of a left- and right-traveling wave with wave number k,

$$E(z) = E_r e^{ikz} + E_t e^{-ikz} \qquad \text{Eq(2.54)}$$

Because it follows from Maxwell's equation that E and E' must be continuous across a boundary, it is convenient to represent the field as the vector (E, E'), where

$$E' = \frac{dE}{dz} = ikE_r e^{ikz} - ikE_t e^{-ikz} \qquad \text{Eq(2.55)}$$

Since there are two equations relating E and E' to E_r and E_t, these two representations are equivalent. In the new representation, propagation over a distance L into the positive z-direction is described by the matrix

$$M = \begin{pmatrix} \cos kL & \dfrac{1}{k}\sin kL \\ -k\sin kL & \cos kL \end{pmatrix} \qquad \text{Eq(2.56)}$$

and

$$\begin{pmatrix} E(z+L) \\ E'(z+L) \end{pmatrix} = M \begin{pmatrix} E(z) \\ E'(z) \end{pmatrix} \qquad \text{Eq(2.57)}$$

Such a matrix can represent propagation through a layer if k is the wave number in the medium and L the thickness of the layer: For a system with N layers, each layer j has a transfer matrix M_j, where j increases towards higher z-values. The system transfer matrix is then

$$M_s = M_N \cdot \ldots \cdot M_2 \cdot M_1$$ Eq(2.58)

Typically, one would like to know the reflectance and transmittance of the layer structure. If the layer stack starts at $z = 0$, then for negative z, the field is described as

$$E_L(z) = E_0 e^{ik_L z} + r E_0 e^{-ik_L z}$$ Eq(2.59)

where E_0 is the amplitude of the incoming wave, k_L the wave number in the left medium, and r is the amplitude reflectance coefficient of the layer structure. On the other side of the layer structure, the field consists of a right-propagating transmitted field

$$E_R(z) = t E_0 e^{ik_R z},$$ Eq(2.60)

where t is the amplitude transmittance and k_R is the wave number in the rightmost medium. If $E'_L = dE_L / dz$ and $E'_R = dE_R / dz$, then we can solve

$$\begin{pmatrix} E(z_R) \\ E'(z_R) \end{pmatrix} = M \cdot \begin{pmatrix} E(0) \\ E'(0) \end{pmatrix}$$ Eq(2.61)

in terms of the matrix elements M_{mn} of the system matrix M_s and obtain

$$t = 2ik_L e^{-ik_R L} \left[\frac{M_{11} M_{22} - M_{12} M_{21}}{-M_{21} + k_L k_R M_{12} + i(k_R M_{11} + k_L M_{22})} \right]$$ Eq(2.62)

And

$$r = \left[\frac{(M_{21} + k_L k_R M_{12}) + i(-k_R M_{11} + k_L M_{22})}{(-M_{21} + k_L k_R M_{12}) + i(k_R M_{11} + k_L M_{22})} \right]$$ Eq(2.63)

The transmittance and reflectance (i.e., the fractions of the incident intensity E_0 transmitted and reflected by the layer) are often of more practical use and are given by $T = |t^2|$ and $R = |r^2|$, respectively.

As shown in Fig2.4, where θ is the angle of incidence/reflection of the incident radiation and λ is the wavelength of the radiation. The measured reflectivity depends on the variation in the scattering length density (SLD) profile, $(\rho(z))$ perpendicular to the interface. Although the scattering length density profile is normally a continuously varying function, the interfacial structure can often be well approximated by a slab model in which layers of thickness d_n, scattering length density ρ_n and roughness $\sigma_{n,n+1}$ are sandwiched between the super- and sub-phases. One then uses a refinement procedure to minimise the differences between the theoretical and measured reflectivity curves, by changing the parameters that describe each layer.

In this description the interface is split into n layers. Since the incident neutron beam is refracted by each of the layers the wavevector, k, in layer n, is given by:

$$k_n = \sqrt{k_z^2 - 4\pi(\rho_n - \rho_0)}$$ Eq(2.64)

The Fresnel reflection coefficient between layer n and $n+1$ is then given by:

$$r_{n,n+1} = \frac{k_n - k_{n+1}}{k_n + k_{n+1}}$$ Eq(2.65)

Since the interface between each layer is unlikely to be perfectly smooth the roughness/diffuseness of each interface modifies the Fresnel coefficient and is accounted for by an error function, as described by Nevot and Croce (1980).

$$r_{n,n+1} = \frac{k_n - k_{n+1}}{k_n + k_{n+1}} \exp\left(-2k_n k_{n+1} \sigma_{n,n+1}^2\right)$$

Eq(2.66)

A phase factor, β is introduced, which accounts for the thickness of each layer.

$$\beta_0 = 0 \text{, and } \beta_n = ik_n d_n$$

Eq(2.67)

where $i^2 = -1$. A characteristic matrix, c_n is then calculated for each layer.

$$c_n = \begin{bmatrix} \exp(\beta_n) & r_{n,n+1}\exp(\beta_n) \\ r_{n,n+1}\exp(-\beta_n) & \exp(-\beta_n) \end{bmatrix}$$

Eq(2.68)

The resultant matrix is defined as the product of these characteristic matrices

$$M = \prod_0^n c_n$$

Eq(2.69)

from which the reflectivity is calculated

$$R = \left|\frac{M_{10}}{M_{00}}\right|^2$$

Eq(2.70)
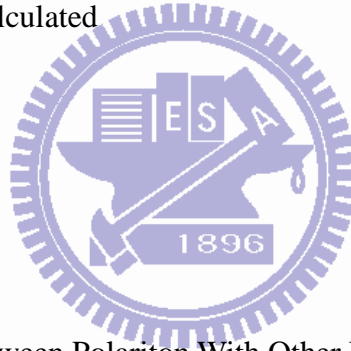
2.3 The Scattering Mechanisms Between Polariton With Other Particle

We identify three steps in the description of photoluminescence from semiconductors: an excitation provided by an external pump, a relaxation process in which the energy of the excitation is redistributed among the electronic states and released to the lattice, and a radiative recombination process. The relaxation mechanisms of recent research developments include phonon-polariton scattering, electron-polariton scattering, polariton-polariton scattering, and exciton dissociation. In Fig 2.4 we give a schematic picture of the polariton dispersion and of the possible scattering processes governing its dynamics and PL that we are going to consider.

2.3.3   Polariton dynametic rate equation

In order to describe the relaxation kinetics of classical particles, we use the semi-classical Boltzmann equation to calculate the polariton distribution, as equation 2.71.

$$\frac{\partial}{\partial t}n_{\vec{k}} = P_{\vec{k}}(t) - \Gamma_{\vec{k}}n_{\vec{k}} + W_{\vec{k}'\rightarrow\vec{k}}n_{\vec{k}'} - W_{\vec{k}\rightarrow\vec{k}'}n_{\vec{k}} \qquad \text{Eq(2.71)}$$

where $P_{\vec{k}}$ is the generation term, due to optical pumping or to any other physical process, $\Gamma_{\vec{k}}$ is the particle decay rate, and $W_{\vec{k}'\rightarrow\vec{k}}$ is the total scattering rate between the states and due to any kind of physical process. Uhlenbeck and Gropper (1932) first proposed to include the quantum character of the particles by taking into account their fermionic or bosonic nature. Equation 2.71 written for bosons reads:

$$\frac{\partial}{\partial t}n_{\vec{k}} = P_{\vec{k}}(t) - \Gamma_{\vec{k}}n_{\vec{k}} + W_{\vec{k}'\rightarrow\vec{k}}\left(1+n_{\vec{k}}\right)n_{\vec{k}'} - W_{\vec{k}\rightarrow\vec{k}'}\left(1+n_{\vec{k}'}\right)n_{\vec{k}}$$
$$= P_{\vec{k}}(t) - \frac{n_{\vec{k}}}{\tau_{\vec{k}}} + \left.\frac{\partial}{\partial t}n_{\vec{k}}\right|_{LP-LP} + \left.\frac{\partial}{\partial t}n_{\vec{k}}\right|_{LP-ph}$$

$$\text{Eq(2.72)}$$

As elementary excitations of the microcavity system, polaritons are most conveniently created by a laser pump pulse, after which they relax and under appropriate conditions accumulate at least partly in the ground state of the LP branch, before they completely decay. In order to study a spontaneous phase transition, pumping should be incoherent, so that there are no phase relations between the pump light and the condensate. One speaks about a quantum statistically degenerate state if the number of polaritons n_0 in the ground state is much larger than 1. In this case, stimulated relaxation processes dominate over the spontaneous ones by a factor $1+n_0$. The main interactions which drive the relaxation and eventually the condensation stem from the exciton-phonon interactions and the

Coulomb interactions between excitons. The exchange Coulomb interactions dominate over the direct

Coulomb interactions between two excitons and give rise to a repulsive interaction between two

polaritons with an identical spin. This interaction provides the fastest scattering mechanism which

thermalizes the polariton gas, but the temperature of the gas can only be lowered by coupling to the

cold acoustic phonon reservoir. Much of the physics of the polariton relaxation and condensation can

be described with the semiclassical Boltzmann rate eqn, which we formulate in the next section. We

include the scattering due to the LP-phonon and LP-LP interactions as discussed. The spectral change

due to condensation is not extended enough to have a substantial influence on the condensation

kinetics. Hence we use only the free-particle spectrum to calculate the scattering rates. These rate

equations yield results in good agreement with the experimental observations in many reference. The

rate equations calculate only the number of the LPs in the ground and excited states.
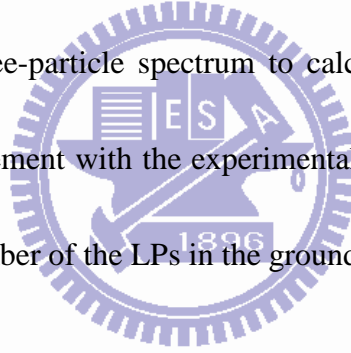
2.3.4   The scattering mechanisms between polariton with other particle

2.3.4.1   The polariton-phonon scattering

The relevant interaction between excitons and longitudinal-acoustic phonons is provided by the

deformation-potential coupling with the electron and hole De and Dh, respectively. This interaction

Hamiltonian between the LPs and phonons is [69, 70]

$$H_w^{LP-ph} = \sum_{\vec{k},\vec{q},q_z} X_k^* X_{|\vec{k}+\vec{q}|} \langle k | H_w^{x-ph} | k+q \rangle \times \left(c_{\vec{q},q_z} - c_{-\vec{q},-q_z}^{\dagger\dagger} \right) b_{\vec{k}+\vec{q}} b_{\vec{k}} \qquad \text{Eq(2.73)}$$

where X_k^* are again the exciton Hopfield coefficients of the polariton. The phonons are taken to

be the bulk phonons with a wave vector $q\vec{e}_\parallel + q_z \vec{e}_z$. Only the in-plane vector component is conserved.

The quantum well 1s-exciton envelope function is given by

$$\chi\left(\vec{r}_\parallel, z_e, z_h\right) = \sqrt{\frac{2}{\pi a_B^2}} e^{-r_\parallel/a_B} f_e\left(z_e\right) f_h\left(z_h\right) \qquad \text{Eq(2.75)}$$

where a_B is the 2D Bohr radius and $f_{e,h}\left(z_{e,h}\right)$ are the quantum well envelope functions.

Evaluating the exciton-phonon interaction matrix element with this envelope function, one finds

$$G(\vec{q}, q_z) = i\sqrt{\frac{\hbar\left(q^2 + q_z^2\right)^{1/2}}{2\rho V u}}\left[D_e I_e^\parallel(q) I_e^z(q_z) - D_h I_h^\parallel(q) I_h^z(q_z)\right] \qquad \text{Eq(2.76)}$$

Here ρ is the density, u is the sound velocity, and V is the microcavity volume. The superposition integrals for the electron (e) or hole (h) are given by

$$I_{e,h}^\parallel(q) = \left[1 + \left(\frac{m_{h,e}}{2M} q a_B\right)^2\right]^{-3/2}$$

$$I_{e,h}^z(q_z) = \int_0^{L_{QW}} dz f_{e,h}^2(z) e^{iq_z z} \qquad \text{Eq(2.77)}$$

These integrals cut off the sums for $q > a_B^{-1}$ and for $q_z > 2\pi/L_{QW}$.

With this interaction matrix element, the transition rates for the LPs can be written as

$$W_{\vec{k} \rightarrow \vec{k}' = \vec{k} - \vec{q}}^{LP-ph} = \frac{2\pi}{\hbar} \sum_{q_z} X_k^2 X_{k-q}^2 G\left(q, q_z\right)$$

$$\times \delta\left(E_{k-q} - E_k \pm \hbar\omega_{q,q_z}\right) \qquad \text{Eq(2.78)}$$

$$\times \left(N_B\left(\hbar\omega_{q,q_z}\right) + \frac{1}{2} \pm \frac{1}{2}\right)$$

where $N_B\left(\hbar\omega_q\right) = 1/\left[\exp\left(\hbar\omega_q\right) - 1\right]$ is the thermal phonon Bose distribution function. Here the small correction of the phonon confinement is neglected.

2.3.4.2   The polariton-polariton scattering

For a nonpolarized LP gas, following Tassone and Yamamoto [71], we further simplify the scattering coefficient as

$$M \simeq 2\sum_{k,k'} V_{\bar{k}-\bar{k}'} \varphi_k \varphi_{k'} \left(\varphi_k^2 - \varphi_k \varphi_{k'} \right) \simeq 6E_0 \frac{a_B^2}{S} \qquad \text{Eq(2.79)}$$

where φ_k and E_0 are the screened 2D 1s-exciton wave function and binding energy, respectively. $V_k = 2\pi/\varepsilon_0 Sk$ is the 2D Coulomb potential and ε_0 is the dielectric function.

The corresponding LP transition probability is then

$$W_{k,k';k_1,k_2}^{LP-LP} = \frac{\pi}{\hbar} \frac{S^2}{(2\pi)^4}$$

$$\times \frac{\Delta E^2 |M|^2 X_k^2 X_{k'}^2 X_{k_1}^2 X_{k_2}^2}{\left[\partial E(k')/\partial k'^2 \right] \left[\partial E(k_1)/\partial k_1^2 \right] \left[\partial E(k_2)/\partial k_2^2 \right]} \qquad \text{Eq(2.80)}$$

$$\times R(k,k',k_1,k_2)$$

A uniform energy grid is adopted with an energy spacing ΔE. The terms proportional to the 2D density of states $\partial E(k')/\partial k'^2$ stem from the conversion of integration over momenta to summation over energies. The term R is given by

$$R(k,k',k_1,k_2) = \int \frac{dq^2}{\left[(k+k_1)^2 - q^2 \right]\left[q^2 - (k-k_1)^2 \right]\left[(k'+k_2)^2 - q^2 \right]\left[q^2 - (k'-k_2)^2 \right]} \qquad \text{Eq(2.81)}$$

The integration is taken over the range in which all four terms under the square root are non-negative. Energy conservation is built in by taking $k_2 = k\left(E_2 = E_k + E_{k'} - E_{k_1} \right)$ and summing over the $E_{k'}$ and E_{k_1}.

(a)Wannier exciton (typical of inorganic semiconductors)

(b)Frenkel exciton (typical of organic materials)
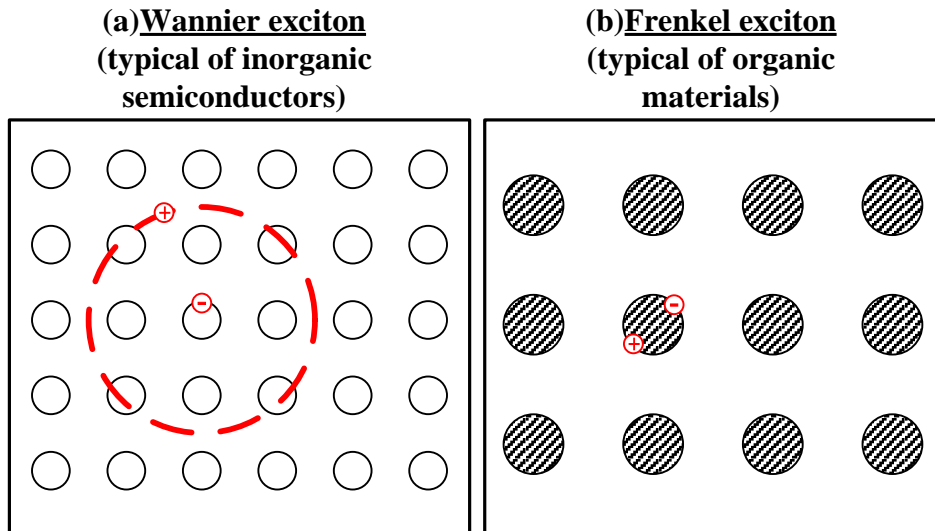
Fig 2.1 Excitons may be treated in two limiting cases, depending on the properties of the binding

energy E_b. (a) Wannier-Mott exciton $E_b < 0.1eV$ (b)Frenkel exciton $1eV > E_b > 0.1eV$
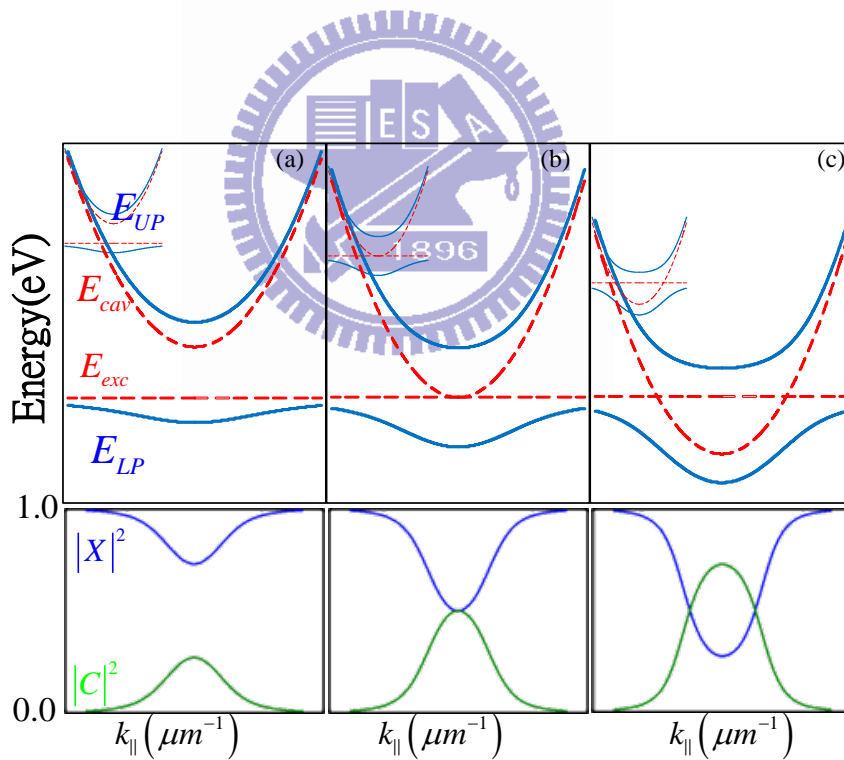
Fig. 2.2 polariton dispersion and corresponding Hopfield coefficients at (a) positive detuning (b)

zero detuning (c) negative detuning
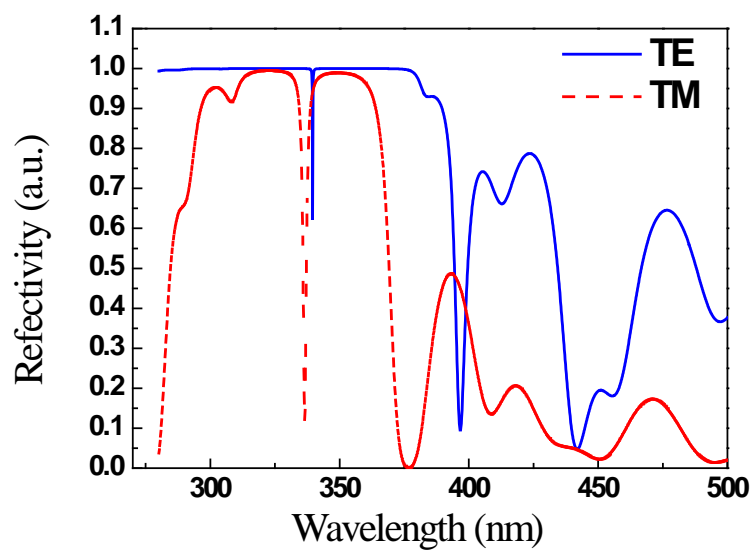
Fig 2.3the simulation result of the reflectivity of microcavity in transfer matrix method

$$Q_z = \frac{4\pi}{\lambda}\sin\theta = 2k_z$$

Layer 0
1
...
...
N
N+1

| d
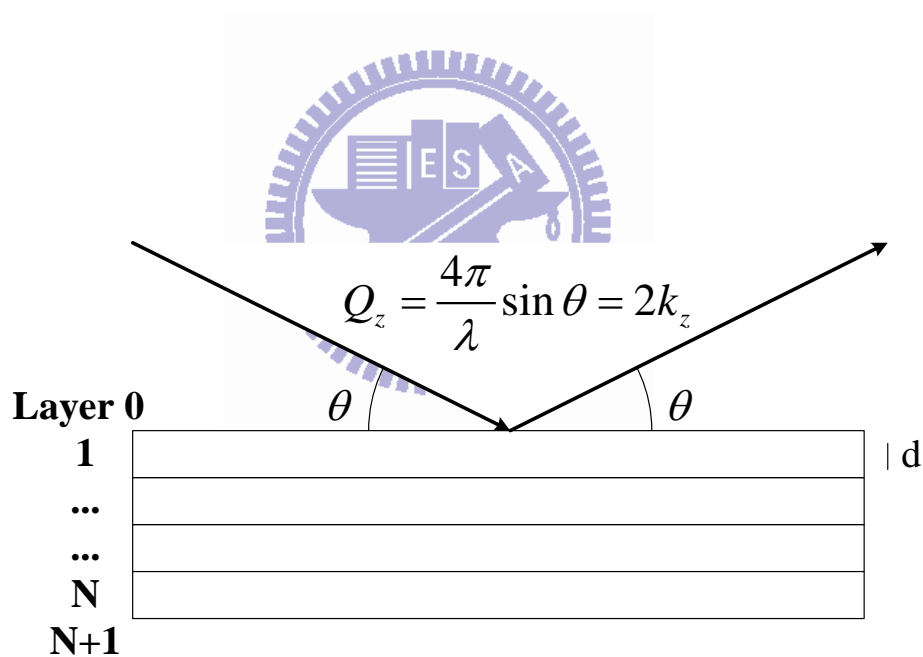
Fig 2.4 Schematic of the structure for transfer matrix model
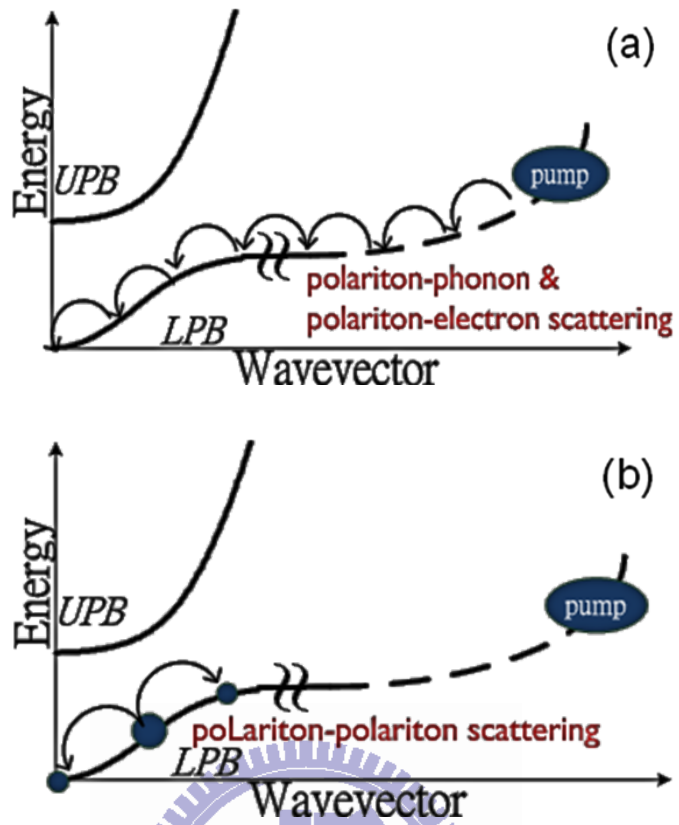
Fig 2.5 schematic of the polariton scattering processes (a) polariton-phonon scattering and

polariton-electron scattering (b) polariton-polariton scattering

Chapter3. Experimental Systems

3.1 Sample Materials And Structures

An optical microcavity is a structure formed by reflecting faces on the two sides of a spacer layer or optical medium. A typical structure of a semiconductor microcavity consists of a $m\lambda_C/2$ cavity layer sandwiched between two distributed Bragg reflectors (DBRs). A DBR is made of layers of alternating high and low refraction indices, each layer with an optical thickness of $\lambda/4$. Light reflected from each interface destructively interfere, creating a stop-band for transmission. Hence the DBR acts as a high-reflectance mirror when the wavelength of the incident light is within the stop-band.

In current semiconductor samples, the microcavity structure consists of a bulk ZnO $3/2\lambda$ thick cavity sandwiched between a bottom 30-pair AlN/AlGaN DBR and a top 9-period dielectric SiO_2/HfO_2 DBR. Here we chose λ to be 380 nm in air. The aluminum composition in the DBR was about 23% from the measurement of high-resolution x-ray diffraction. The AlN/AlGaN DBR was grown on (0001)-oriented sapphire substrates in a low-pressure high-speed rotating-disk metalorganic chemical vapor deposition (MOCVD) system. During the growth, trimethylgallium (TMGa) and trimethylaluminum (TMAl) were used as group III source materials and ammonia (NH3) as the group V source material. After thermal cleaning of the substrate in hydrogen ambient for 5 min at 1100 °C, a 30-nm-thick GaN nucleation layer was grown at 500 °C. The growth temperature was raised up to 1020 °C for the growth of 2.8 μm GaN buffer layer. Then, the $AlN/Al_{0.23}Ga_{0.77}N$ DBRs were grown under the fixed chamber pressure of 100 Torr [72].

The bulk ZnO 3/2λ thick cavity was grown on AlN/Al$_{0.23}$Ga$_{0.77}$N DBR by plasma-assisted molecular beam epitaxy (MBE) system under the growth temperature of about 550 °C.

The 9-period SiO$_2$/HfO$_2$ dielectric DBR was deposited by dual electron-beam gun evaporation system to complete the microcavity structure. The schematic sketch of the ZnO-based microcavity structure is shown in Fig 3.1. The interface between the AlN/AlGaN DBR and the ZnO cavity is smooth as seen from the cross-sectional scanning electron microscope (SEM) image in Fig 3.2. To further illustrate the configuration of the hybrid microcavity structure, the refractive index profile and the electric-field intensity in the growth direction for normal incidence at photon energy of 3.23 eV are displayed in Fig 3.3. The reflectivity spectra of a 30-pair AlN/Al0.23Ga0.77N DBR and a nine-pair SiO2 /HfO2 DBR were measured at RT, respectively, for normal incidence, as shown in Fig3.4. The peak reflectivity of bottom AlN/AlGaN DBR is about 93% and the stop band width is about 145 meV. As for the top SiO2 /HfO2 DBR, the peak reflectivity and the stop bandwidth are 97% and 790 meV, respectively.

3.2 Photoluminescence Measurement

Photoluminescence is a general and powerful analysis technology. It is a process in which a chemical compound absorbs a photon of light, thus transitioning to a higher electronic energy state, and then radiates a photon back out, returning to a lower energy state. The period between absorption and emission is typically extremely short, on the order of 10 nanoseconds. Under special

circumstances, however, this period can be extended into minutes or hours. The simplest

photoluminescent processes are resonant radiations, in which a photon of a particular wavelength is

absorbed and an equivalent photon is immediately emitted. Fig 3.5 shows the PL experiments setup

discussed in the dissertation.

Generally, we use a biconvex lens to focus laser beam onto a spot ~50 μm in diameter on the

sample surface. The light emission from the sample was collected by optics fiber into a spectrograph,

iHR 320 system, with a spectral resolution of 0.1nm and was recorded by using cooling charged

coupled devices (CCDs) and photomultipliers (PMTs).

3.2.1 Micro-Photoluminescence Measurement

Micro-PL measurements with a confocal spectroscopy setup is similar to ARPL, as shown in Fig

3.6. About 30mW of the 325 nm excitation Helium-Cadmium laser beam was focused onto the sample

using a high magnification microscope objective. The spot size on the sample is estimated to be 6μm

in diameter, measured by knife-edge method. The PL signal was collected and collimated by the same

objective, and then focused onto the input slit of iHR spectrometer. A cooling charge-coupled-device

(CCD) detector array was used to collect the spectra. The resolution of the system is estimated to be

approximately 0.1nm.

We have been use several laser light source to proceed those experiments, include 325nm He-Cd

laser , 355nm Nd:YVO$_4$ laser, 266nm Ti-sapphire laser, and 266nm Nd:YAG laser.

3.2.2   Angle-Resolved Photoluminescence Measurement

Fig3.7 shows the experimental setups for measuring angle-resolved photoluminescence (ARPL) of a microcavity sample at room temperature. In principle, the ARPL measurement setup is similar to PL setup. The emission light is collected by a fiber-coupled lens which is mounted on a goniometer rail with an angular resolution of $4° \sim 6°$ which is in turn connected to a spectrometer. The excitation source of the ARPL measurements is a 266 nm radiation from a frequency tripled Ti:sapphire laser at an oblique incidence angle of 57º. The general near UV objective lens doesn't have enough long work distance to avoid blocking the optic path of the emission light. Therefore, we use a biconvex lens to focus the input beam, and the input beam onto a spot ~50μm in diameter on the sample surface.

3.3 Reflection Measurement

The angle-resolved reflectance measurement setup is similar to ARPL. We use Xenon lamp as the input light whose spectrum is shown in Fig 3.8. The white light source input along one rail of a goniometer, and a doublet lens focuses the input beam from a slant angle to a spot ~100 μm in diameter on the sample. The reflected beam is collected by a fiber-coupled lens with an angular resolution of 4º-6º on the other rail of the goniometer which is in turn connected to a spectrometer.

9-pair SiO$_2$/HfO$_2$

3/2 λ ZnO

30-pair AlN/
Al$_{0.2}$Ga$_{0.8}$N DBR

2.8-μm GaN

c-sapphire

e-gun

MBE

MOCVD

Fig3.1 The schematic sketch of the ZnO-based microcavity structure

Top DBR

Bottom DBR

GaN
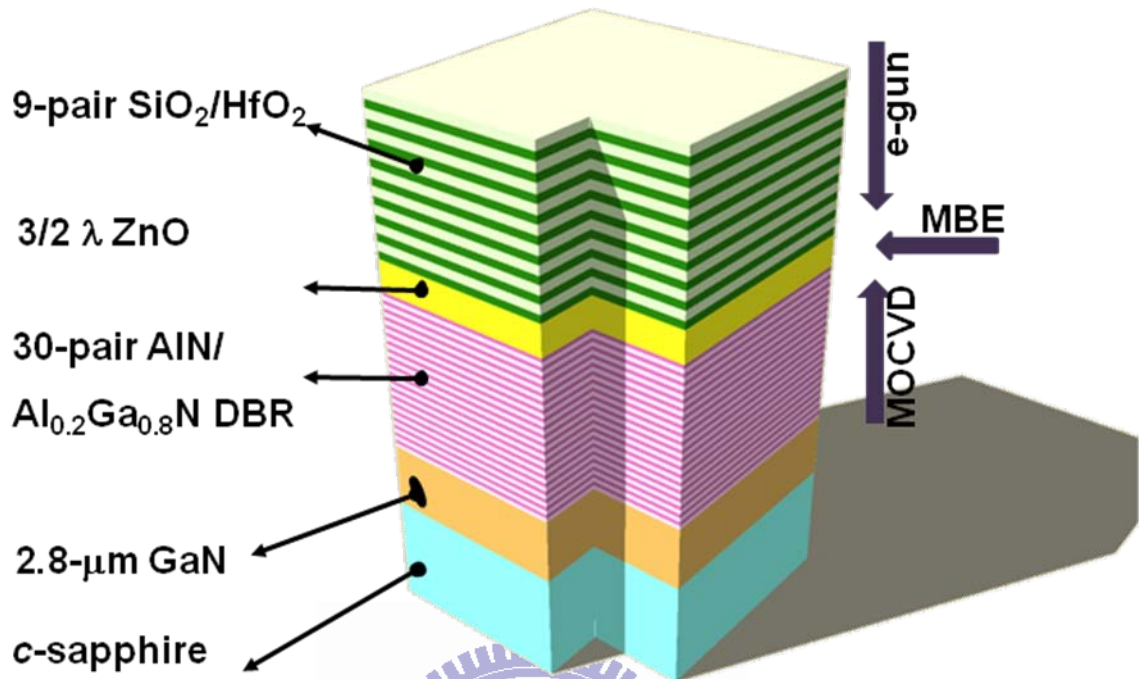
c-sapphire
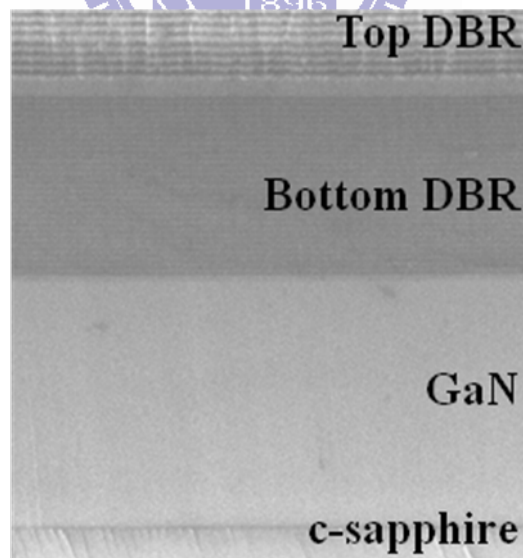
Fig 3.2 The interface between the AlN/AlGaN DBR and the ZnO cavity is smooth as seen from

the cross-sectional scanning electron microscope (SEM) image
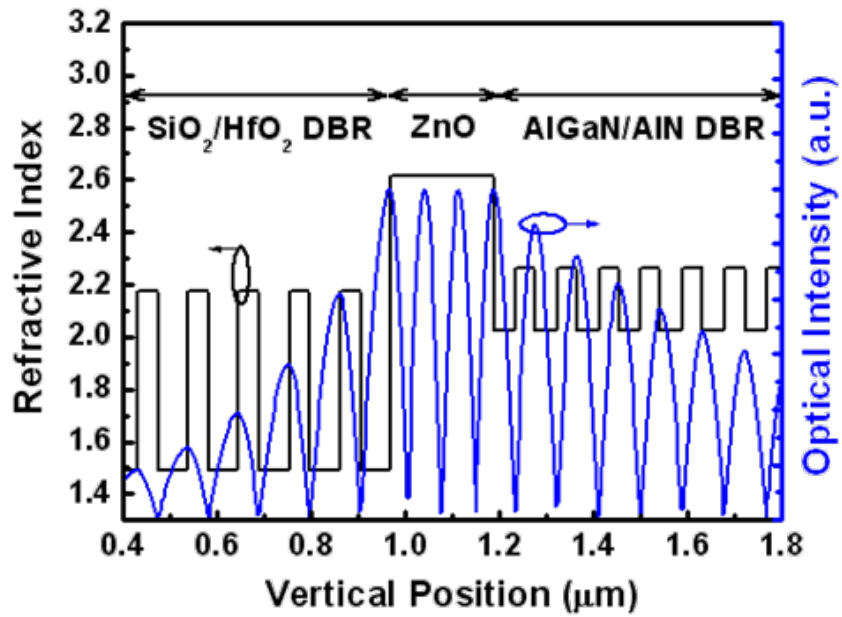
Fig 3.3 Refractive index profile and electric-field intensity in the growth direction for normal

incidence at photon energy of 3.23 eV.
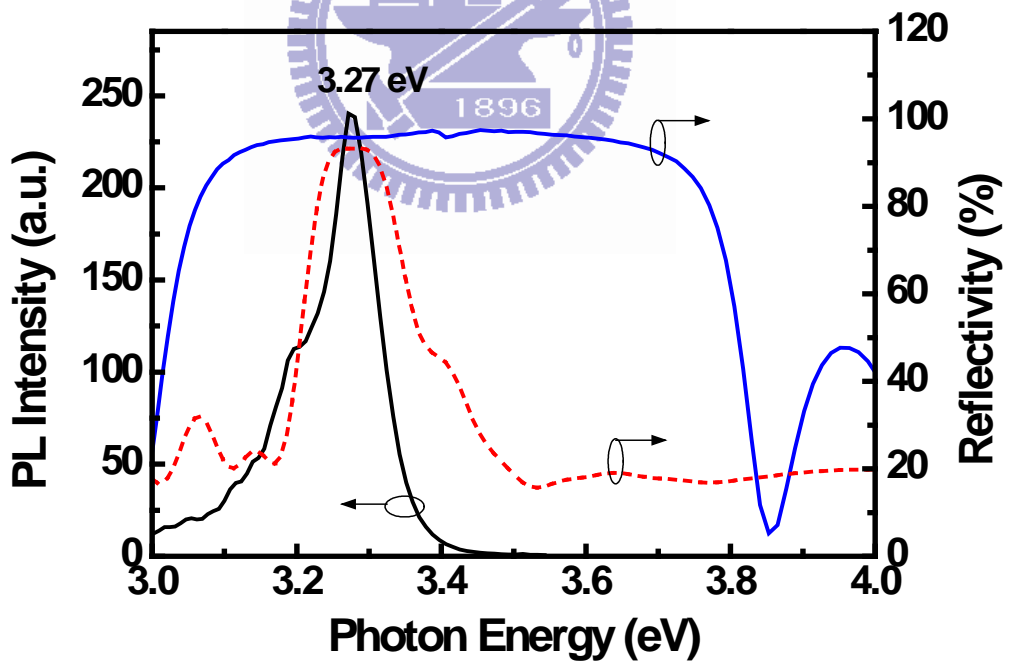
Fig 3.4The RT reflectivity spectra of a 30-pair AlN/Al$_{0.23}$Ga$_{0.77}$N DBR ☐(dashed line) and a

nine-pair SiO2 /HfO2 DBR☐(solid line). RT PL spectrum from a half cavity is located within the stop

band of the bottom and top DBRs.
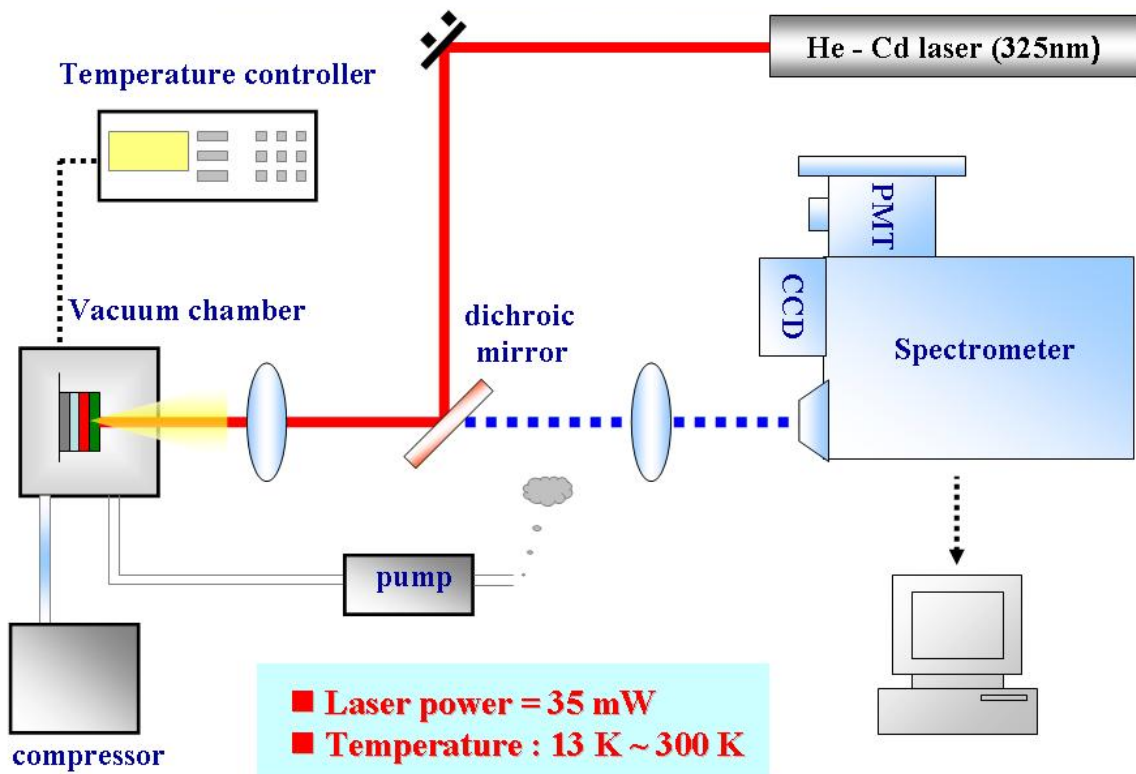
Fig3.5 The schematic diagram of photoluminescence setup
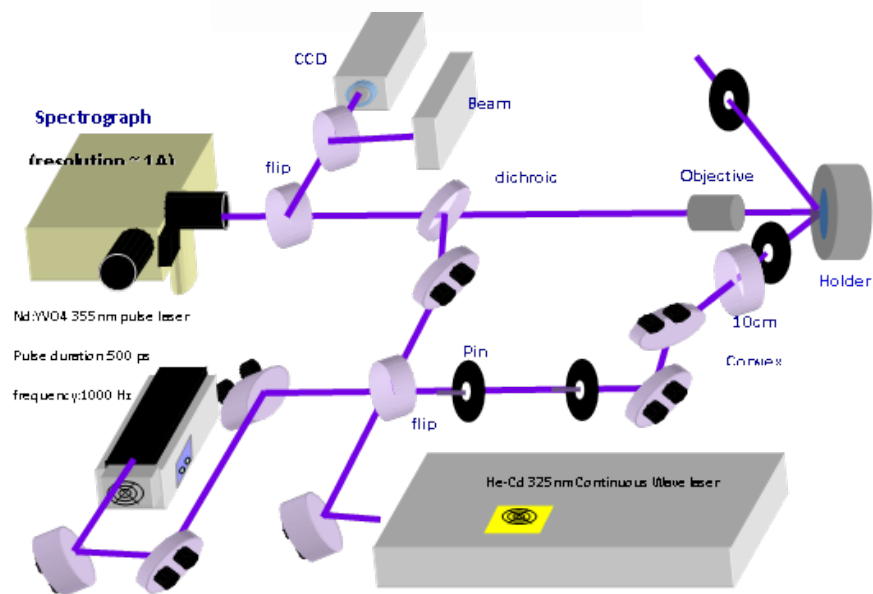
Fig3.6 The schematic diagram of micro-photoluminescence setup
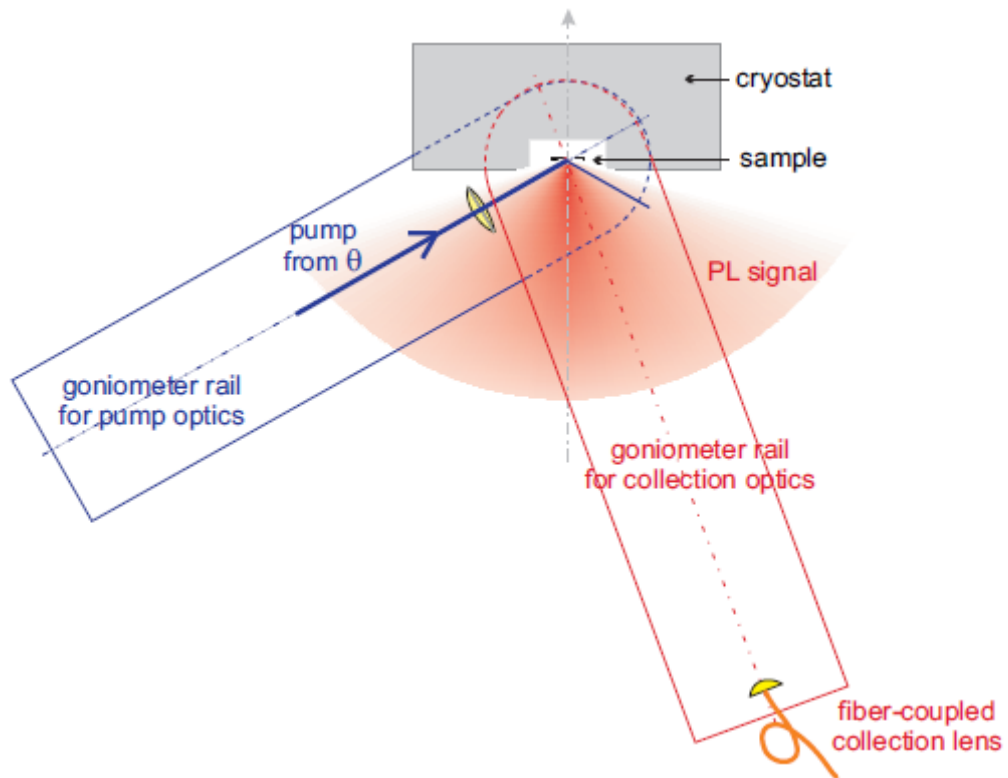
Fig3.7 The schematic diagram of angle-resolved photoluminescence setup
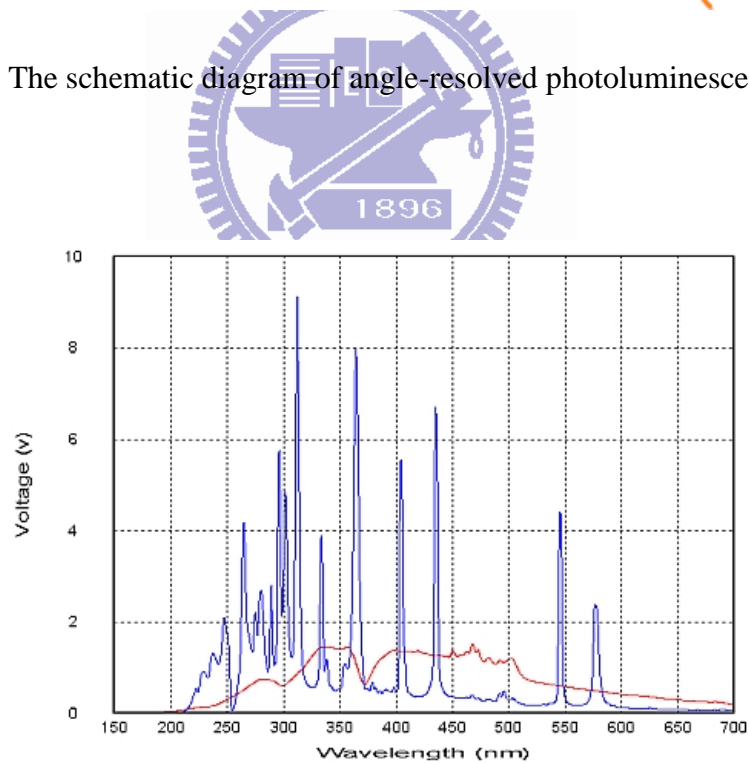
Fig3.8 The spectrum of Xenon lamp

Chapter4.   EXPERIMENTAL SYSTEMS

4.1   Polariton dispersion

In practice, we have three ways to prove the polariton exist in the microcavity system. First, the energy splitting between E_{LP} and E_{UP} is observable in reflectivity or photoluminescence spectrum. Due to the coupling between the exciton and photon modes, the new polariton energies anticross when the cavity energy is tuned across the exciton energy. In chapter 2 , we studied the E-k dispersion of microcavity, as shown in Fig 2.2. The dispersion curves of reflectivity, transmission, or absorption resonances in an open cavity as a function of the angle of incidence θ, with $k_{\parallel} = q \sin \theta$. As result, we can measurement the polariton dispersion curve by angle-resolved photoluminescence or angle-resolved reflectility experiment. Moreover, according to the simulation result of transfer matrix method or quasi-particle model, we can obtain not only the Rabi-splitting energy but also the more physical parameters such as the oscillator strength. Second, Rabi oscillations are the temporal equivalent of the energy splitting and appear only if the lower and upper modes are well defined. In Fig 1.7, the probability for finding polariton in either the upper or lower level is oscillator with each other with the form

$$\left| c_1 \left(t \right) \right|^2 = \cos^2 \left(\Omega_R t / 2 \right)$$
$$\left| c_2 \left(t \right) \right|^2 = \sin^2 \left(\Omega_R t / 2 \right)$$

Eq(4.1)

As result, The Hanbury Brown and Twiss(HBT) is the well-known experiment setup to measure the temporal coherence between two light sources. However, the HBT is not discussed in the dissertation.

Third, phenomena like Bose-Einstein condensation or parametric scattering which require polaritons only on the lower polariton branch(LPB). in order to observed those phenomena, we progress the power dependent angle-resolved photoluminescence to detect the polariton distribution with different input power. And under the suitable conditions, the Bose-Einstein condensation behavior may be observed, that is to say, the polariton laser is achievement.

4.2 Micro-Photoluminescence experiment results

In chapter 2, we can define the strong-coupling regime from Eq(2.39) as

$$\hbar\Omega > \left|\frac{\gamma - \gamma_c}{2}\right| \qquad\qquad Eq(4.2)$$

where $\hbar\Omega$ has the sense of the coupling strength between the cavity photon mode and the exciton, γ, γ_c is the broadening of the exciton and cavity, respectively. Under the condition the anticrossing takes place between the exciton and photon modes. In this regime, two distinct exciton-polariton branches manifest themselves as two optical resonances in the reflection or transmission spectra. The splitting between these two resonances is referred to as the vacuum-field Rabi splitting. It reaches 4–15 meV in current GaAs-based microcavities, up to 50 meV in GaN-based microcavities, and is found to be as large as 120 meV in ZnO-based microcavities. The physical meaning of γ_c is the same as cavity quality factor (Q-factor). Higher Q-factor indicates a lower rate of energy loss relative to the stored energy of the oscillator; the oscillations die out more slowly. In other word, higher Q-factor is longer lifetime and smaller energy broadening. In order to get γ_c the

as small as possible, we need higher reflectivity mirrors.

In current semiconductor samples of the dissertation, the reflectivity of the bottom 30-pair AlN/AlGaN DBR and the top 9-period dielectric SiO_2/HfO_2 DBR is 93% and 97%, respectively. As shown in Fig 4.1, We tune the cavity length to match the different resonance wavelength, include 381.5 nm, 384.4 nm, 391.5nm. By the micro-photoluminescence, we can obtain the three Q-factors, 256, 320, 279, respectively.

4.3 Angle-resolved reflective experiment results

To further probe the characteristics of strong exciton-photon coupling in the ZnO MC structure, RT angle-resolved reflectivity measurements were performed for the observation of in-plane polariton dispersion curves, which were carried out by using a two-arm goniometer and a xenon lamp employed as a white light source combined with a 100 μm core optical fiber. The reflected light was then collected by a 600 μm core UV optical fiber mounted on a rotating stage with an angular resolution of ~1°. The color map of the angular dispersion of measured reflectivity spectra from 8 to 38° is shown in Fig. 4.3(a). Furthermore, the color map of the calculated angle-resolved reflectivity spectra with taking the resonant exciton into account is shown in Fig. 4.3(b). In our simulation, the reflectivity spectra were carried out based on the transfer matrix method and the resonant exciton was modeled by a Lorentz oscillator dispersive dielectric function. In Fig. 4.3 (a), the measured dispersion of the LPB obviously deviates from the parabolic cavity mode and approaches to exciton mode with increasing angle. Furthermore, a good agreement is found between the experimental and theoretical LPBs, as shown in Figs. 4.3 (a) and 4.3 (b), when we consider the strong exciton-photon coupling in our calculation by assigning the parameter related to the oscillator strength of about 10^5 meV^2. This value is nearly two times larger than that of GaN-based materials due to the larger oscillator strength of ZnO

materials. As can be seen from Fig. 4.3 (b), we estimated that the anticrossing occurs near the angle of about 34° and the corresponding vacuum Rabi splitting value is about 72 meV. This large vacuum Rabi splitting is the largest value reported in ZnO-based MCs at RT, which may originate from the high cavity quality factor, good ZnO crystal quality, and larger ZnO thickness. On the other hand, although the angular dispersion of the LPB is well visible from experimental results, the signature of the UPB is nearly not observable, as shown in Fig. 4.3 (a).

This interesting issue regarding the anticrossing behavior in bulk ZnO MCs was reported by Faure *et al.* in 2008.[17] They theoretically expected that the anticrossing behavior can be properly defined in bulk GaAs and GaN MCs, whereas only the LPB is a well-defined and well-mixed exciton-photon state in bulk ZnO MCs. They proposed that the UPB in bulk ZnO MCs is pushed into the continuum states of excitons due to the large vacuum Rabi splitting of 120 meV (i.e., twice larger than the exciton binding energy) in their calculation. Nevertheless, the Rabi splitting estimated in our structure is about 72 meV, which is only slightly larger than the exciton binding energy. Therefore, the UPB will not overlap with the exciton continuum states. To understand the origin of the invisible UPB in the bulk ZnO MC, except for the exciton continuum states, we further take into account the effect of absorption induced by scattering states of excitons in our simulation. The 3D exciton physical model is used in our calculation to involve the absorption of bound states and scattering states. The absorption due to scattering states is added into the dielectric function and the amplitude is adjusted to match the experimental absorption spectra. Fig. 4.2 shows the experimental (open blue circle) and simulated (solid line) absorption spectra of a bulk ZnO at RT. When the vacuum Rabi splitting energy is nearly the same as the exciton binding energy, it will give rise to the energy overlap between the UPB and the scattering states, which may originate from the exciton excited states, the onset of continuum absorption, and the exciton-phonon complexes, especially at RT. Fig. 4.3 (c) presents the simulation of angle-resolved reflectivity spectra for the bulk ZnO MCs after taking the scattering absorption into account. It is clearly observed that the UPB is significantly broadened due to its crossing with the

scattering states of excitons. Such a situation is especially important for bulk ZnO MCs due to the relatively thick cavity layer and the large absorption coefficient ($\sim 2 \times 10^5$ cm^{-1}) for ZnO materials.[17] These effects induce the damping of the coherence for upper polariton states and lead to the dispersion of UPB to be invisible. Although the full anticrossing behavior cannot be experimentally demonstrated because of the strong scattering absorption, it should be noted that clear observation of the LPB is more important for the investigation of Bose-Einstein condensation and polariton lasing. Prospects regarding the experimental observation of the complete anticrossing behavior may be achieved based on a ZnO/ZnMgO quantum-well-MC due to the decrease in the thickness of ZnO absorption and the enhancement of exciton binding energies, pushing the continuum states of exciton to higher energy values due to the 2D excitonic nature from the quantum confinement effect.

4.3.1   Angle-resolved Photoluminescence experiment results

The cavity quality factor of the ZnO MC is dependent on the pump beam spot size, which is induced by the contribution of different cavities originating from the microscopic fluctuation in thickness, interface roughness, and crystal imperfection. The different emission wavelengths cause the inhomogeneous broadening of the cavity mode when using a larger laser spot size. This phenomenon is commonly observed in wide-bandgap materials due to the difficulty in growing high-quality DBRs and cavity layers. A cavity quality factor of ~165 was probed from the PL measurements. However, when the laser spot size was focused to be about 10 um, the cavity quality factor of 320 was found, which demonstrates the high local quality of our ZnO MC structures. The sample was first studied by angle-resolved PL at RT. Two different detunings between the uncoupled photon and exciton modes at

zero in-plane wave vector were considered to confirm the strong coupling phenomenon. Fig 4.4

presents the experimental angle-resolved PL spectra of the ZnO MCs with approximate detunings of:

(a) $\delta = -78$ meV, and (b) $\delta = -26$ meV at RT. The dashed line corresponds to the uncoupled exciton

energy. Instead of a pure cavity mode following a parabolic dispersion, the lower polariton branch

(LPB) can be observed in these two cases. The photonlike LPB will approach to excitonlike LPB with

increasing angle and finally converges to an energy that is close to uncoupled exciton. Furthermore, it

is expected that the upper polariton branch (UPB) is not observable as a result of the strong absorption

of ZnO in this spectral range.

4.3.2   Temperature dependent Angle-resolved Photoluminescence

To get better understanding of the polairton occupancy and the corresponding competition

between relaxation and emission processes, we further plot the color maps of the angular dispersions

of measured PL spectra at different temperatures and detuning values. Fig 4.5(a)~ 4.5 (c) show the

color maps of the angle-resolved PL spectra at the temperatures of (a) 100 K, (b) 200 K, and (c) 300 K

for the case of $\delta = -78$ meV at RT. The strong redistribution of the polariton population is found with

increasing temperature from 100 to 300 K. At low temperature (100 K), a maximum of the LP

intensity can be observed at the angle of about 39° at which the energy difference between the cavity

photon mode and the uncoupled exciton mode shows zero detuning. This condition can be considered

an experimental demonstration of the presence of a relaxation bottleneck, induced by the inefficient

scattering rate of bottleneck polaritons into the ground state. The similar situation can be found when the temperature is 200 K. Furthermore, the intensity of the LP emission spreads over a wide range of angle from 15° to 30° when the temperature is 300 K, as shown in Fig. 4.5 (c). This enhanced polariton relaxation from the bottleneck should be caused through polariton-acoustic phonon interaction. On the other hand, with increasing temperature the decreases in exciton energy and in cavity-photon energy are resulted from a reduction of the bandgap energy and the temperature dependence of the refractive index, respectively. Therefore, the temperature-dependent detuning δ will also influence the distribution of polariton emission due to the different exciton and photon fractions of the polariton states. To get access to the exciton and photon contents in the mixed polariton states, we apply the quasiparticle model to obtain the expansion coefficients of the eigenstates on the exciton and photon basis[81]. The curved dashed lines shown in Fig. 4.5 (a)~(c) represent the calculated LPBs and the curved dot line and horizontal dot line show the pure cavity and exciton modes, respectively. Because of the temperature-dependent detuning, the angles of exciton-photon resonance are about 39°, 36°, and 31° for the temperatures of 100, 200 and 300 K, respectively. Furthermore, the Rabi splitting values, which increase with decreasing temperature, corresponding to the three temperatures are 67, 79, and 87 meV. This temperature-dependent Rabi splitting is also observed in recent studies[80], and may be induced by a decrease of the exciton oscillator strength with increasing temperature. Fig 4.5 (d)~2(f) show the angle-dependent composition of the cavity photon and exciton modes for the three detunings induced by different temperatures. The photon fractions at zero degree are 93%, 91%, and 85.5% with

decreasing exciton-photon detuning. It is obvious that this high fraction of photon leads to the observable bottleneck effect even if the polariton relaxation is assisted by polariton-phonon interaction at 300 K.

To further confirm the polariton relaxation mechanisms, we plot the color maps of the angle-resolved PL spectra and calculate the relevant exciton-photon fractions for the case of smaller detuning ($\delta = -26$ meV at RT) at different temperatures in Fig. 4.6. The obvious bottleneck effect can be found at 150 K when the photon fraction is about 82%. Furthermore, an uniform emission intensity ranging over 30° exhibits the dynamic competition between the phonon-assisted polariton relaxation and the escape of cavity photons at 250 K, as shown in Fig. 4.6 (b). When the temperature rises to 300 K, the maximum emission intensity is centered at zero degree and a relaxation bottleneck is absent due to the increased polariton-phonon interaction and the lower photon fraction of 68% at zero degree [Fig. 4.6 (c) and Fig. 4.6 (f)].

Figure 4.7 presents the color maps of the measured angle-resolved PL spectra at 150, 200, and 250 K for the exciton-photon detuning of −8 meV at 250 K. The corresponding exciton and photon fractions as a function of angle are calculated and shown in Fig. 4.7 as well. By comparing Figs. 4.6 (c) and 4.7 (a), based on the similar photon fraction of ~69% the polaritons can obtain the efficient scattering from high k states into lower k states by increasing the temperature from 150 to 300 K. On the other hand, at the same temperature of 200 K the obvious polariton bottleneck can be relaxed into the bottom of the LPB when the photon fraction is reduced from 91% to 63% [see Figs. 4.5(b), 4.5(e),

4.7(b), and 4.7(e)], which means the longer polariton lifetime sufficient for the relaxation process under the condition of relatively fewer phonons at 200 K. Furthermore, the LP emission intensity is more centered within a smaller range of angle when the temperature increases from 200 to 250 K. Contrary to the case of large detuning ($\delta = -78$ meV at RT), the suppression of polariton relaxation bottleneck in the condition of small detuning ($\delta = -8$ meV at 250 K) mainly originates from the low photon fraction and therefore the bottleneck effect is absent at 200 K, which indicates the importance of exciton-photon detuning in the possible presence of polariton relaxation bottleneck.

4.3.3 Power-dependent Angle-resolved Photoluminescence

In order to check the role of polariton-polariton scattering in polariton relaxation mechanism, in Fig. 4.8, we show the color map of Lower Polariton-Photoluminescence intensity dependence with angle at 300 K for an initial detuning of −68 meV and for incident power ranging from 170μW to 1mW. We find a small superlinear increase of the emission at small angles with increasing excitation and a suppression of the relaxation bottleneck, likely driven by the polariton-polariton scattering processes.

Increasing the pumping power speeds up the relaxation kinetics due to the onset of the polariton-polariton scattering mechanism. One can see that the distribution of the polariton population shifts to lower energies while remaining broad in energy and wave vector at low average pump power 170 μW. The polariton-polariton scattering plays only a weak role and that the relaxation is dominated

by interactions with phonons or residual free carriers under the small pumping condition.At stronger pumping, the scattering of polaritons to the ground state becomes much more effective due to the bosonic final state stimulation effect. This leads to an avalanchelike process that results in an exponential increase of the ground-state population. The exciton-polariton distribution is now strongly peaked at the bottom of the LPB, approaching the equilibrium Bose-Einstein distribution function.

We conclude the polariton-polariton relaxation mechanism may play a role in our system, which may explain the discrepancy with theory and the slightly reduced bottleneck suppression in the theoretical simulations at higher temperatures when compared to the experimental data.

4.4   Nonlinear emission

4.4.1   Nonlinear emission from ZnO-based microcavity

The nonlinear optical properties of this ZnO-based microcavity under nonresonant pumping with the Nd:YVO$_4$ 355nm pulse laser have then been investigated in our experiments, as shown in Fig. 4.9..

At room temperature, we can observed the nonlinear emission under the two detuning case, $\Delta = -26meV$ and $\Delta = -78meV$, and the average threshold power is 165μW and 12.5μW, respectively. Clearly, the detuning is playing a role since the threshold intensity for nonlinear emission with the relatively negative detunings $\Delta = -78meV$ is less than for the case of the relatively positive ones $\Delta = -26meV$. By using the repetition rate of the Nd:YVO$_4$ pulse laser, 1KHz, and the incident spot area, $(30\mu m)^2 \pi/\cos 60°$, the threshold power of 160μW and 12.5μW correspond to energy

density of 2.78 mJ/cm^2 and 0.21 mJ/cm^2.

The experiment results in Ref. [82], shows that the similar quality factor of the GaN-based QWs VCSEL is 480, and the threshold power is 17.5nJ/pulse. This threshold energy of 17.5 nJ/pulse corresponds to an energy density of 5.1 mJ/cm^2. The observation of a low-threshold coherent emission from our ZnO-based microcavity at relatively negative detuning $\Delta = -78meV$, 1 order of magnitude smaller than in previously reported VCSELs of wide bandgap material with similar quality factor.

In order to observe the polariton distribution below and above threshold, the power-dependent ARPL can help us to figure out the characteristics of lower polariton distribution, as shown in Fig 4.10.

Two emission spectra measured at $k_{\parallel} = 0$ at average pump power, from 8μW to 12μW is displayed in Fig. 4.9. A transition toward a nonlinear emission regime is clearly observed at a relatively low threshold pump power P$_{thr}$=12μW. This nonlinear emission is accompanied by a sharp increase in the integrated emission intensity Fig. 4.13□and a strong line narrowing as the measured emission linewidth decreases from 16.1 meV just belowthreshold down to about 2 meV . The latter is a signature of the significant increase in the coherence time well above the polariton radiative lifetime. In addition, the emission line exhibits a slight blueshift ($E_{shift} \sim 2.7meV$ at threshold) ascribed to polariton-polariton interactions. Analysis of the power dependence PL as shown in Fig 4.11, the spontaneously emitted polaritons emerge in the mode which undergoes stimulated scattering factor $\beta \sim (700)^{-1}$ [76, 77, 78]. In conventional microcavity lasers, the cavity volume is made small

(photons confined in 3D) leading to a large Purcell factor. Planar semiconductor microcavities differ in that the cavity confines photons in only 1D, but the stimulated scattering from the bosonic nature of the polaritons leads to inversionless coherent emission (termed polariton lasing) unrelated to the transparency condition[79].

Note also that above threshold the nonlinear emission peak remains far from the position of the uncoupled cavity mode(C) ,as shown in Fig 4.10. Furthermore, conventional lasing through C can be ruled out as the nonlinear refractive index n of ZnO is negative near the band gap, which means that the position of C is not expected to redshift with increasing pump power. All these features prove that the present system remains in the strong coupling regime above threshold. Some more information on this nonlinear polariton emission can be derived from angular-resolved PL measurements by monitoring the evolution of the farfield emission pattern below and above threshold, as shown in fig 4.10. It is thus seen that the width of the in-plane momentum distribution undergoes a sudden collapse when crossing the nonlinear emission threshold with the main emission emerging essentially from the lowest energy state at $k_{\parallel} = 0$.

The integrated output intensity collected at normal incidence for these conditions is shown as a function of pump intensity in Fig. 4.10 with negative detuning $\Delta = -78 meV$. A clear nonlinear behavior is found for the emission at 388 nm, with an increase of over 10^3 at the critical threshold around P_{th}=12 μW. This corresponds to a density of $N_{3D} = 3.8 \times 10^{14} cm^{-3}$ which is an order of magnitude below both the Mott density $N_{3D} = 1.2 \times 10^{20} cm^{-3}$ in ZnO at 300 K, and the transparency

density for bulk ZnO which provides the lower limit for lasing. These features are similar to polariton lasing reported in II-VI and III-V microcavities at low temperature. Planar semiconductor microcavities differ in that the cavity confines photons in only 1D, but the stimulated scattering from the bosonic nature of the polaritons leads to inversionless coherent emission (termed polariton lasing) unrelated to the transparency condition. Instead, stimulated scattering takes off when the occupation in any polariton mode reaches unity, which defines the polariton laser threshold. As we discuss below, we speculate that photonic disorder localizes the polariton condensate laterally (similar to CdTe microcavities), with the different modes first attaining unity occupation on different laser shots statistically. This behavior contrasts with previous observations of coexistence of strong coupling and low threshold lasing.
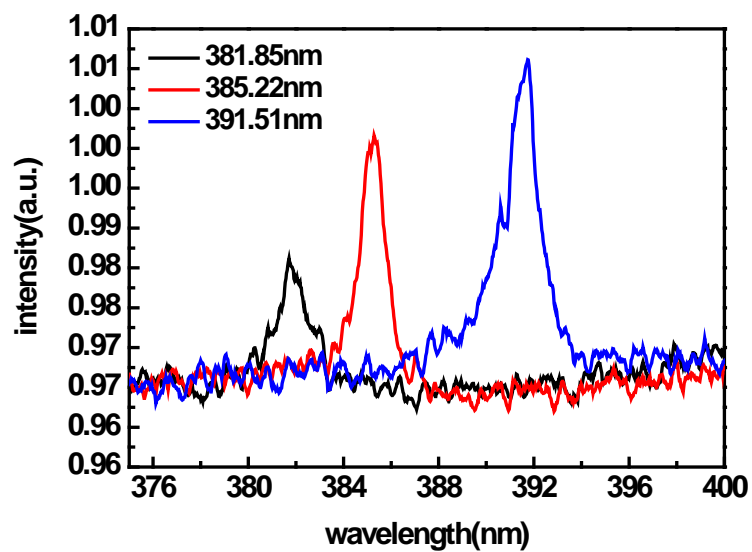
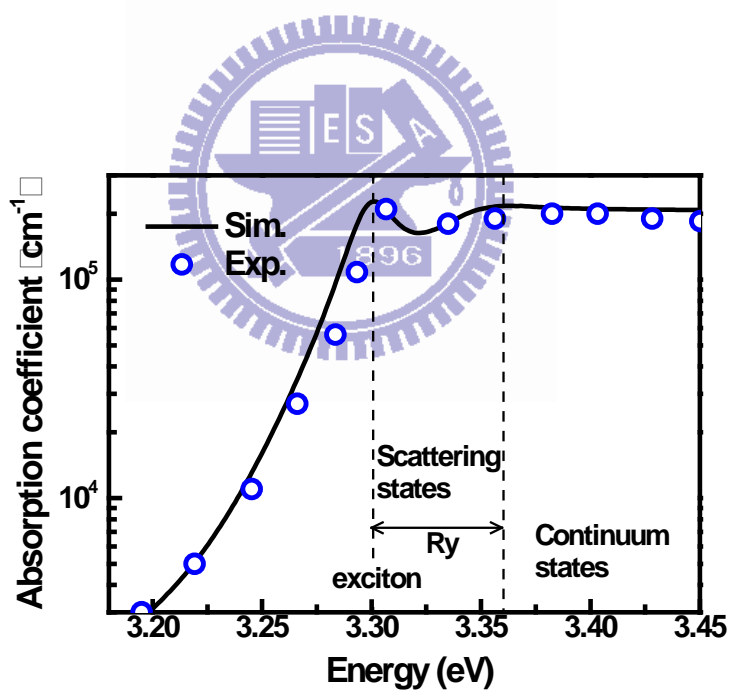Fig 4.1 the micro-PL measurement result on different detuning case

Fig 4.2Experimental (open blue circle) and simulated (solid line) absorption spectra of a bulk
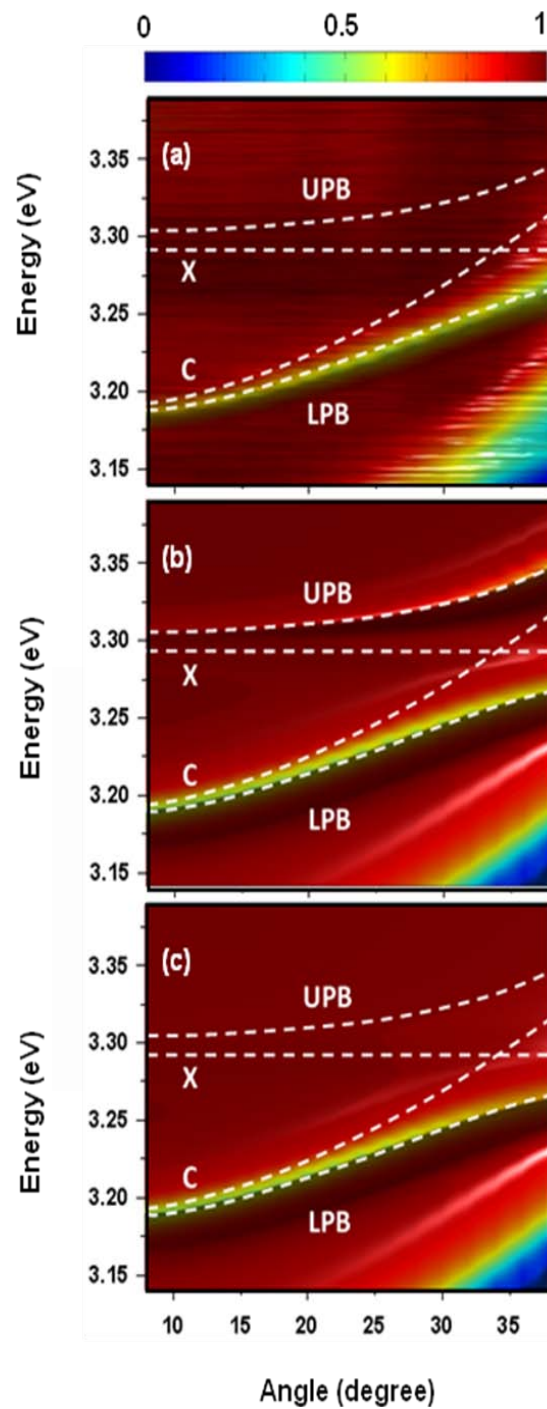
ZnO at RT.

Fig 4.3 (a) Color map of the angular dispersion of measured reflectivity spectra from 8 to 38° at RT. (b) Color maps of the calculated angle-resolved reflectivity spectra with taking the resonant exciton into account. (c) Simulation of angle-resolved reflectivity spectra for the bulk ZnO MCs after taking the absorption of scattering states into account.
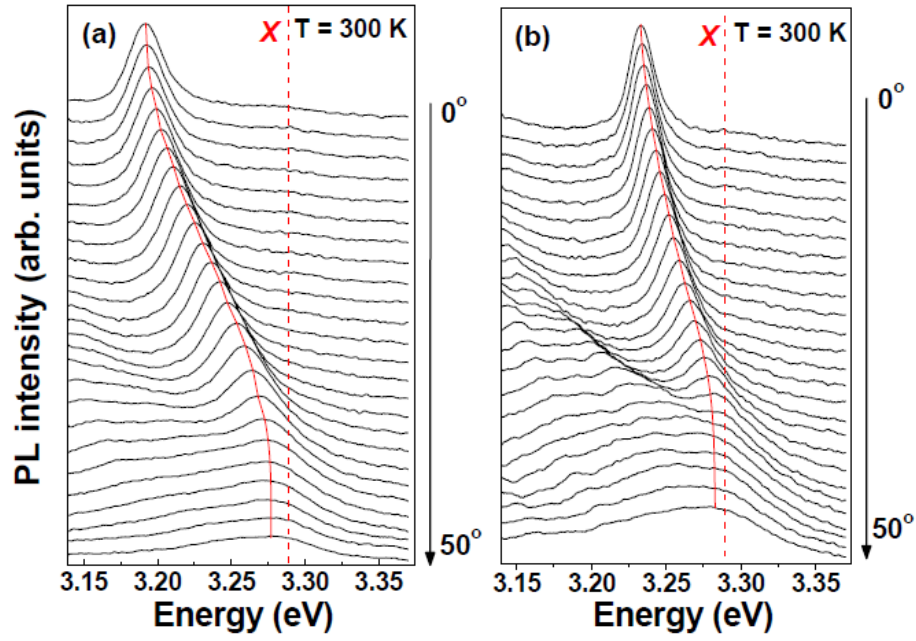
Fig 4.4 the experimental angle-resolved PL spectra of the ZnO MCs with approximate exciton-photon detunings of: (a) $\delta = -78$ meV, and (b) $\delta = -26$ meV at RT. The dashed line corresponds to the uncoupled exciton energy. The curve red line is a guide for the eyes, showing the dispersion of lower polariton branch.
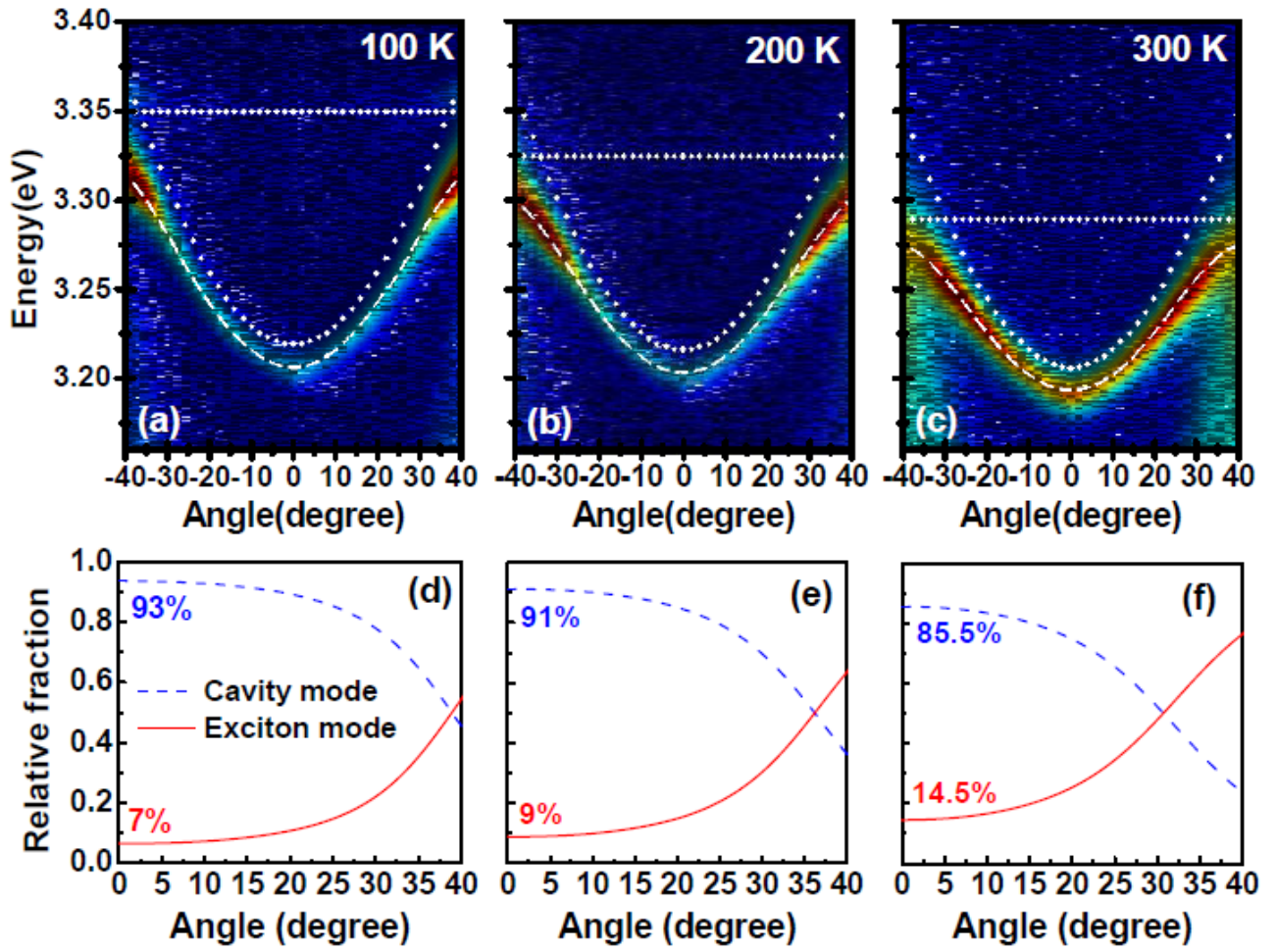
Fig 4.5 The color maps of the experimental angular dispersions of measured PL spectra at (a) 100 K, (b) 200 K, and (c) 300 K for the case of $\delta = -78$ meV at RT. The curved dashed lines represent the calculated LPBs and the curved dot line and horizontal dot line show the pure cavity and exciton modes, respectively. (d)~(f) show the calculated angle-dependent composition of the cavity photon and exciton modes for the three detunings induced by different temperatures.

Fig 4.6 The color maps of the experimental angular dispersions of measured PL spectra at (a) 150 K, (b) 250 K, and (c) 300 K for the case of $\delta = -26$ meV at RT. (d)~(f) show the calculated angle-dependent composition of the cavity photon and exciton modes for the three detunings induced by different temperatures.
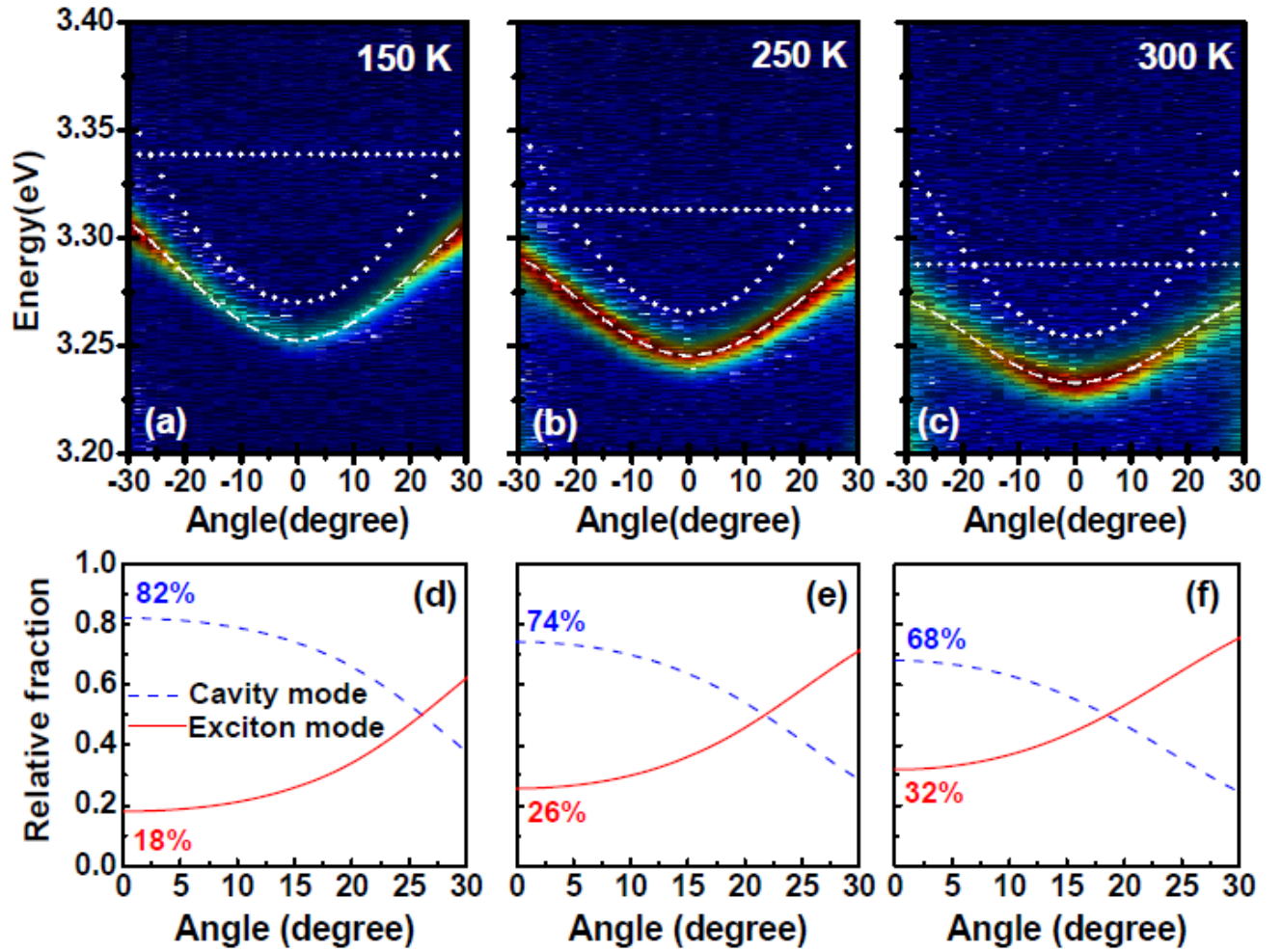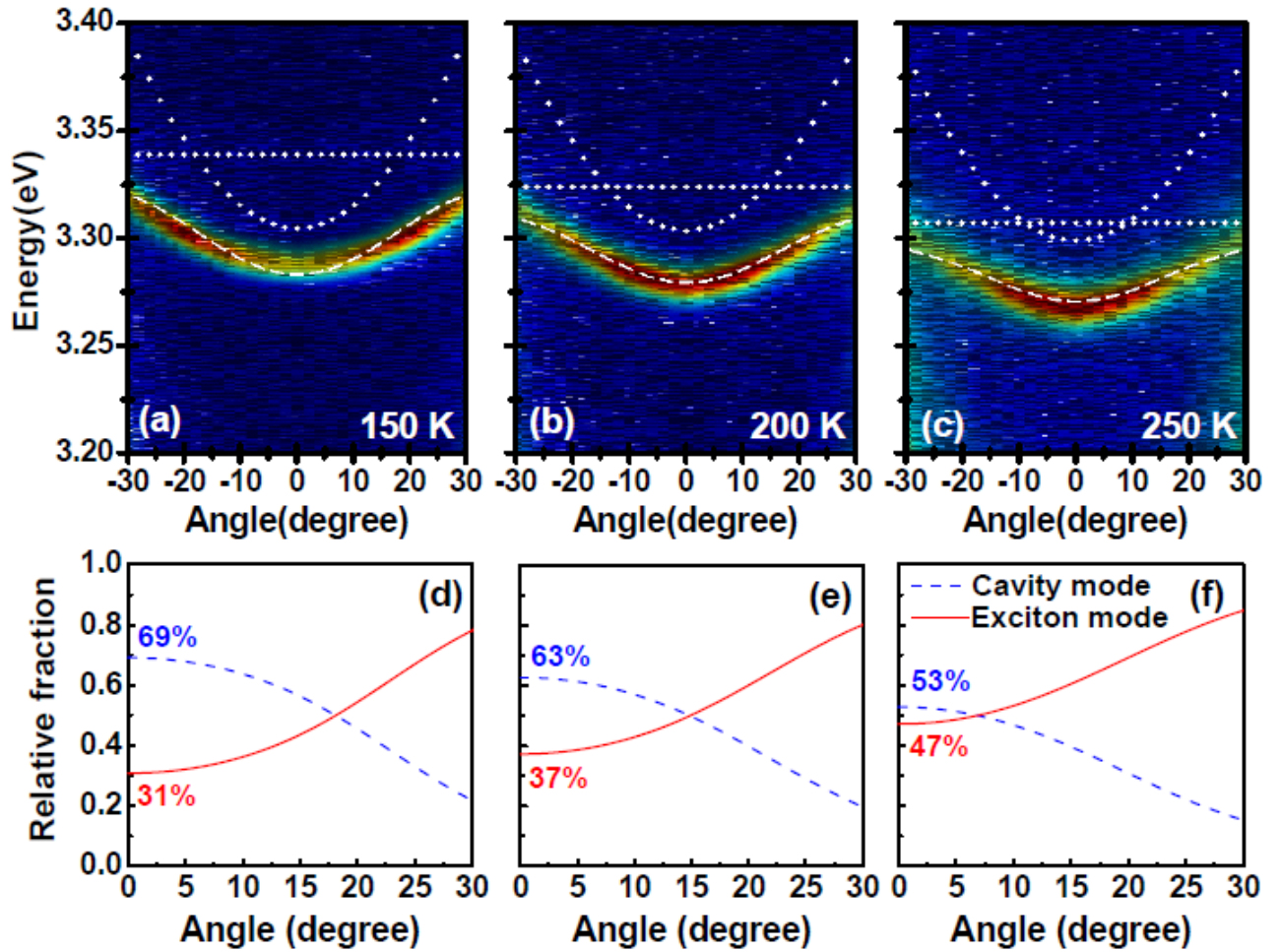
Fig 4.7 The color maps of the experimental angular dispersions of measured PL spectra at (a) 150 K, (b) 200 K, and (c) 250 K for the case of $\delta = -8$ meV at 250 K. (d)~(f) show the calculated angle-dependent composition of the cavity photon and exciton modes for the three detunings induced by different temperatures.
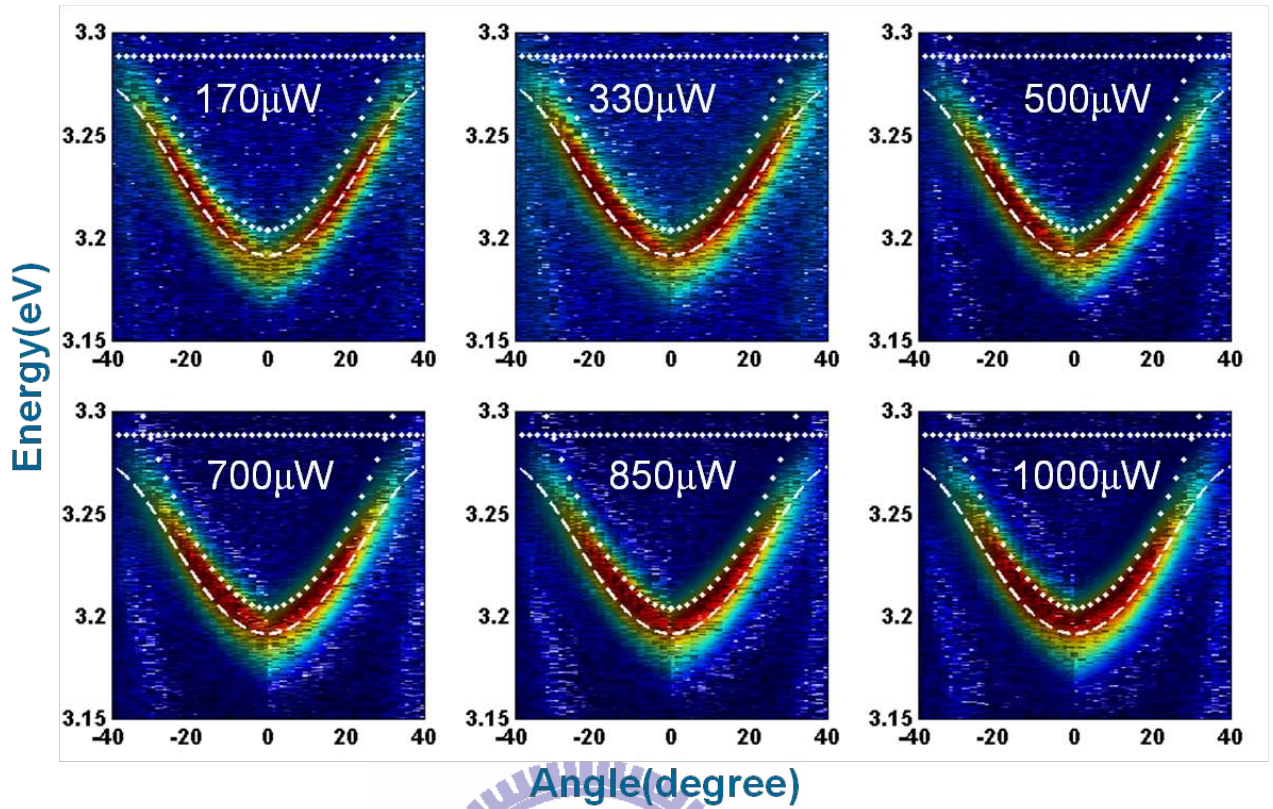
Fig 4.8 Experimental LP-PL intensities as a function of the external detection angle for different excitation power densities at room temperature. The detuning between the uncoupled photon and exciton modes at k=0 is −68 meV. The intensities are normalized to the excitation power density.
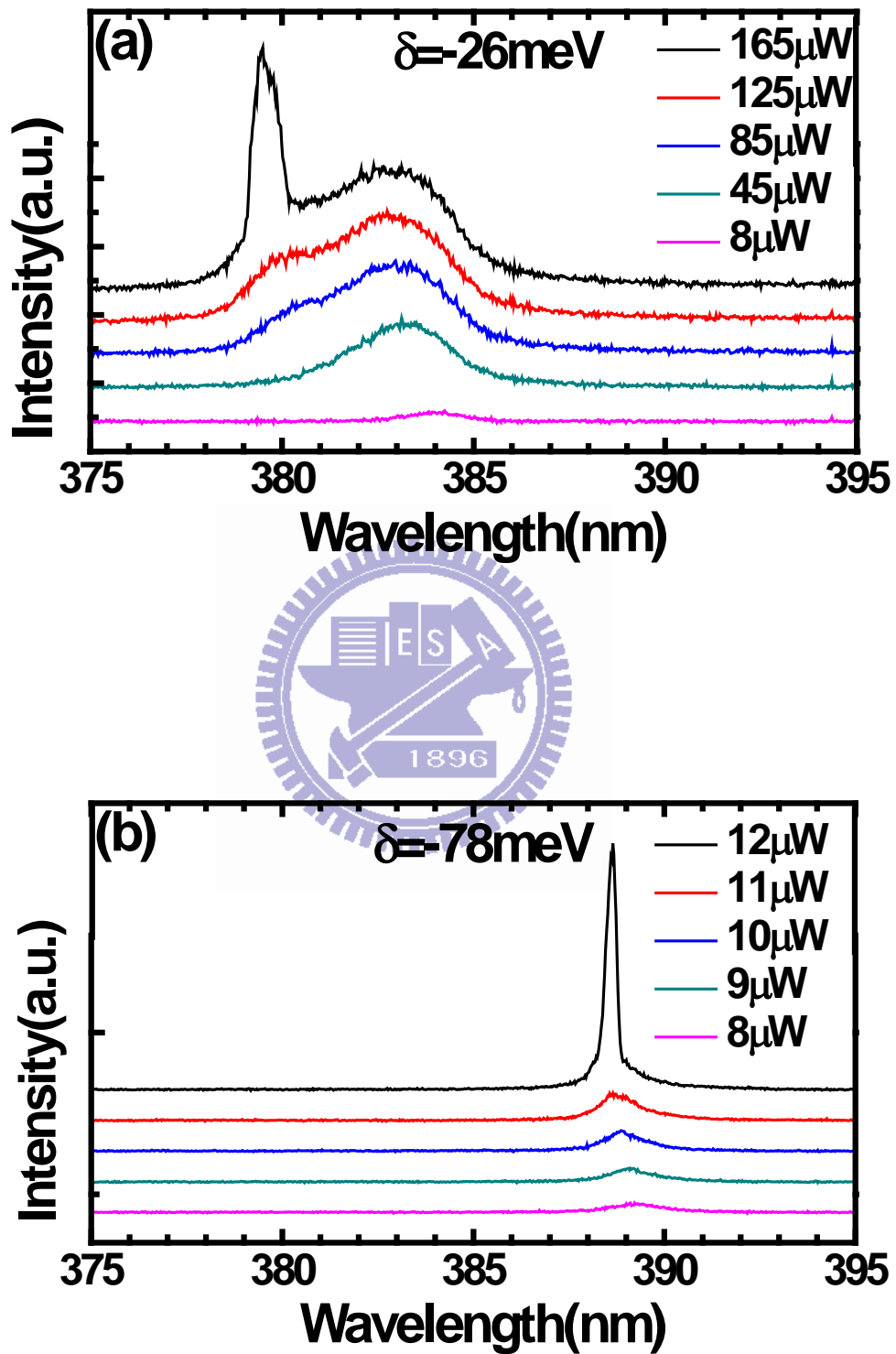
Fig 4.9 The PL spectra below threshold and above threshold with different detuning condition.
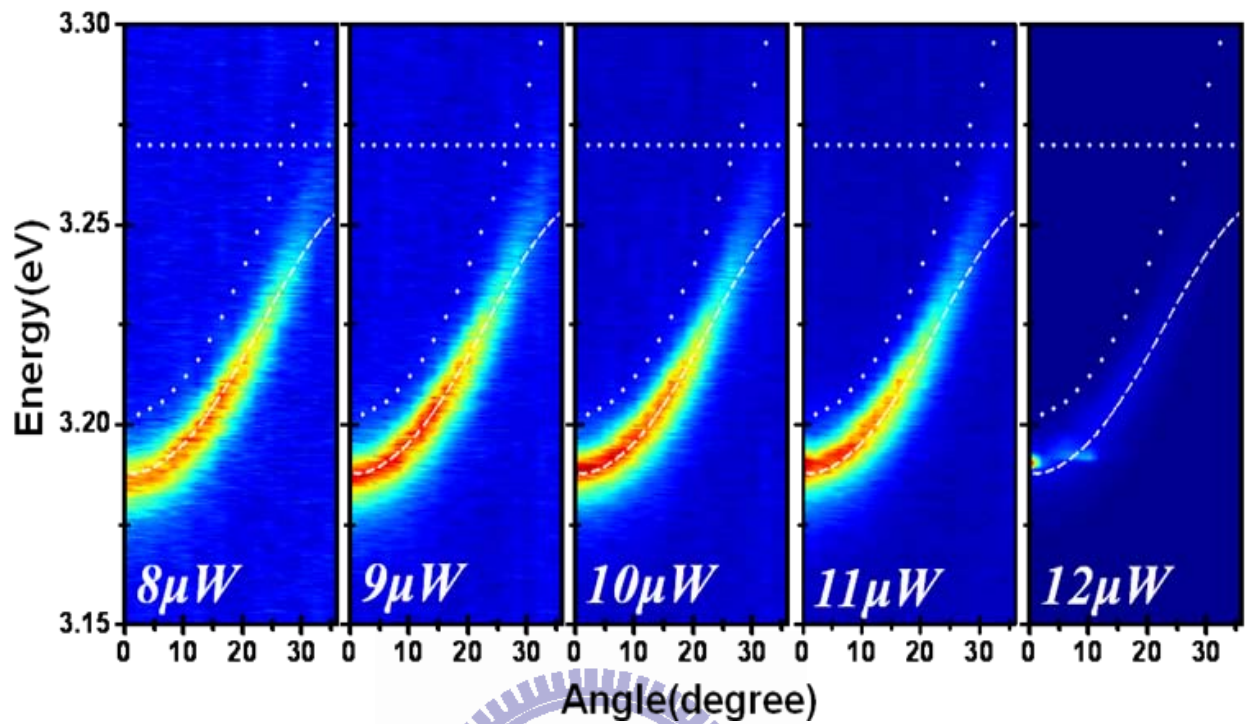
Fig 4.10 The color maps of the experimental angular dispersions of measured PL spectra below

threshold and above threshold at 300 K.
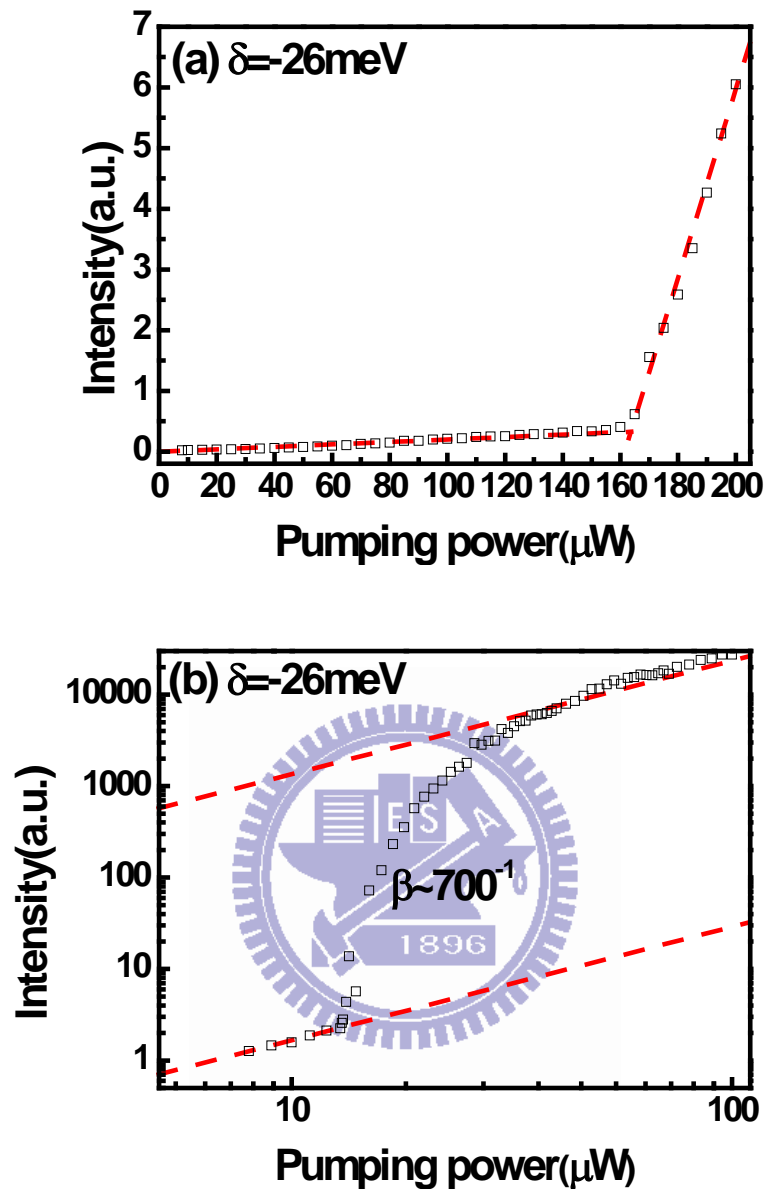
Fig 4.11. Integrated intensity vs pump power (solid points), with a guide line for the eyes(red dash line).

Fig 4.12 Experimental LP-PL intensities as a function of the external detection angle for different

excitation power at a room temperature.

Fig4.13 the normalized nonlinear emission spectra below threshold (8μW) and above threshold

(12μW)

Chapter5.   Conclusions

In conclusion, the strong exciton-photon coupling at RT has been observed from the ZnO-based hybrid microcavity structure. The dispersion curves based on angle-resolved reflectivity and PL measurements show obvious characteristics of s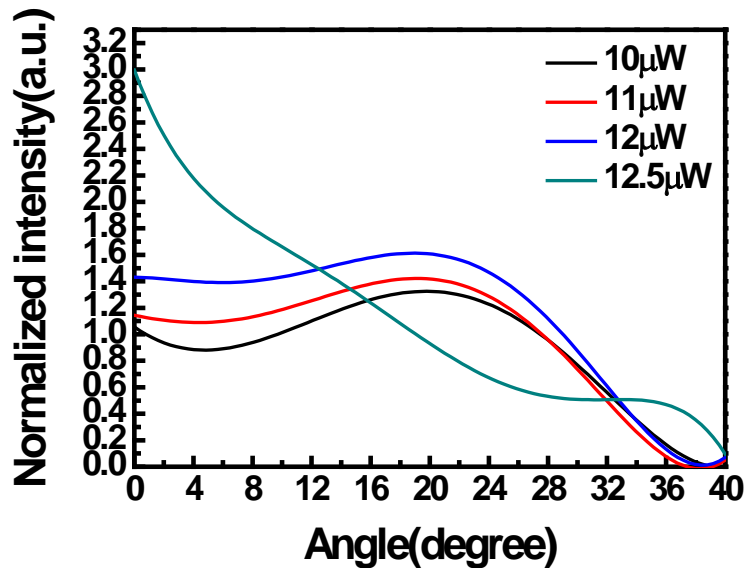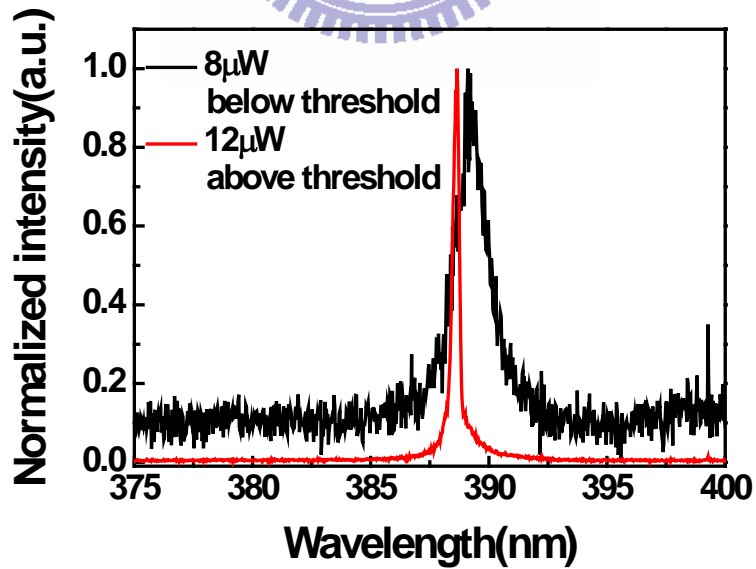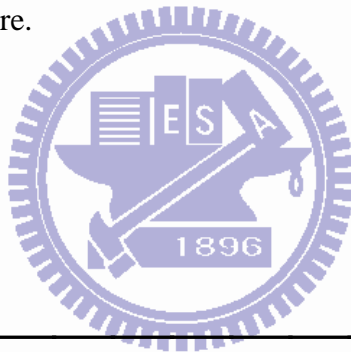trong exciton-photon coupling. Theoretically calculated exciton-polariton dispersion curves are in good agreement with the measured results. The large vacuum Rabi splitting value of about 72 meV is estimated from both different cavity-exciton detuning values. By performing angle-resolved PL measurements, we can observe the bottleneck effect for large negative detuning even at RT. This consequence may originate from the states with very high photon fractions in the low angle region.

The strong polariton relaxation bottleneck has been observed in bulk ZnO-based MCs at low temperature by performing angle-resolved PL measurements. The polariton relaxation from bottleneck to low k states can be enhanced with increasing temperature. Nevertheless, in the case of large exciton-photon detuning $\delta = -78$ meV at RT, the relaxation bottleneck cannot be completely suppressed even if the temperature is increased to 300 K due to the high photon fraction of polaritons at low k states. Furthermore, in the case of small exciton-photon detuning $\delta = -8$ meV at 250 K, the lower photon fraction results in longer polariton lifetime sufficient for the relaxation process into the low k states even though the temperature is only 200 K. These results reveal the possible design rule for the consideration of different temperatures and exciton-photon detunings in order to suppress the polariton relaxation bottleneck in ZnO-based MCs.

From the semi-classical Boltzmann equation, the scattering rates $W_{k \to k'}$ take into account exciton-phonon interaction (LO phonons by Fröhlich interaction, acoustic phonons by deformation potential and piezoelectric interaction) and exciton-exciton interaction in the Born approximation. The temperature dependent ARPL experiment under the similar detuning case condition can help us to confirm the effect of the polariton-phonon scattering. In addition to phonon interaction, we use the power-dependent ARPL to observe the polariton distribution with different exciton density. As theory, the bottleneck effect is suppressed when the pumping power increase due to the polariton-polariton interaction.

The nonlinear emission phenomenon has been observed at a very low threshold pumping power, only 0.21mJ/cm^2, 1 order of magnitude smaller than in previously reported nitride-based VCSELs. As result, we conjecture the nonlinear emission belong to Bose-Einstein condensation behavior. Moreover, the emission line blueshift due to polariton-polariton interactions, while thermal cavity expansion would have a similar effect and we measure no blueshift in a comparable empty microcavity. We have investigated the emission of hybrid bulk ZnO microcavities at room temperature and demonstrates the first room-temperature polariton lasing.

Reference

[1]. Anderson, M. H., Ensher, J. R., Matthews, M. R., Wieman, C. E. & Cornell, E. A. Science 269, 198 (1995).

[2]. Davis, K. B. et al. Phys. Rev. Lett. 75, 3969 (1995).

[3]. Bradley, C. C., Sackett, C. A., Tollett, J. J. & Hulet, R. G. Phys. Rev. Lett. 75, 1687 (1995).

[4]. Moskalenko, S. A. Fiz. Tverd. Tela 4, 276 (1962).

[5]. Blatt, J., Brandt, W. & Boer, K. Phys.Rev. 126, 1691 (1962).

[6]. Wolfe, J. P., Lin, J. L. & Snoke, D. W. Bose-Einstein condensation of a nearlyideal gas: Excitons in Cu2O in Bose-Einstein Condensation (eds. Griffn, A., Snoke, D. W. & Stringari, S.) 281 (Cambridge University Press, 1995).

[7]. Keldysh, L. & Kozlov, A. N. Sov. Phys. JETP 27, 521 (1968).

[8]. Weisbuch, C., Nishioka, M., Ishikawa, A. & Arakawa, Y. Phys. Rev. Lett. 69, 3314 (1992).

[9]. Dang, L. S., Heger, D., Andŕe, R., Boeuf, F. & Romestain, R. Phys. Rev. Lett. 81, 3920 (1998).

[10]. Senellart, P. & Bloch, J. Phys. Rev. Lett. 82, 1233 (1999).

[11]. Savvidis, P. G. et al. Phys. Rev. Lett. 84, 1547 (2000).

[12]. R. Huang, Y. Yamamoto, R. André, J. Bleuse, M. Muller, and H. Ulmer-Tuffigo. Phys. Rev. B. 65, 165314 (2002).

[13]. G´erard, J. M., Barrier, D., Marzin, J. Y., Kuszelewicz, R., Manin, L., Costard, E., Thierry-Mieg, V. and Rivera, T. Appl. Phys. Lett. 69: 449. (1996).

[14]. Bumki Min, Eric Ostby, Volker Sorger, Erick Ulin-Avila, Lan Yang, Xiang Zhang & Kerry

Vahala Nature **457, 455 2008**

[15].K. Hennessy, A. Badolato, M. Winger, D. Gerace, M. Atatüre, S. Gulde, S. Fält, E. L. Hu   and A. Imamog brevelu Nature 445, 896 (2007)

[16].I. I. Rabi, Phys. Rev. 51, 652 (1937).

[18].M. H. Anderson, J. R. Ensher, M. R. Matthews, C. E. Wieman, E. A. Cornell, Sci. 269 198 1995

[19].Weisbuch C, Nishioka M, Ishikawa A and Arakawa Y Phys. Rev. Lett. 69 3314(1992)

[20].Kavokin A, Baumberg J J, Malpuech G and Laussy F P, Microcavities (Semiconductor Science and Technology) (Oxford: Oxford University Press 2008)

[21].Dang L S, Heger D, André R, Boeuf F and Romestain R Phys. Rev. Lett. 81 3920(1998)

[22].Oulton R F, Takada N, Koe J, Stavrinou P N and Bradley D D C 2Semicond. Sci. Technol. 18 S419 (2003)

[23].Hobson P A, BarnesWL, Lidzey D G, Gehring G A, Whittaker D M, Skolnick M S andWalker S Appl. Phys. Lett. 81 3519 (2002)

[24].S. Christopoulos, G. Baldassarri Höger von Högersthal, A. J. D. Grundy, P. G. Lagoudakis, A. V. Kavokin, J. J. Baumberg, G. Christmann, R. Butté, E. Feltin, J.-F. Carlin, and N. Grandjean Phys. Rev. Lett. 98 126405(2007)

[25].Christmann G, Butté R, Feltin E, Mouti A, Stadelmann P A, Castiglia A, Carlin J-F and Grandjean N Phys. Rev. B 77 085310(2008)

[26].Antoine-Vincent N, Natali F, Byrne D, Vasson A, Disseix P, Leymarie J, Leroux M, Semond F
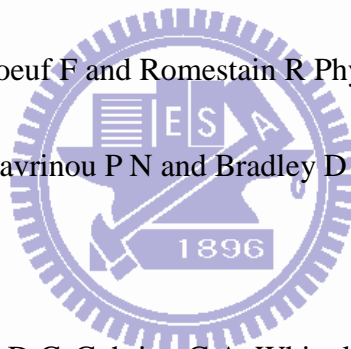
and Massies J Phys. Rev. B 68 153313(2003)

[27]. Schmidt-Grund R, Rheinländer B, Czekalla C, Benndorf G, Hochmuth H, LorenzMand

Grundmann M Appl. Phys. B 93 331 (2008)

[28]. Shimada R, Xie J, Avrutin V, Özgür Ü and Morkoˇc H Appl. Phys. Lett. 92 011127(2008)

[29]. F. Médard, J. Zuniga-Perez, P. Disseix, M. Mihailovic, J. Leymarie, A. Vasson, F. Semond, E.

Frayssinet, J. C. Moreno, M. Leroux, S. Faure, and T. Guillet Phys. Rev. B 79 125302 (2009)

[30]. Zamfirescu M, Kavokin A, Gil B, Malpuech G and Kaliteevski M Phys. Rev. B 65 161205(2002)

[31]. Kavokin A and Gil B Appl. Phys. Lett. 72 2880(1998)

[32]. Reitzenstein, S., C. Hofmann, A. Gorbunov, M. Strauss, S. H. Kwon, C. Schneider, A. Loffler, S.

Hofling, M. Kamp, and A. Forchel, Appl. Phys. Lett. 90, 251109(2007).

[33]. Deng, H., G. Solomon, R. Hey, K. H. Ploog, and Y. Yamamoto, Phys. Rev. Lett. 99,

126403(2007),.

[34]. Deng, H., G. Weihs, C. Santori, J. Bloch, and Y. Yamamoto, Science 298, 199(2002).

[35]. Deng, H., G. Weihs, D. Snoke, J. Bloch, and Y. Yamamoto, Proc. Natl. Acad. Sci. U.S.A. 100,

15318(2003).

[36]. Roumpos, G., S. Hoefling, A. Forchel, and Y. Yamamoto, APS March Meeting (unpublished),

Paper No. H1600010(2009).

[37]. Huang, R., Y. Yamamoto, R. André, J. Bleuse, M. Muller, and H. Ulmer-Tuffigo, Phys. Rev. B 65,

165314(2002)

[38]. Richard, M., J. Kasprzak, R. Romestain, R. Andre, and L. S. Dang, Phys. Rev. Lett. 94, 187401(2005).

[39]. J. Kasprzak, M. Richard, S. Kundermann, A. Baas, P. Jeambrun, J. M. J. Keeling, F. M. Marchetti, M. H. Szyman acuteska, R. André, J. L. Staehli, V. Savona, P. B. Littlewood, B. Deveaud and Le Si Dang, Nature 443, 409 (2006).

[40]. G. Malpuech, A. D. Carlo, A. Kavokin, J. J. Baumberg, M. Zamfirescu, and P. Lugli, Appl. Phys. Lett., 81, 412 (2002).

[41]. I. R. Sellers, F. Semond, M. Leroux, J. Massies, P. Disseix, A-L. Henneghien, J. Leymarie, and A. Vasson, Phys. Rev. B, 73, 033304(2006)

[42]. Vinattieri, M. Colocci, A. Tahraoui, and A. A. Khalifa, Phys. Rev. B, 74, 193308(2006).

[43]. R. Butté, G. Christmann, E. Feltin, J.-F. Carlin, M. Mosca, M. Ilegems, and N. Grandjean, Phys. Rev. B, 73, 033315(2006).

[44]. A. Alyamani, D. Sanvitto, A. A. Khalifa, M. S. Skolnick, T. Wang, F. Ranalli, P. J. Parbrook, A. Tahraoui and R. Airey, J. Appl. Phys.,101, 093110(2007).

[45]. E. Feltin, G. Christmann, R. Butté, J. –F Carlin, M. Mosca and N. Grandjean, Appl. Phys. Lett., 89, 071107(2006).

[46]. T. Tawara, H. Gotoh, T. Akasaka, N. Kobayashi, and T. Saitoh, Phys. Rev. Lett. 92, 256402(2004).

[47]. E. Feltin, G. Christmann, R. Butté, J. –F Carlin, M. Mosca and N. Grandjean, Appl. Phys. Lett.,

89, 071107(2006).

[48].S. Christopoulos, G. Baldassarri Höger von Högersthal, A. J. D. Grundy, P. G. Lagoudakis, A. V. Kavokin, J. J. Baumberg, G. Christmann, R. Butté, E. Feltin, J. –F. Carlin, and N. Grandjean, Phys. Rev. Lett., 98, 126405(2007).

[49].G. Christmann, R. Butté, E. Feltin, J. –F. Carlin, and N. Grandjean, Appl. Phys. Lett., 93, 051102(2008).

[50].G. Christmann, R. Butté, E. Feltin, A. Mouti, P. A. Stadelmann, A. Castiglia, J. –F. Carlin, and N. Grandjean, Phys. Rev. B, 77, 085310(2008).

[51].R. Butté, G. Christmann, E. Feltin, A. Castiglia, J. Levrat, G. Cosendey, A. Altoukhov, J. –F. Carlin, and N. Grandjean, in Proc. of SPIE, 7216-45, (2009).

[52].G. Christmann, R. Butté, E. Feltin, J. –F. Carlin, and N. Grandjean, Phys. Rev. B, 73, 153305(2006).

[53].E. Feltin, G. Christmann, J. Dorsaz, A. Castiglia, J. –F. Carlin, R. Butté, N. Grandjean, S. Christopoulos, G. Baldassarri Höger von Högersthal, A. J. D. Grundy, P. G. Lagoudakis, and J. J. Baumberg, "Blue lasing at room temperature in an optically pumped lattice-matched AlInN/GaN VCSEL structure", Electron., Lett., 4 (2007)

[54].J. J. Baumberg, A. V. Kavokin, S. Christopoulos, A. J. D. Grundy, R. Butté, G. Christmann, D. D. Solnyshkov, G. Malpuech, G. Baldassarri Höger von Högersthal, E. Feltin, J. –F. Carlin, and N. Grandjean, Phys. Rev. Lett., 101, 136409(2008).

[55]. M. Zamfirescu, A. Kavokin, B. Gil, G. Malpuech and M. Kaliteevski, Phys. Rev. B, 65, 161205(R) (2002).

[56]. S.F. Chichibu, A. Uedono, A. Tsukazaki, T. Onuma, M. Zamfirescu, A. Ohtomo, A. Kavokin, G. Cantwell, C. W. Litton, T. Sota and M. Kawasaki, Semicond. Sci. Technol., 20, S67(2005).

[57]. S. F. Chichibu, T. Ohmori, N. Shibat and T. Koyama, Appl. Phys. Lett., 88, 161914(2006).

[58]. R. Shimada, J. Xie, V. Avrutin, Ü. Özgür, and H. Morkoç, "Cavity polaritons in ZnO-based hybrid microcavities", Appl. Phys. Lett., 92, 011127(2008).

[59]. R. Schmidt-Grund, B. Rheinländer, C. Czekalla, G. Benndorf, H. Hochmuth, M. Lorenz, and M. Grundmann, App. Phys. B, 93, 331(2008).

[60]. M. Nakayama, S. Komura, T. Kawase, and D. G. Kim, J. Phys. Soc. Jpn., 77, 093705(2008).

[61]. R. Johne, D. D. Solnyshkov, and G. Malpuech, Appl. Phys. Lett., 93, 211105(2008)

[62]. A. Tsukazaki, A. Ohtomo, T. Onuma, M. Ohtani, T. Makino, M. Sumiya, K. Ohtani, S. F. Chichibu, S. Fuke, Y. Segawa, H. Ohno, H. Koinuma and M. Kawasaki, Nature Materials, 4, 42(2005).

[63]. Y. R. Ryu, J. A. Lubguban, T. S. Lee, H. W. White, T. S. Jeong, C. J. Youn and B. J. Kim, Appl. Phys. Lett., 90, 131115(2007)

[64]. Hanamura, E. & Haug, H., Physics Reports. Physics Letters Section C 33C, 209(1977).

[65]. Wannier, G. H. Phys. Rev. 52, 191 (1937).

[66]. Hopfield, J. J. Phys. Rev. 112, 1555 (1958).

[67]. Kavokin A, Thin Film and nanostructure (Oxford: Oxford University Press 2008)

[68]. S. Faure, T. Guillet, P. Lefebvre, T. Bretagnon, and B. Gil, Phys. Rev. B 78, 235323(2008).

[69]. Pau, S., J. Jacobson, G. Bjrk, and Y. Yamamoto, J. Opt. Soc. Am. B 13, 1078(1996).

[70]. Piermarocchi, C., F. Tassone, V. Savona, A. Quattropani, and P. Schwendimann, Phys. Rev. B 53, 15834(1996).

[71]. Tassone, F., and Y. Yamamoto, Phys. Rev. B 59, 10830(1996).

[72]. G. S. Huang, T. C. Lu, H. H. Yao, H. C. Kuo, S. C. Wang, C.-W. Lin, and L. Chang, Appl. Phys. Lett. 88, 061904(2006).

[73]. D. Solnyshkov and G. Malpuech, Superlattices Microstruct. 41, 279 (2007).

[74]. M. Richard, J. Kasprzak, R. Romestain, R. André, and L. S. Dang, Phys. Rev. Lett. 94, 187401 (2005).

[75]. Pavlos G. Lagoudakis, M. D. Martin, Jeremy J. Baumberg, Guillaume Malpuech, and Alexey Kavokin, J. Appl. Phys. 95, 2487 (2004).

[76]. Pavlos G. Lagoudakis, M. D. Martin, Jeremy J. Baumberg, Guillaume Malpuech, and Alexey Kavokin, J. Appl. Phys. 95, 2487 (2004).

[77]. Y. Yamamoto, S. Machida, and G. Bjo¨rk, Phys. Rev. A 44, 657 (1991);

[78]. G. Bjo¨rk, H. Heitmann, and Y. Yamamoto, Phys. Rev. A 47, 4451 (1993).

[79]. J. J. Baumberg et al., Phys. Rev. B 62, R16247 (2000).

[80]. G. Malpuech et al., Appl. Phys. Lett. 81, 412 (2002).

[81]. S. Faure, C. Brimont, T. Guillet, T. Bretagnon, B. Gil, F. Médard, D. Lagarde, P. Disseix, J.

Leymarie, J. Zúñiga-Pérez, M. Leroux, E. Frayssinet, J. C. Moreno, F. Semond, and S. Bouchoule,

Appl. Phys. Lett. 95, 121102 (2009).

[82]. V. Savona, L. C. Andreani, P. Schwendimann, and A. Quattropani, Solid State Commun. 93, 733

(1995).

[83]. Takehiko Tawara, Hideki Gotoh, Tetsuya Akasaka, Naoki Kobayashi, and Tadashi Saitoh Appl.

Phys. Lett. 83, 830 (2003).